Towards the Development of a Sub 500 Micron Thermally Actuated Scanning Fiber Endoscope for Detection of Lung Cancer: A Preliminary Investigation

by

Aydin A. Ahrabi

B.A.Sc., Simon Fraser University, 2013

Thesis Submitted in Partial Fulfillment of the
Requirements for the Degree of
Master of Applied Science

in the
School of Engineering Science
Faculty of Applied Sciences

SIMON FRASER UNIVERSITY

Summer 2018

Approval

Name:	**Aydin A. Ahrabi**
Degree:	**Master of Applied Science**
Title:	***Towards the Development of a Sub 500 Micron Thermally Actuated Scanning Fiber Endoscope for Detection of Lung Cancer***
Examining Committee:	**Chair: Michael Sjoerdsma** Senior Lecturer
	Carlo Menon Senior Supervisor Professor
	Pierre Lane Supervisor Associate Professor
	Behraad Bahreyni Internal Examiner Associate Professor School of Mechatronic Systems Engineering
Date Defended/Approved:	May 30th, 2018

Abstract

Medical professionals increasingly rely on endoscopes to carry out many minimally-invasive procedures on patients in order to safely examine, diagnose and treat a myriad of conditions. However, their distal tip size dictates which passages of the body they can be inserted into and consequently what organs they can access. For inaccessible areas and organs, patients are often subjected to intrusive, risky and uncomfortable procedures; diagnosis of lung cancer is one of these cases. Hence, this study sets out to design an endoscope head that has an outer diameter of less than 500 microns, small enough to be inserted into the lungs. To attain this goal, a novel approach based on resonance thermal excitation of a dual clad single mode optical fiber at a location close to its base is proposed. The previously obtained analytical models for describing the lateral vibratory motion of the fixed-free micro-cantilever are used to validate the corresponding physical prototypes. Parameters such as choice of materials, resonance frequency, bonding methods, shape and dimensions of the actuator bridge, structural rigidity, assembly are considered in the physical design of the device. Lateral free-end deflection of the center fiber is used as a benchmark for evaluating performance. The results show that this novel proposal can be used to satisfy the project requirements.

Keywords: Scanning Fiber Endoscope (SFE); Ultrathin; Thermal Actuation; Endoscopy; Resonance; Optical fiber;

I would like to dedicate this thesis to individuals dealing with cancer.

Acknowledgements

First and foremost, I would like to thank my senior supervisor, Dr. Carlo Menon, for his invaluable support and guidance throughout this project and for focusing on many projects that have a chance to make a difference in the world and improve the lives of many patients.

I would like to acknowledge BC Cancer Agency who sponsor this project. This project which aims to improve the life of millions of people that are diagnosed with lung cancer ever year would not exist without them. I would also like to thank Pierre Lane, Geoffrey Hohert, and Anthony Lee for their steadfast support of this project.

I am thankful to the past and present members of Dr. Menon's MENRVA research group at Simon Fraser University for their tireless support throughout the course of my research. I would like to especially thank Yasong Li, Mandeep Kaur, Gurpal Bisra, Chakaveh Ahmadizadeh, and Mojtaba Komeili for their contributions to this project.

Last and not least, I would like to thank my family for their unwavering support, patience and encouragement.

Table of Contents

List of Tables

List of Figures

List of Acronyms

BCCA	BC Cancer Agency
CAD	Computer-aided design
CCD	Charge-coupled device
CES	Cambridge Engineering Selector
CMOS	Complementary metal-oxide-semiconductors
CNC	Computer numerical control
DRIE	Deep reactive ion etching
EP17	EP17HTND-CCM one-part epoxy by Master Bond
FEA	Finite element analysis
MEMS	Micro electromechanical systems
MOSFET	Metal-oxide-semiconductor field-effect transistor
NA	Numerical aperture
PCB	Printed circuit board
PMMA	Poly-methyl methacrylate
RGB	Red, green, blue

Chapter 1. Introduction

1.1. Motivations

Modern science relies on endoscopes more than ever to safely examine, diagnose and treat a myriad of conditions in a minimally invasive manner. Non-invasive or minimally invasive here means there is no break in the skin and there is no contact with an internal body cavity beyond a natural or artificial body orifice. Therefore, what medical procedures can be performed by endoscopes on which parts of body or organs are dictated by their distal tip size which is the outer diameter of tail end of the flexible tube that gets inserted into the body. The distal tip size of most classes of endoscopes can range from a few millimetres to a couple of centimeters [1].

These dimensions mean that patients with coronary and stroke conditions or those dealing with lung and pancreatic cancer and various other ailments have to subject themselves to invasive and uncomfortable procedures that affect their quality of life for a prognosis. Furthermore, the recovering patients may have to deal with any complications that may arise during the often complicated procedures [2].

At the moment some of the smallest fiberoptic bronchoscopes in general use are approximately 1.6-2.2 mm distally which limits them to trachea and bronchial tube of the lung for the most part [3]. There is a need for lung biopsy for anything beyond that when a lung lesion is suspected of being cancerous. A lung biopsy involves removing a small piece of lung tissue which is examined for a diagnosis. This is usually done by inserting a long needle through the chest wall into the lung or making an incision between the ribs to remove a sample of lung tissue [4]. The following picture shows a needle lung biopsy in case of suspected lung cancer taking using computed tomography [5]:

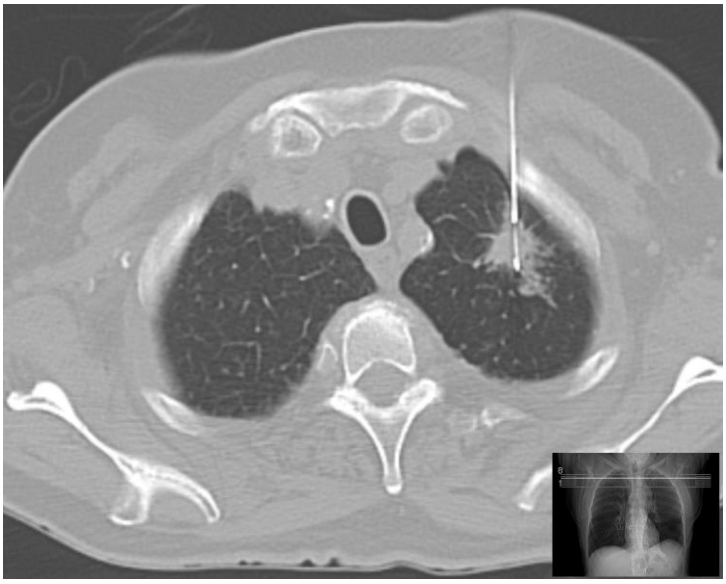

Figure 1. Needle lung biopsy for diagnosis of lung cancer
Hellerhoff, "Lung biopsy guided by computer tomography: Lung cancer," https://upload.wikimedia.org/wikipedia/commons/5/50/Biopsie_Lunge_Computertomographie_BC.png. Licenced under Creative Commons 3.0

Even outside of what is normally required for patients to recover from a procedure like this, this process carries several risks. The patient may develop a collapsed lung (pneumothorax), difficulty breathing, an infection, or a bleeding; in some rare cases serious enough to cause death [4]. More than 28,000 Canadians will be diagnosed with lung cancer every year (78 Canadians every day) which makes it crucial to find new less-intrusive ways of diagnosis that can improve their quality of life [6].

New advancements have been made in recent years in the form Scanning Fiber Endoscopes (SFE) to miniaturize the distal tip size further and this has resulted in relatively high-fidelity endoscopes that are only about 1.2+ mm [7]. However, this is not nearly small enough to make most areas of the lung accessible to medical professionals and help lung cancer patients.

Herein, a single fiber endoscopy approach is proposed that will try to address the two main factors preventing SFE's from shrinking further in size; their actuation method, and their collection fibers. This work introduces a novel actuation method in the form of thermal actuation to achieve the desired lateral vibratory motion as well as a single mode dual core optical fiber for both illumination and collection to be able to create an endoscope system small enough to be packaged inside of a sub 500-micron distal housing; small enough to access most airways and areas of the lung.

1.2. Objectives

This study pursues three goals:

1. To study the feasibility of resonance vibration of an optical fiber micro-cantilever using electro-thermal actuation
2. To design, develop and configure a prototype of a novel thermal actuator for a Scanning Fiber Endoscope that meets the strict ultra thin size requirements
3. To validate the proposed designs through experimentation and assess their performance

1.3. Summary of Contributions

The concept of a novel bimetal thermal actuator combined with one single mode dual core fiber is previous work by Komeili et al. [8] [9] [10] [11] [12]. These suggestions proposed by Mojtaba Komeili[1] are the basis of this project. These contributions are outlined in section 2.4. Section 3, titled theoretical foundations, is also his work for the most part and is included for reference.

The task of realizing the device based on the theoretical models constitutes my work, Aydin A. Ahrabi. This includes feasibility study of the idea covered in chapter 4. Designing and optimizing the physical device so that it meets the strict size requirements, and experimental assessment and verification of the performance of the design to prove it satisfices the project goals; presented in chapters 5 and 6.

Some of the prototypes were fabricated by Yasong Li[1]. The polymer collars used to secure the assembly inside of the housing tubes were primarily designed by her as well. This is presented in sections 5.7 and Appendix A.

All of the optical fibers used in this project were supplied by BCCA. Most of them were made by Geoffrey Hohert. Some were fabricated by Mandeep Kaur[1].

Gurpal Bisra[1] and Chakaveh Ahmadizadeh[1] temporarily worked on this project. Their contributions did not end up in the current version of the device. Therefore, none of

[1] MENRVA research group member, Dr. Menon's lab at Simon Fraser University

their work is presented here. Mandeep Kaur currently works on creating and expanding the analytical models and simulations for this project. However, her contributions are not discussed in this document either.

1.4. Thesis Layout

The remainder of this thesis is organized as follows:

Chapter 2, literature review, gives an overview of what constitutes a flexible endoscope, most commonly found configurations and what is preventing them from shrinking down further in size. Then, scanning fiber endoscopes (SFE) are examined and the common set-ups and their limitations in terms of size are discussed. A summary of thermal actuators is presented afterwards, outlining what makes the proposal in this project novel and unique. Finally, the analytical work previously done at MENRVA research group on this project is presented.

Chapter 3 further develops the mathematical models to more closely match the device going to be made in the subsequent chapters. This chapter presents a summary of calculations and theoretical work the design is based on.

Chapter 4 studies the feasibility of the novel approach by comparing the analytical results to preliminary physical prototypes made in the lab. This chapter covers objective 1.

Chapter 5 explains the design and fabrication process of the proposed sub 500-micron endoscope tip enclosure and presents several configurations for the system. This chapter covers objective 2.

Chapter 6 covers objective 3 and aims to assess the performance and validate the design through experimentation. It also evaluates and discusses their limitations.

Chapter 7 gives a summary of the thesis, draws conclusions by highlighting the main findings and provides recommendations for future work.

Chapter 2. Literature Review

In this chapter, a literature review on endoscopes, and, in particular, scanning fiber endoscopes is presented. There are many components to an endoscope. In accordance to the scope of this project, most of the discussion is focused on the insertion tip and components and methods used to shine and receive light at the distal tip. First, a quick overview of video endoscopes is given. Then, scanning fiber endoscopes (SFE) are discussed. Finally, the preliminary work done at MENRVA labs to address the aforementioned devices' shortcomings regarding ultra thin airways and passages found in lungs and how they may be remedied is outlined.

2.1. Flexible Endoscopy

Medical devices that are used to image the internal organs can be grouped into two categories. The first category consists of structure-based imaging, such as x-ray computed tomography (CT), magnetic resonance imaging (MRI), and ultrasound which image at low spatiotemporal resolution (millimeters, seconds). The second category is made of surface-based imaging using optical endoscope technologies which image at high spatiotemporal resolution (micrometers, milliseconds) [2]. An endoscope is a medical device that is inserted directly into the body to examine the interior of a hollow organ or cavity [13]. There are many types and configurations of endoscopes available depending on which site in the body or type of procedure is being performed. An endoscopy procedure may be prescribed to investigate symptoms, diagnose, and treat various conditions and ailments. It can be used to determine what's causing signs and symptoms such as nausea, vomiting, abdominal pain, gastrointestinal bleeding, etc. It can also be used to perform a biopsy and collect tissue samples to test for diseases such as anemia, inflammation, diarrhea or cancers. Furthermore, specially equipped endoscopes can be utilized to treat problems such as internal bleedings by cauterizing them or clip a polyp or remove a foreign object. An endoscopy is a very safe procedure but complications such as bleedings, infections and tears may occur in rare situations [1].

Endoscopes come in various configurations, each with different features and each optimized for the portion of the body they're designed to examine but the basic

shape and layout of the instrument are relatively unchanged since they were first introduced. In addition, almost all include a long flexible insertion tube, a light delivery system to illuminate the organ or object being inspected, a lens system to direct the light being shined at the target back to the receiver and additional channels to house medical instruments and manipulators or tubes for air and water. The light source is normally situated outside of the insertion tube and the light is typically directed using an optical fiber system. The light sensors or receivers are typically made of charge-coupled device (CCD) sensors or complementary metal-oxide-semiconductors (CMOS). A modern endoscope is shown in the figure below [2]:

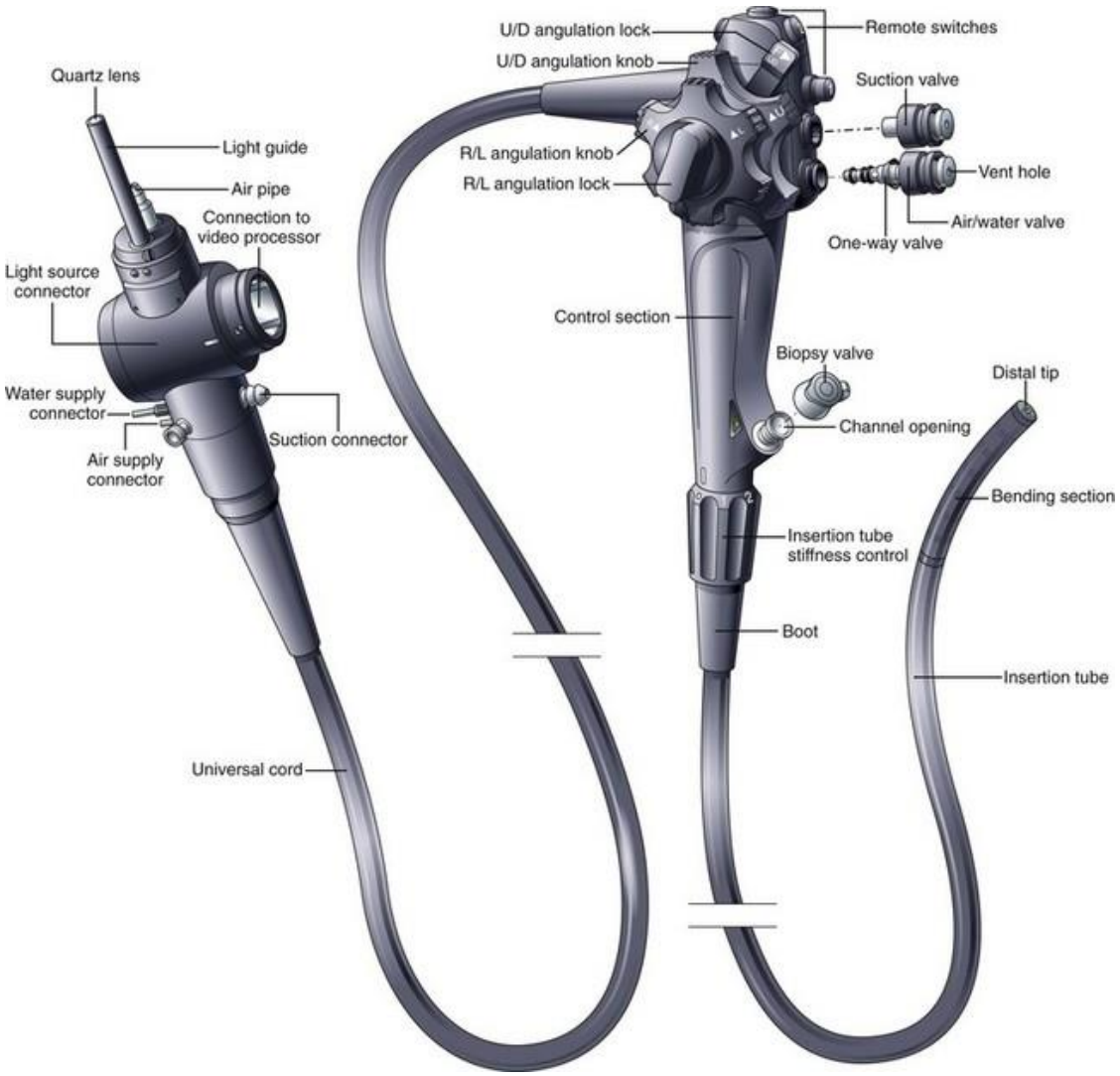

Figure 2. The basic components and controls of a flexible video endoscope
Reproduced with permission of Elsevier.

A solid-state CCD image sensor is an array of individual photo cells, also commonly referred to as photodiodes or “pixels”. An electric charge proportional to the brightness of the light is generated when light hits a pixel. The charge from each pixel is then sent through a very limited number of output nodes to be converted to voltage, buffered, and sent off-chip as an analog signal. After decoding the analog signal, the resultant bits are processed to form a video frame. This process can be repeated to reach the desired framerate. Basic CCDs can only respond to light intensity and do not detect color. Therefore, each pixel is given one of there primary color filters (red, blue, green) by metal oxide etching. One pixel will measure the intensity of light through a red filter while adjacent pixels do the same through blue and green filters. A full color image is produced when the values of colors and brightness levels from the 3 adjacent pixels are combined and processed. A CMOS sensor works in a similar fashion. However, in a CMOS sensor, each pixel has its own charge-to-voltage conversion, and the sensor often includes amplifiers, noise-correction, and digitization circuits on the chip itself, so it outputs digital bits. Both CCD and CMOS sensors offer excellent performance and produce high quality and high-resolution videos. However, these other functions increase the design complexity and reduce the area that is available for light capture. The smaller the solid-state sensor, the smaller the pixels have to be which results in lower sensitivity to light and higher noise levels. In addition, the pixels must be electrically isolated from each other [14]. So, there is a limit to how small the sensors can get which consequently dictates how small the overall distal tip of the endoscope can get. The figure below illustrates the components typically found at the distal tip of an end-viewing endoscope, such as a bronchoscope:

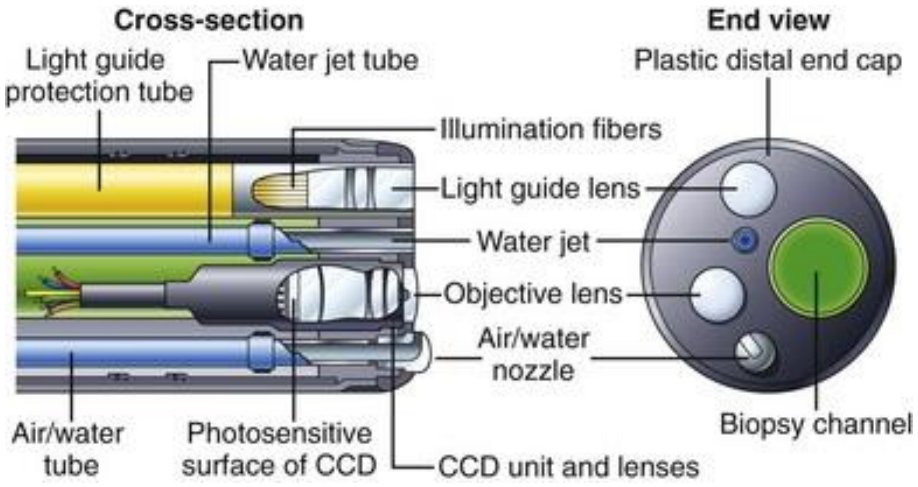

Figure 3. Components found in the distal tip of an end-viewing endoscope
Reproduced with permission of Elsevier.

The illuminating light travels through the instrument via optical fibers is evenly dispersed across the endoscopes field of view by a system of light guide lenses. The objective lens and sensor are tightly sealed to protect the imaging system from damage if fluids were to enter the device by accident. Typical sensors used in these endoscopes range from about 0.9-3mm and depending on the application and what's included in the endoscope the entire package can be 2-12mm in diameter [2].

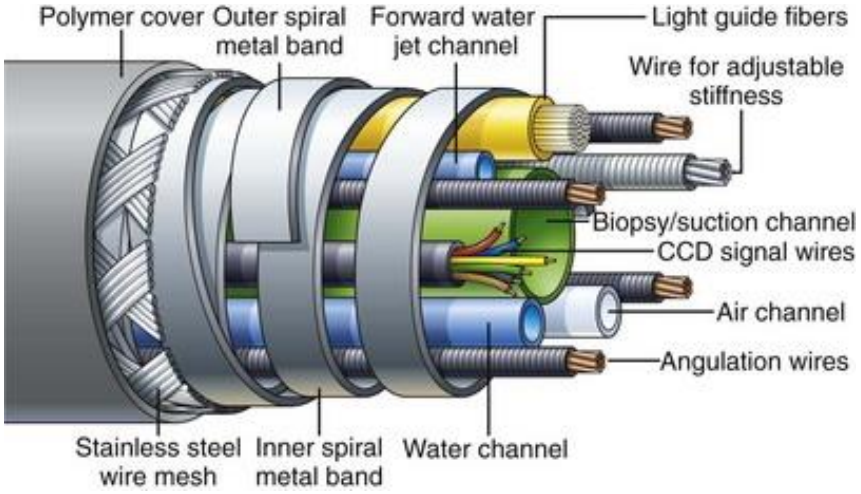

Figure 4. Internal components of an end-viewing endoscope
Reproduced with permission of Elsevier.

Due to the tight arrangement of the delicate components in the confines of the endoscope sheath, endoscopes of this kind are highly prone to significant damage arising from allowing the endoscope tip to drop on the floor or bounce off some hard

surface. Mouthpieces should be used when the endoscope is inserted into the body through the mouth because one firm bite on the insertion tube can cause major damage [2].

These endoscopes are not disposable or one-time use. Therefore, after every procedure they need to be thoroughly washed and cleaned. Even though, the endoscopes are disinfected to a high level, in day to day practice, they cannot be truly sterilized. So, there is always a risk of infection, albeit small, due to potential retained pockets of fluid [2].

As discussed, for endoscopic imaging, both illumination and detection elements must be routed through an often twisty anatomical geometry to the region being examined. Therefore, the size and rigidity of the endoscope dictate access to the internal organs. Similarly, these dimensions would limit a bronchoscope to only examining the trachea and bronchi for the most part and underscore the need for a smaller distal tip to both improve accessibility and reduce tissue trauma and discomfort.

2.2. Scanning Fiber Endoscopes (SFE)

Minimally invasive medical procedures rely on flexible and thin endoscopes that produce high quality images. However, current devices use fiberoptic bundles or silicon image sensors positioned at the distal tip where each pixel in the image corresponds to an element on the detection sensor. This represents a fundamental trade-off where resolution or image quality is sacrificed when the scope diameter gets small (typically smaller than 3 mm) [15]. Scanning fiber endoscopy (SFE) was developed to address this problem by providing full color and high-resolution images in a flexible form factor and in diameters smaller than what is possible with the conventional technology to make previously inaccessible parts of the body open to minimally-invasive medical procedures. The SFE uses a single model optical fiber vibrating at its first natural frequency to scan a focused laser spot over the organ tissue being examined and one or more optical fibers acting as the detector to record the time-multiplexed backscatter signal [15] [16].

In Seibel et al. [15] [16] [7] SFEs from 1.6mm to 1.2mm in diameter are outlined. The main component of the SFE is a single laterally vibrated resonant single-mode optical fiber scanning RGB laser light onto the image plane. A custom tubular

piezoelectric actuator in a coaxial design is used to vibrate the optical fiber in a cylindrical fashion. This fiber is a standard 125 µm or 80 µm diameter fused silica single mode optical fiber [7]. This lateral vibratory motion of the optical fiber can be modeled as a cylindrical, base-excited cantilever with fixed-free boundary conditions shown in equation (1) [17]:

$$F = \frac{\pi\sqrt{E}}{16\sqrt{\varrho}}\frac{R}{L^2}(1.194^2, 2.988^2, \dots) \quad (1)$$

In equation (1), natural frequency is denoted by 'f', fiber density is shown as ϱ, modulus of elasticity is E, radius is R, and L is the length of the solid fiber cantilever. The fiber is assumed to be perfectly cylindrical. For fiber lengths of around 1mm, resonance frequencies of 5 to 12 kHz are expected for the 125 µm to 80 µm fibers. The figure below illustrates the layout, and placement of different components of a SFE in a spiral scan pattern [18]:

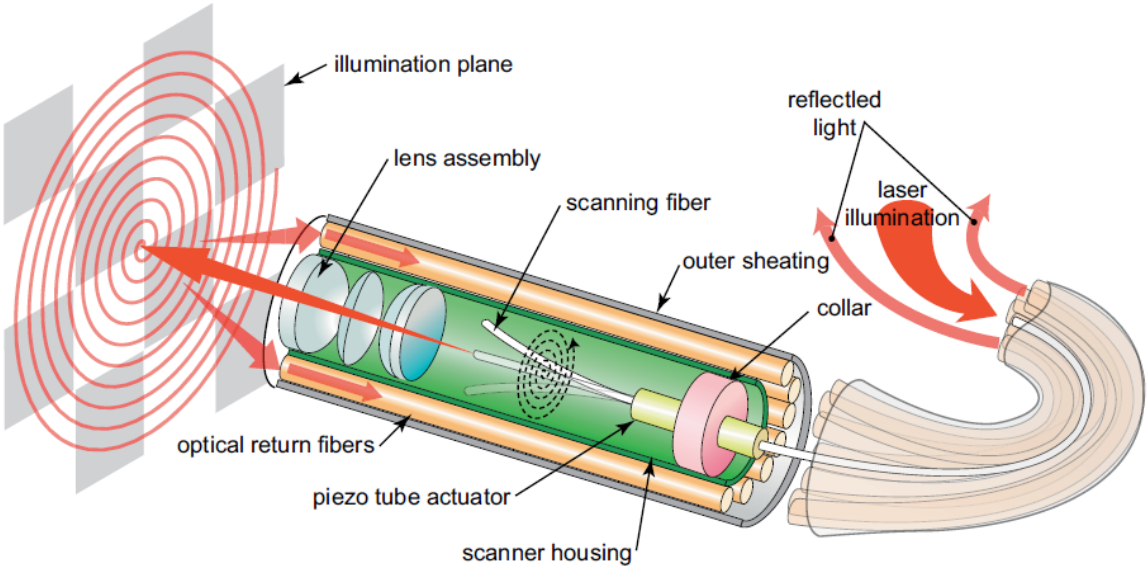

Figure 5. Layout of a SFE with a fiber moving in the spiral scan pattern
Reproduced with permission of John Wiley and Sons.

In short, the laser illumination is carried through the single mode fiber at the center to the distal tip. The single mode fiber then shines the coherent light in a spiral pattern at a large area. The light is finally collected and carried to be processed by the multimode optical fibers that surround the housing tube on the outside [18].

The spiral scan pattern is unconventional as in a sense that unlike most other resonant device that operate at a set frequency and amplitude, the SFE with a spiral scan pattern is rapidly excited and damped. First, an outwardly growing spiral pattern is created during the excitation phase. The image is captured at this stage. Then an active breaking input will quickly reduce the spiral movement by 95% and finally the power is cut and the vibrations are allowed to decay naturally before the start of the next cycle. This three-stage scanning cycle is shown in the picture below [18]:

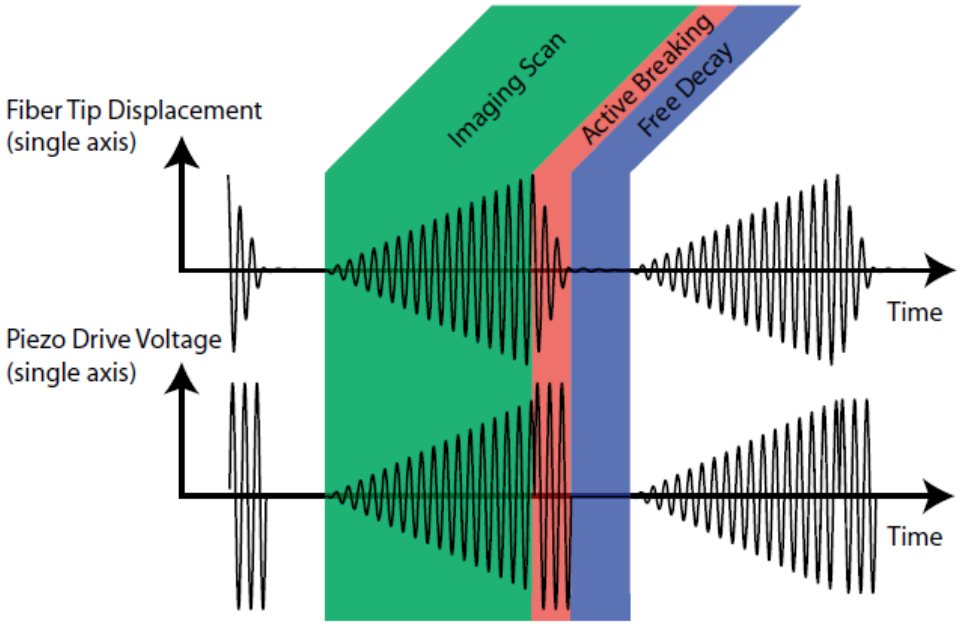

Figure 6. The three phase excitation modes for the spiral scan pattern
Reproduced with permission of John Wiley and Sons.

The parameters of the spiral scan can be tuned to capture more lines at the cost of lower framerates and vice versa. For example, it can be set to capture 500 lines at 30 Hz, or 1000 lines at 15 Hz [18].

The spiral scan pattern is not the only scanning pattern being used in SFEs. Raster and propeller scan patterns are also used, each having their own pros and cons. A piezotube with quartered electrodes can create two-dimensional resonant scan patterns with a single actuator because it provides before horizontal and vertical actuation. The resonant scans are typically sinusoidal because resonant amplification occurs only in a small range around each natural frequency. Lissajous patterns result from z-y scans of two sinusoidal signals. A stable closed pattern is created if the two signals' frequency ratio can be expressed as a small integer or rational number. The

frequency ratio for a 2-D resonant scanner is the ratio of the z-axis' natural frequency to the y-axis' natural frequency. One to one Lissajous patterns can be created because the resonant single fiber scanner uses a standard circularly cylindrical optical fiber, so the z and y axes' natural frequencies are the same. By modifying the amplitude and phase of the z and y scan, the 1:1 Lissajous pattern can take on a variety of shapes such as skewed lines, rotated ellipses and circles. A spiral scan is created when the amplitudes of a circular scan are modulated in a triangle pattern while the phases are kept constant. A propeller scan can be generated with a single piezotube when the 1:1 Lissajous pattern creates a 45-degree skewed line with horizontal and vertical sinewaves of the same frequency, equal amplitude and phase. A standard raster scan can be created by combining a fast, horizontal scan and a galvo-mirror scanner for the slow vertical scan. These raster modes and their corresponding inputs is seen in the figure below:

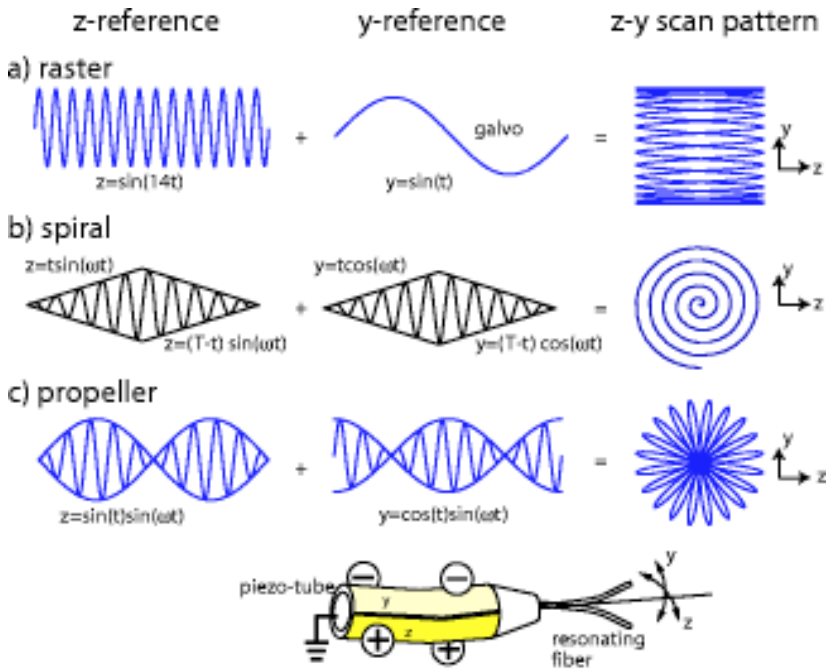

Figure 7. Scan patters with their inputs. a) raster scan b) spiral scan c) propeller scan

The quality of scans is very important for image acquisition applications. The dispersal or collection of the image data has to be synchronized with the position of the scan. Normally, the data or pixel collection starts at the beginning of the scan patterns and continues sequentially at a constant rate corresponding to the scan frequencies. However, due to piezotube and the resonant fiber dynamics the fiber can undergo large

displacements taking it outside the region of linear dynamic behaviour and forcing the scan outside of the known, regular and repeatable reference pattern resulting in image distortion. These non-linear dynamic effects can show up as amplitude dependent phase shifts, nonlinear amplitude response, amplitude jumps and whirls. Spiral and propeller scans are susceptible to amplitude dependent phase shifts and nonlinear amplitude response; manifesting as warped radial lines. The raster scan does not suffer as greatly from this effect because of its constant amplitude scan. Amplitude jumps are sudden changes in fiber tip amplitudes with the same drive frequency and amplitude. They can affect all three patterns. Whirl is defined as undriven out of plane response. It primarily affects the raster scan pattern because even though the fiber is being only excited horizontally, there may be a vertical response in addition to the horizontal vibration which cause the scan to take on a skewed linear, rotated ellipse or even a circular shape instead of the desired horizontal linear pattern. Both raster and propeller patterns can be continuously driven while the spiral pattern has to be stopped at the end of spiral and reset to the center [19].

The RGB laser light in a standard SFE configuration is typically combined at base station and coupled into the core of the single mode optical fiber by a fiberoptic combiner. The RGB illumination is comprised of 1mW blue (442 nm), 2mW green (532 nm), and 2mW red (635 nm). The lens assembly at the distal tip determines the maximum spatial resolution. It is aligned with the fiber scanner. The plane of sharpest focus is determined by the separation between fiber scanner tip and lens assembly. In order to achieve a large depth of focus that is more useful for determining anatomical features over relatively large distances, a low-NA endoscope lens assembly is used. The lens system can be further adjusted to accommodate 1-30mm for small lumens and 2-60mm for large lumens. The standard non-confocal geometry collects the backscattered light with a multitude of high-NA multimode optical fibers that are covering the outside surface of the tip assembly. The efficiency of the non-confocal SFE is dependant on the location, size and number of these optical collectors. A standard non-confocal set up can be seen in the picture below [18]:

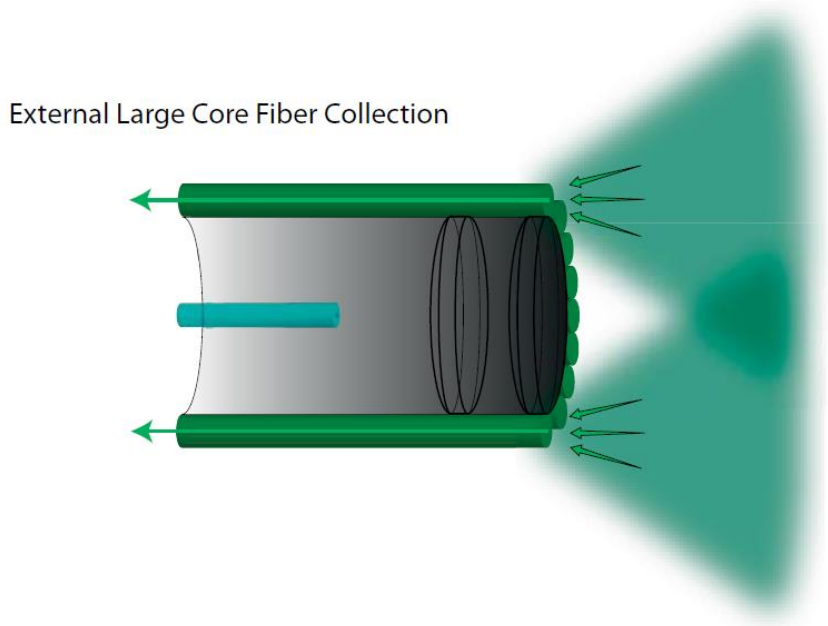

Figure 8. Optical collection method for a non-confocal external collection method

Reproduced with permission of John Wiley and Sons.

Early designs featured a ring of twelve 250 µm plastic optical fibers placed around the fiber scanner housing of approximately 1 mm in outer diameter to collect the backscattered RGB laser light, which extended the probe outer diameter to 1.6 mm. However, newer set ups feature a ring of 50 µm borosilicate glass optical fibers that reduce the probe overall diameter by 25% to 1.2 mm. Since the NA of both types of multimode collection fibers are roughly the same (0.6), the collection efficiency is reduced proportional to the total area of optical fiber cores. This loss of signal-to-noise ratio can be compensated to a degree by increasing the efficiency of light collection within the base station. Nevertheless, this reduces the range of high signal to noise imaging due to less collection area available to capture backscattered photons. Nevertheless, this reduction in size allows for complete exploration of the previously inaccessible areas and organs such as the main pancreatic duct for early detection of pancreatic cancer. This 1.2 mm SFE non-confocal endoscope can be seen in the figure below [7]:

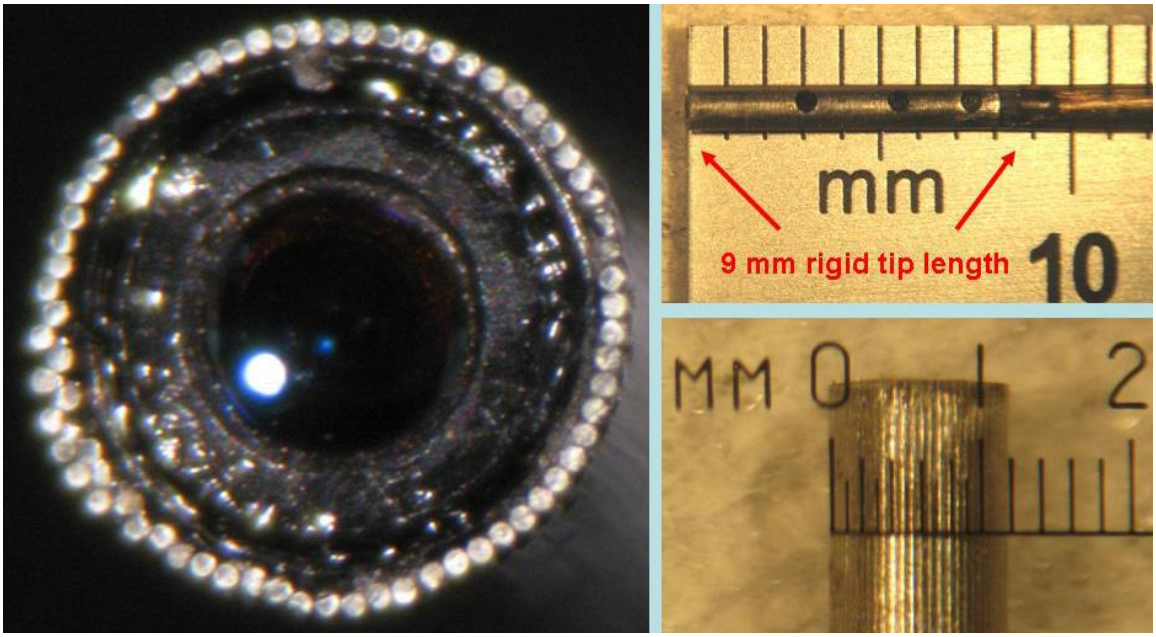

Figure 9. End view (left), side view (top right) and top view (lower right) of a 1.2 mm SFE

Proceedings Volume 6852, Optical Fibers and Sensors for Medical Diagnostics and Treatment Applications VIII; 685207 (2008); doi: 10.1117/12.765983

In summary, the non-confocal 1.2 mm SFE's unique design results in a device that can deliver relatively high-quality images; comparable to endoscopes with silicon image sensors at a very small form factor. It can produce up to 1000 lines per image, a wide field of view of 80-100 degrees, up to 30 Hz frame rate [7].

However, this design's size is limited by the piezoelectric actuator within it. Piezoelectric actuators produce very little amounts of deflection, requiring any piezoelectric actuator to use a stack of them to produce any meaningful displacement (0.4mm in this case). In addition, this device relies on numerous external multimode collector fibers situated around the housing which significantly contribute to its overall distal tip size. Therefore, a sub 500-micron device has to address both the actuation and collection methods in a novel way.

2.3. Thermal Actuation Methods

In micro-electromechanical systems (MEMS), thermal actuators are devices that create motion by utilizing thermal expansion. The increase in temperature is either achieved by electrical resistive heating of the actuator body itself or by using an external targeted heat source. Thermal actuators tend to generate a large force, compared to other MEMS actuators. However, displacements from linear thermal expansion is small. So, geometrical amplification is used to obtain larger, more useful displacements. One of the simplest and most common methods of geometrical amplification is the bent beam actuator shown below. This structure is also called a chevron actuator or a symmetric bent beam actuator [20].

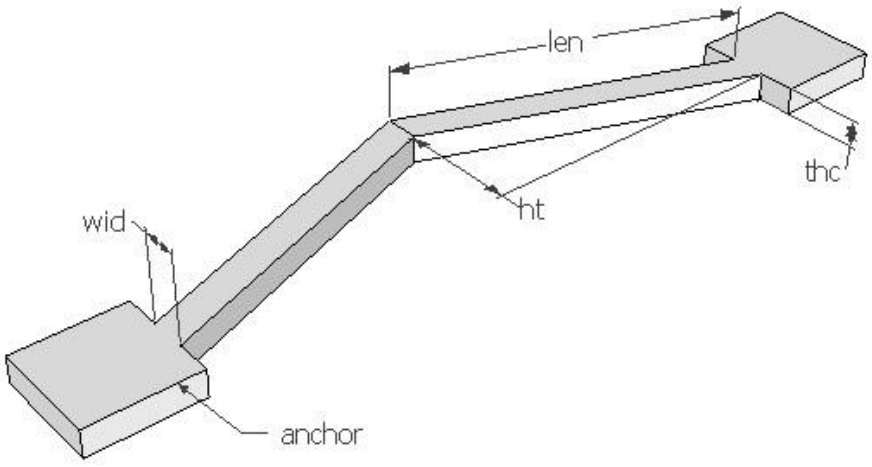

Figure 10. A chevron thermal actuator
Reproduced with permission of Institute of Physics Publishing.

The chevron beam is made of single crystal silicon or polysilicon in a clean room. The thin beam membrane is doped to a higher resistance than the anchors so that when current passes across the actuator from one anchor to the other, the thin beam heats up more than the anchors, linearly expanding. Beam geometry contributes to this as well. The maximum deflection is at the tip of the bent beam. When the power is cut off, anchors that have a lower resistance and are attached to substrate, act as a large body heat sink, cooling down the bent beam via conduction. In this set up, maximum temperature is observed at the tip of the bent beam while the anchors maintain a near constant temperature. To fabricate the actuator, usually the silicon wafer is patterned, doped and etched using Deep Reactive Ion Etching (DRIE) (among other techniques) to

create the movable parts with anchors being wider than other features. On another substrate that could be glass or another silicon wafer, the conducting layers are either etched or deposited using standard photolithography. Then the silicon wafer with the actuator parts is bonded to the substrate using direct bonding if it is silicon and anodic bonding if it is glass. After bonding, the silicon wafer is thinned by chemical mechanical polishing to the desired thickness for the moving structures. Then, any other needed metal contact pads or layers are deposited. Finally, the thinned silicon layer is etched by DRIE to release the moveable structures. Any remaining sacrificial layer is usually removed via wet etching. Standard symmetrical thermal actuators feature many chevron actuators in order to increase the exerted force to the desired level. This, however, does not increase the displacement. The length of the beams and the angle between them dictate the actuation distance [21] [22] [23] [24].

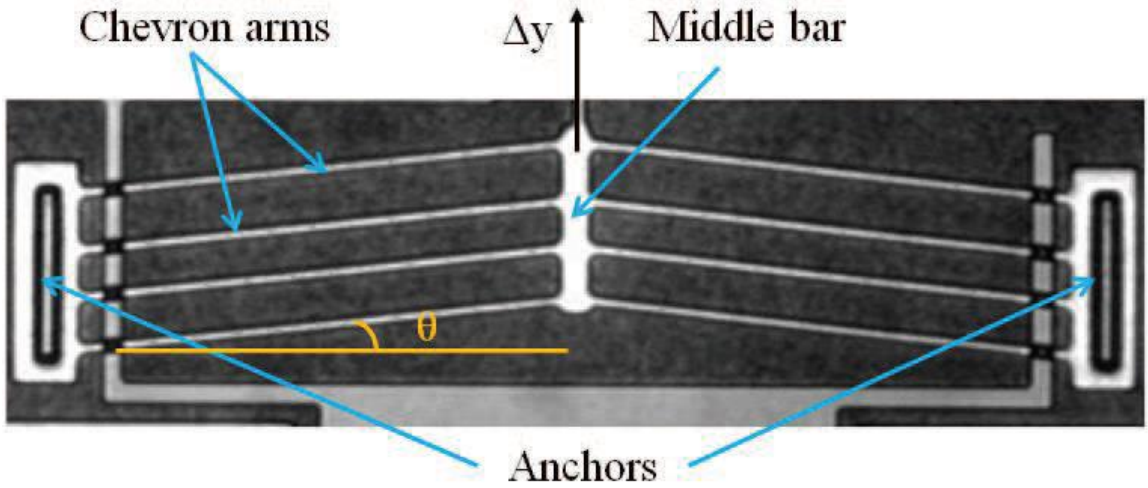

Figure 11. A standard symmetrical electro-thermal actuator

In actuator applications, bimorph or asymmetric actuators are another variation of thermal actuators (with some variations bimetal and bimorphs can be used as sensors, though, that application is not discussed here). They essentially work on the same principal. In bimorph actuators two beams with different resistance values are connected at the tip to each other. When current is passed through from one anchor point to the other, the beam with the higher resistance heats up more than the other side, bending the structure and thus creating actuation. In MEMS structures the resistance variation is created either by doping or by just simply having one beam thicker/wider than the other, resulting in a lower resistance. One such structure can be seen below [25]:

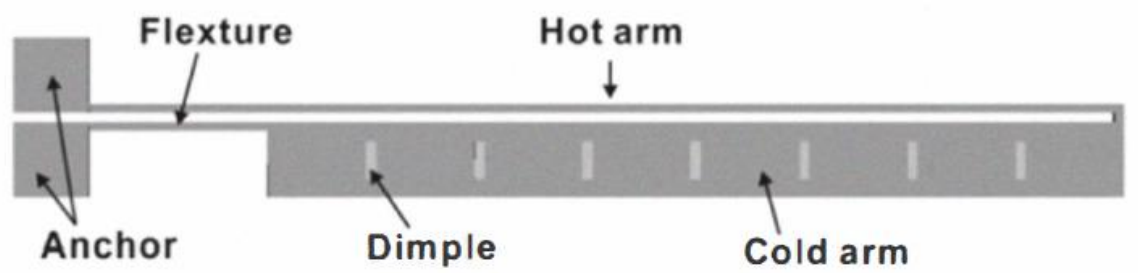

Figure 12. A silicon bimorph thermal actuator with a wide arm

Thermal actuators have a slower response time compared to capacitive, piezoelectric and magnetic actuators. There is a time delay between the application of voltage and temperature change. Time constants for heating and cooling of the structures, dictate the response time of the actuator. This is especially true for silicon doped actuators. For maximum displacement, the actuators are often heated up to hundreds of degrees Celsius [21].

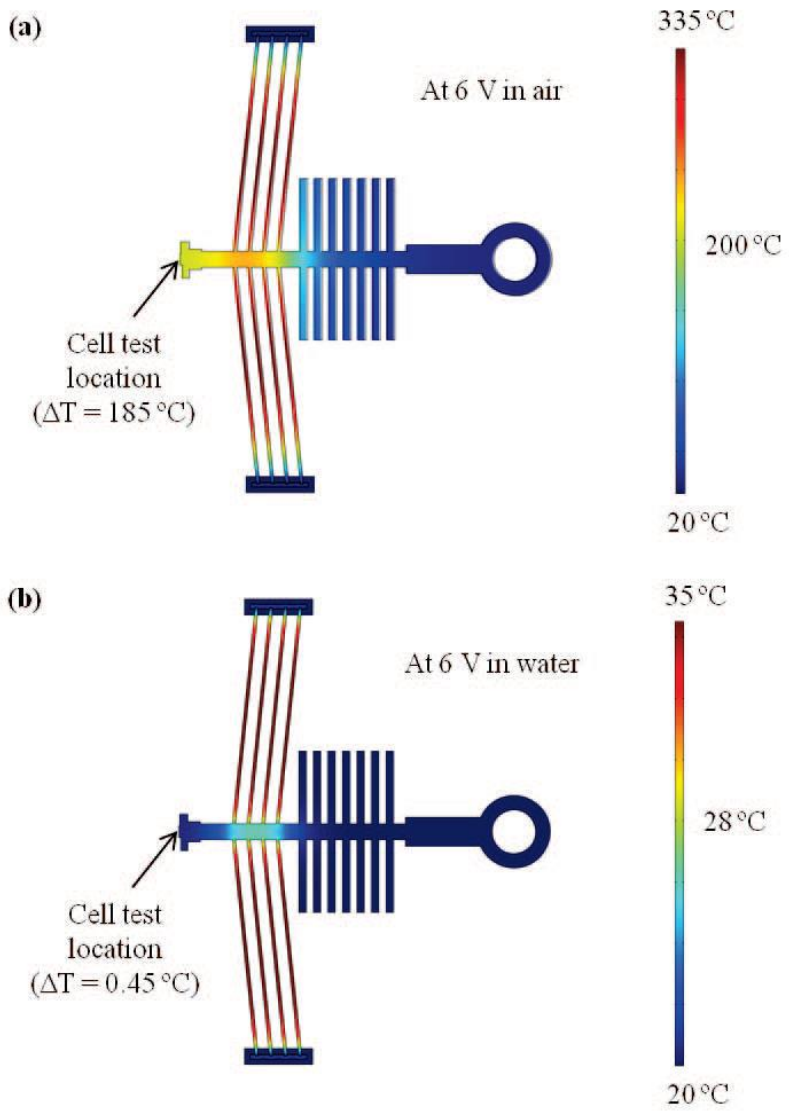

Figure 13. Temperature profile of an electro thermal actuator

This makes them not very suitable for high frequency applications. Furthermore, in all cases, their displacement is along the plane and they rely on their large anchor points to the substrate for support and cooling. So, even though the structures and actuators themselves are small, they need a large body (substrate) to act as a passive heat sink. This also makes it impossible to use them as free standing orthogonal actuators in tight spaces like those found inside of endoscopes [26] [27].

2.4. Research Done at Simon Fraser University Exploring Thermally Actuated SFE's

In the previous sections of this chapter, the main reasons why the current endoscopic technologies are still incapable of accessing many narrow passages in the body were presented. This leaves many patients with coronary and stroke conditions as well as people dealing with lung and pancreatic cancer with no choice but to go through with medically invasive and often uncomfortable procedures that affect their quality of life. Current SFEs have remained just over 1 mm in diameter mainly because of two factors. First reason, is the size of the piezoelectric actuator used in them and second, is the large number of multimode collection fibers placed on the outer edge of the housing. Komeili et al. [8] [9] [10] [11] [12] of MENRVA research group, which is the name of Dr. Menon's research lab at Simon Fraser University, proposes a novel design to address these issues in a series of papers. The work proposes using a novel free standing metallic actuator placed at the base of the vibrating illumination fiber and using the outer core of a dual channel single mode fiber as the light collector. This work lays the foundation for this project.

The work begins with the investigation of dynamic behaviour of a micro-cantilever that is transversely excited at its base. The base excitation is provided by thermal cycles causing thermal expansion. In this model, the actuator is placed underneath a flat cantilever beam. The actuator is assumed to be connected to the conductors beneath it which heat up the actuator via Joule effect. The actuator is assumed to be a block of solid material that contributes to the vibration response through its stiffness. The dimensions are chosen to be close to what would be needed if it was to become a very small endoscope. This set is displayed below [9]:

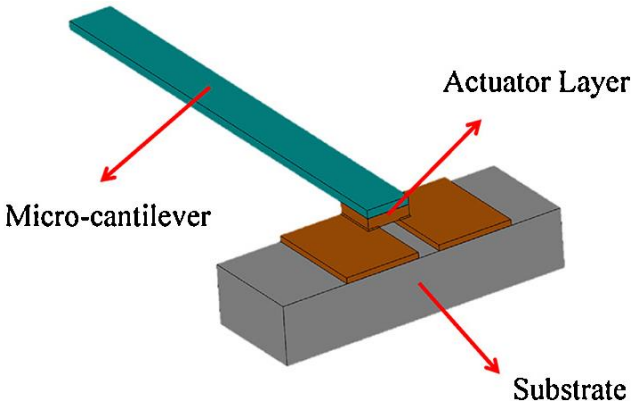

Figure 14. Geometry of the cantilever and actuator
Reproduced with permission of Elsevier.

The Euler-Bernoulli equation along with corresponding boundary conditions is used to model the continuous cantilever beam. The beam is assumed to be made of silica and the actuator is aluminum. The effect of the surrounding gas or liquid as well as the thermal expansion and stiffness of the actuator at the base are considered for the resultant boundary value problem. A closed-form analytical model is developed to compute the natural frequencies, mode shapes, and harmonic response of the vibrating cantilever and the quality factor. Then, the formulations are implemented in numerical codes written in Python. This analytical model is then used to investigate the prominent factors of the actuator as well as how big of a role the surrounding ambient fluid is playing on the dynamic response. The results of this analytical model were then compared to that of a 2D finite element analysis (FEA) using ANSYS to cross verify the proposed numerical models' accuracy for predicting the cantilever's vibrating behaviour. The comparison of the closed form formula and ANSYS for the effects of the ambient fluid on the cantilever system's natural frequency can be seen in the following figure [9]:

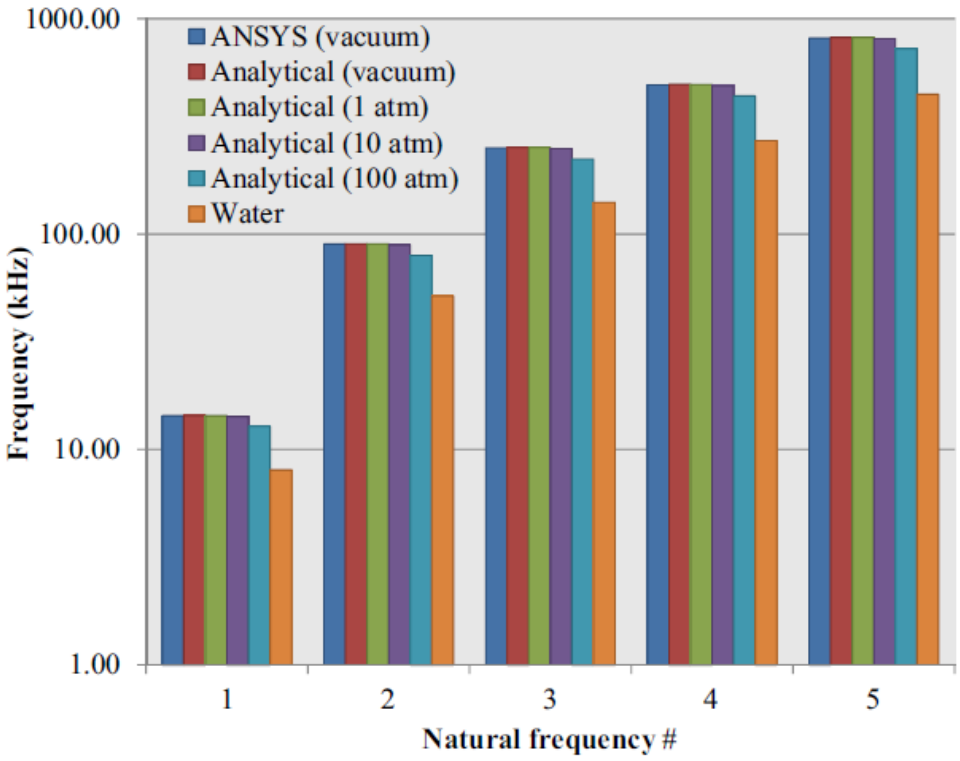

Figure 15. The natural frequencies obtained from the closed analytical solution in different ambient fluids compared to 2D finite element ANSYS model

Reproduced with permission of Elsevier.

It was observed that increasing he density of the ambient fluid reduces the damped natural frequency. Though, this only becomes noticeable at very high pressures and was negligible at vacuum and low pressure.

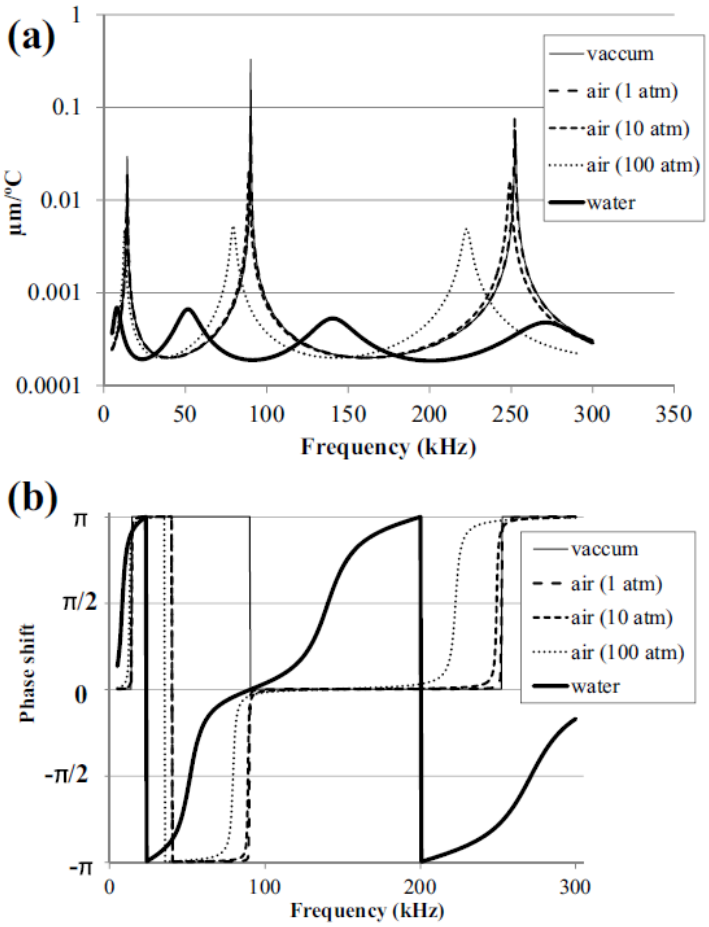

Figure 16. Harmonic response of the cantilever; (a) Displacement at tip, (b) Phase shift

Reproduced with permission of Elsevier.

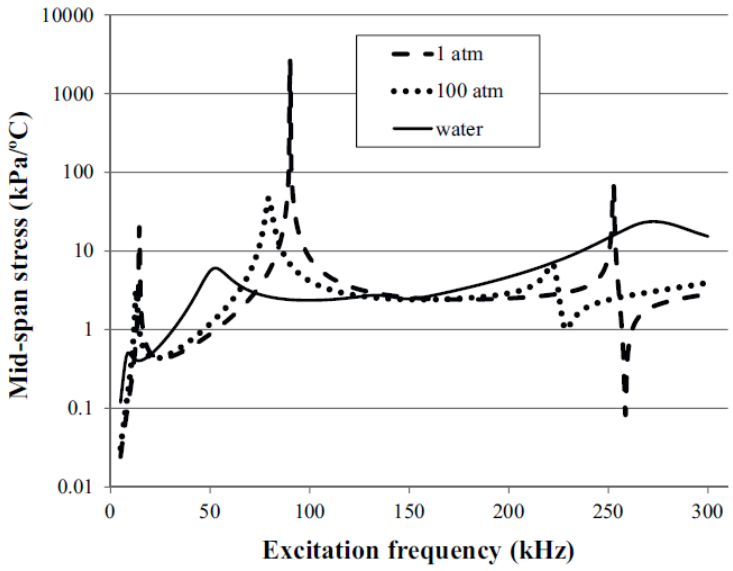

Figure 17. Maximum stress at the mid-span of the cantilever
Reproduced with permission of Elsevier.

Similarly, it was found that at low pressures, for the dynamic response, in terms of tip displacement and mid-span stress, the effect of air can be neglected. Essentially, increased density will have a noticeable effect on the resonance frequency, amplitude of vibrations and the phase shift. The quality factor of the system was studied in this paper as well [9]. It was found that the increase in pressure also negatively affected the quality factor. In summary, the thermal base excitation of a micro-cantilever was studied and numerical models for characterizing its natural frequency, modes, harmonic response and quality factor were developed. The formulations were verified by cross referencing them against FEA results and were shown to be accurate.

These numerical models were further developed in Komeili et al. [8]. This work uses the same model and set up as Komeili et al [9] and expands on it to derive and include the heat conduction equations in a one-dimensional solid medium which represents the actuator along with Euler-Bernoulli continuous beam equation for the micro-cantilever. Laplace transformation was used to resolve the time-dependency of the equations and solve the resulted ordinary differential equations. Then, the method of direct numerical integration was used to find the inverse Laplace of the complicated form of the field variables like the temperature distribution in actuator and displacement along the beam. This made it possible to model and analyze the resonance response of the cantilever under thermal base excitation. First, the actuator was subjected to a unit step

function to assess its response time. Its response was found to be in the order of a few micro-seconds. Furthermore, applying a periodic sinusoidal and square thermal cycling input in the order of a few kHz to it, showed the temperature changes closely follow the input [8].

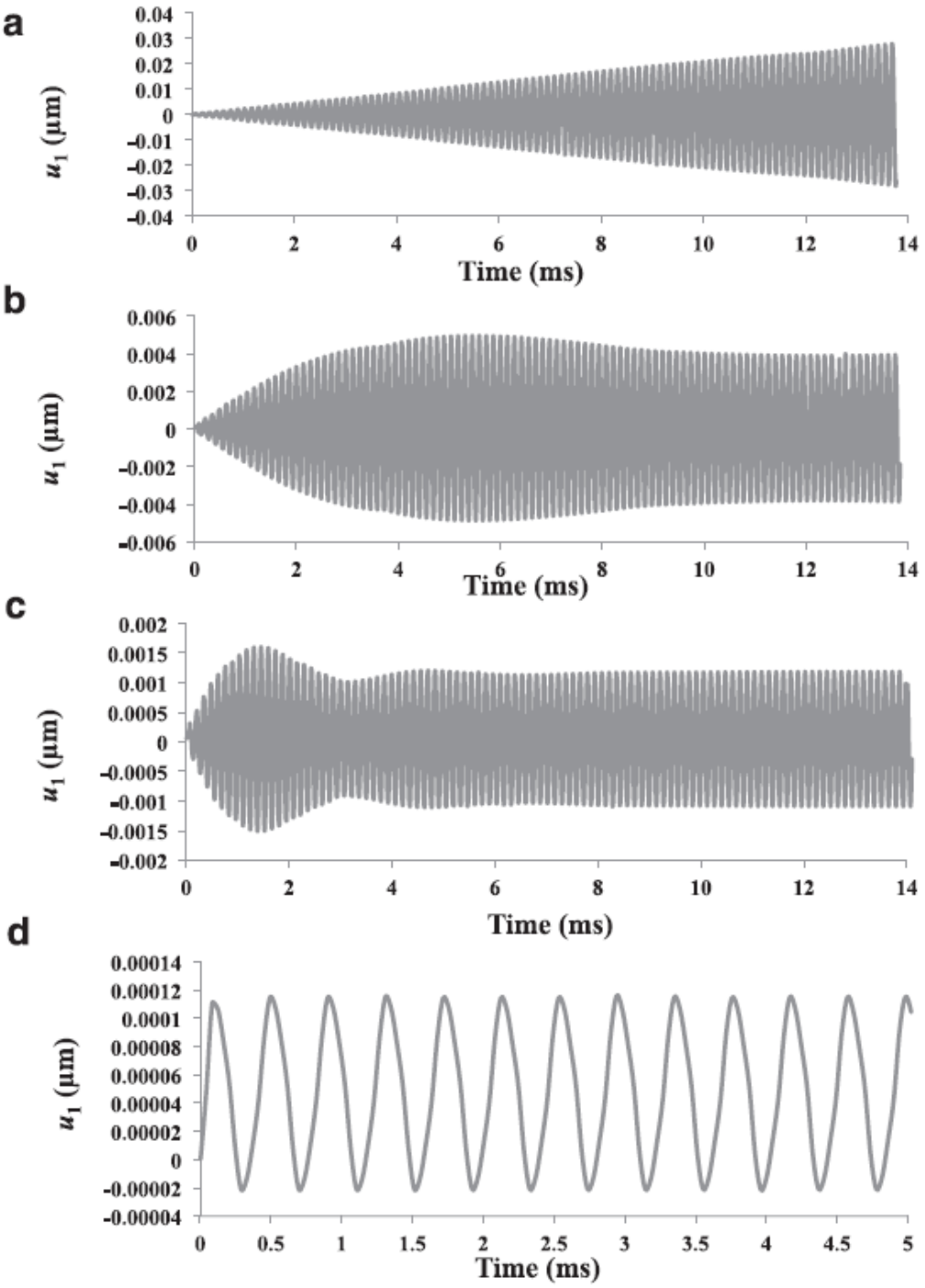

Figure 18. Dynamic response of the cantilever tip to periodic excitation when exposed different fluid mediums; (a) vacuum; (b) air 1 atm; (c) air 10 atm; (d) water

Reproduced with permission of Elsevier.

In addition, the tip displacement response of the micro-cantilever to periodic inputs under various environments was examined. It was shown that increasing the density and/or viscosity of the ambient fluids results in lower amplitudes of vibration except in the no-damping case which increases forever (definition of natural frequency; i.e. no damping). These results were also validated by comparing their results to that of FEA analysis using ANSYS [8]. In these models, the actuator's heat sink was assumed to have a constant temperature. This imperfect approximation results in unlimited heat flow at the boundary.

Satisfied with the numerical models, the work explores the effects of actuator shape and configuration on tip displacement in Komeili et al. [11]. A straight beam with two actuation layers on top and bottom which utilize the bimorph effect to induce bending and one with a long actuator perpendicular to the beam at its base are considered. These two configurations can be seen below [11]:

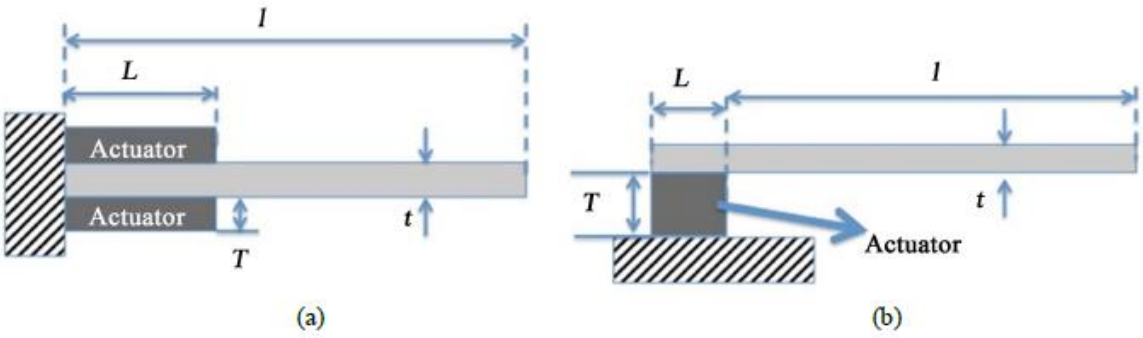

Figure 19. The two configurations considered; (a) Configuration A; (b) Configuration B

Komeili, M. and Menon, C. (2016) Analysis and Design of Thermally Actuated Micro-Cantilevers for High Frequency Vibrations Using Finite Element Method. *World Journal of Mechanics*, **6**, 94-107. doi: 10.4236/wjm.2016.63008. Licensed under Creative Commons 4.0

A specific vibrating frequency is considered (8 kHz) in order to study vibrational behavior and thermo-mechanical efficiency of micro-cantilevers as a function of their geometrical parameters and input power. The analysis is conducted on a 2D model of the selected configurations to examine their modal and transient coupled response. The results show that in both configurations the effect of thermal convection from ambient air can be ignored partly because of the small area of the surfaces as well as the high frequency thermal cyclic input. Therefore, conduction to the base is the only dominant factor in heat transfer. The dynamic response is recorded over a certain number of cycles to ensure the system is in steady state. Both configurations show a proportional

response in displacement and hot spot temperature to input power. However, the magnitude of both displacement and max power is significantly different. Configuration A results in more displacement at the cost of a higher hot spot temperature when compared to configuration B. On the other hand, a direct correlation between actuator length and thickness can be seen in configuration B where the tip displacement is increases when actuator thickness is increased, or actuator length is decreased. In summary, these findings, show it is possible to achieve the desired high level of displacement from a thermal actuator in a small form factor and underline the importance of optimizing the shape and size of the actuator [11].

The subsequent work, is a culmination of all the previous work to study the transient response of an optical fiber at resonance due to thermo-mechanical actuation [10]. The optical fiber is modeled as a cylindrical cantilever beam that is excited by cyclic expansions and contractions from the resistive heat generated inside of the actuator. The actuator system is modeled as a bent conductive wire at the base of the fiber as seen below [10]:

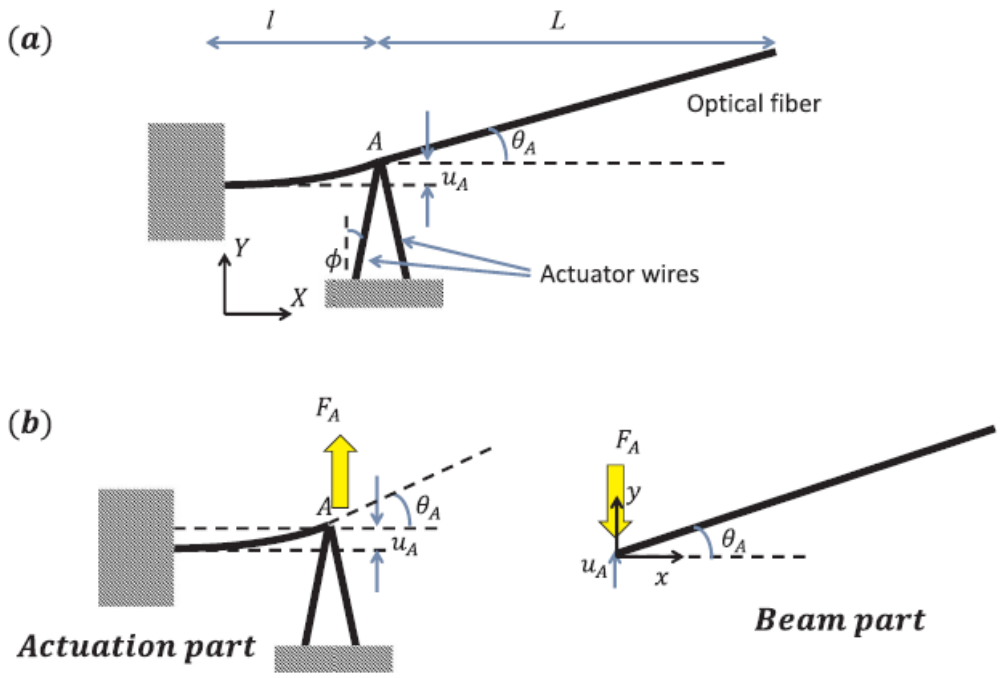

Figure 20. Mechanical model of the wire actuator; (a) geometry of the thermal actuator; (b) schematic of the actuation and beam parts and their interaction

Reproduced with permission of Elsevier.

To simulate this system, time dependent heat conduction equation for the actuator is solved. This results in a time dependent heat distribution and thermal expansion profile of the actuator. Then, a fully dynamic model of the optical fiber which takes into account the hydrodynamic forces from the surrounding fluid medium is developed using a continuous beam equation. The aforementioned equation is solved with respect to its boundary conditions to get the time dependent dynamic response of the optical fiber. Similarly, to Komeili et al. [8] Laplace transformation and its numerical inverse via direct integration have to be used to address the time dependency of the partial differential equations. This results in a mathematical model to predict the temperature oscillations inside the actuator as a function of time. The thermal expansion of the actuator is used to calculate the magnitude of displacement on the fiber. This makes the prediction of response of the system to any arbitrary time-dependent input possible [10].

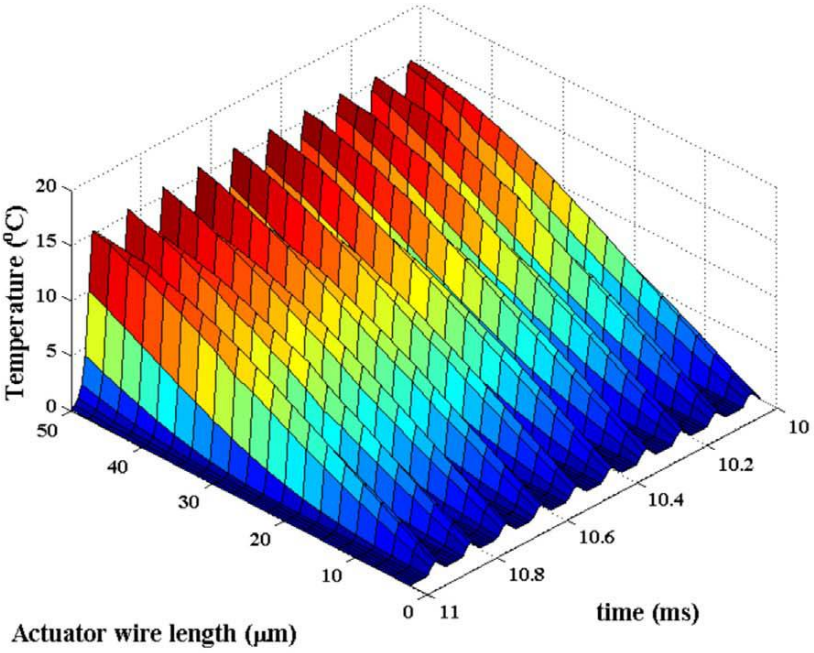

Figure 21. Temperature change of aluminum at the top of actuator as a function of time and actuator length (periodic excitation, 10 kHz)

Reproduced with permission of Elsevier.

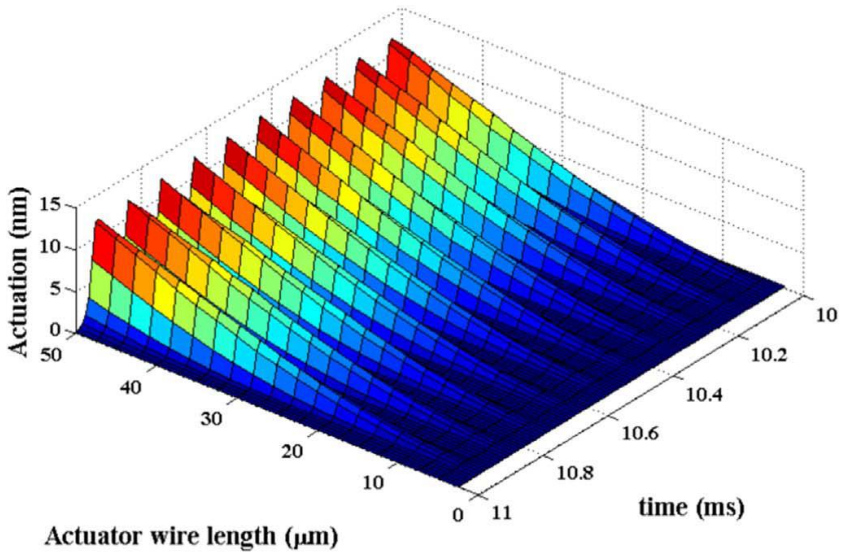

Figure 22. Actuation magnitude of aluminum as a function of time and actuator length (periodic excitation, 10 kHz)
Reproduced with permission of Elsevier.

From the results we can conclude that under periodic excitation and constant input power, the temperature and actuation amplitude increase with actuator length but only to a point. Past a certain length, the magnitude of temperature oscillations and actuation oscillations start to plateau (due to heat dissipation limits). This critical length of the actuator is a function of material properties, mainly thermal diffusivity and excitation frequency [10].

The analytical model is cross referenced against a 3D FEA ANSYS model for validation. Then, the effect of hydrodynamic force from the surrounding ambient fluid on the performance of the beam was studied considering all the new parameters. The results were found to be consistent with the previous findings [8] [9]. In general, a denser and more viscous fluid decreases the natural frequency, time to reach steady state, and the magnitude of displacements [10]. In this simulation it is assumed the heat sink (connected to the base of the actuator wires) is a perfect conductor as well and its temperature does not increase over time.

The final work, Komeili et al. [12] expands on the previous findings to further study how the physical characteristics of the actuator and its placement and alignment to the cantilever beam affect the oscillations. Modal analysis using 3D FEA in ANSYS is

used to optimize the design of a vibrating micro-cantilever using a resistive bent metal wire for thermal actuation. By isolating all other factors and varying one, it was found what parameters affect the natural frequency and tip displacement more than others. For natural frequency of the system, beam diameter and length were the most important factors as expected. For tip displacement it was found an offset in the alignment of the actuator to the cantilever beam was as significant as beam dimensions, emphasizing the need for precise assembly and placement. These results can be used to factor in and control parameters than contribute to the overall variation in prototypes significantly [12].

In summary, Komeili et al. developed a mathematical model to predict the dynamic response of a micro-cantilever to cyclic thermal actuation. The results were verified by comparing them to that of an ANSYS FEA simulation. It was concluded that based on the results, it would be possible to laterally vibrate a micro-cantilever to resonance and get the desired displacement while maintaining the small foot print needed for the proposed endoscope tip enclosure.

Chapter 3. Theoretical Foundations

This chapter presents a summary of the expanded mathematical models and aims to be more thorough in scope and consider more parameters than the work presented in section 2.4. These analytical models lay the groundwork for this project.

All the work outlined in this chapter other than setting the boundary conditions and changes to the physical model from the ones in section 2.4. and figures 31-32 are Mojtaba Komeili's. This chapter constitutes his work in a paper by Komeili, Ahrabi and Menon [28].

3.1. Resonance Vibration of an Optical Micro-Cantilever Using Electro-Thermal Actuation

In order to study the resonance excitation of an optical fiber actuated by a conductive wire and analytically model its behaviour, the continuous Euler-Bernoulli beam equation with the effect of surrounding fluid medium is formulated as a boundary value problem. The natural frequencies of the system and its harmonic response are further explained analytically. The results are validated using ANSYS FEA once again. The obtained analytical solutions are used to predict the response of the system and make suggestions to optimize its performance.

3.1.1. Analytical model

To be able to analytically model the system, the shape and dimensions of the system must be defined first. The figure below shows the schematics of the optical fiber (micro-cantilever) and actuator system:

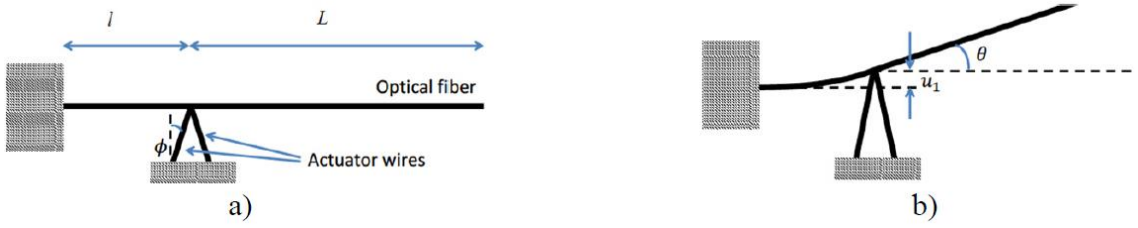

Figure 23. (a) Geometry of the micro-cantilever system (b) actuation mechanism

As seen in the figure, the actuator is attached underneath the beam at a distance, l, from the clamp point and it is extended over length, L, from the actuation point. In this model, the actuating conductive wire is assumed to be triangular as opposed to 'U' shaped. Since, coefficient of thermal expansion only relies on linear expansion along the direction of movement, modelling it as a triangle simplifies the calculations while not reducing the accuracy of the model (simplifies the actuator mesh geometry). Temperature rise inside the actuator caused by current moving through the thin wire and subsequent resistive heating leads to thermal expansion and eventually a displacement of u_1 at the top of the actuator which acts as a load/displacement perturbation at point $x = l$ along the length of the micro-cantilever. Repeated heating and cooling of the actuator results in cyclic excitation of the beam and subsequently its lateral vibration. When the frequency of excitation matches that natural frequency of the beam, resonance occurs, and large amplitudes of vibrations are obtained in the beam. This allows the system to reach magnitudes of deflection that it would normally not be able to achieve at a lower power. Therefore, the study of the free vibration as well as the harmonic response of the system is crucial for an optimized design. In this analysis, the system is split into two parts; the actuation part and the beam part. First, the governing equations for both are developed and then the equations are combined to come up with the general dynamic equation of the system. The actuation part consists of the fixed end of the beam to where the actuator is situated (i.e. $x < l$) and includes the actuation wire as well. The beam part is the span of the beam after the actuator (i.e. $l < x < l + L$).

Actuators in this system act as longitudinal stiffness elements placed underneath the beam. So, stiffness of each actuator wire, K_{wire}, is given by:

$$K_{wire} = \frac{A_{wire}E_{wire}}{L_{wire}} \quad (2)$$

Where A_{wire}, L_{wire}, and E_{wire} are the cross-sectional area, length and Young's moduli of each individual wire, respectively. These elements are acting as parallel springs (with an angle) in conjunction with the section of beam from the clamp point to the connection point (i.e. $x = l$). From basic beam deflection equations and tables, the stiffness of this section of the beam, K_{beam}, can be found [29]:

$$K_{beam} = \frac{3E_{beam}I}{l^3} \quad (3)$$

Where E_{beam} and I are the Young moduli of beam material and the second moment of inertia of beam cross section. Similarly, the slope at the end point of the actuation section, θ, can be found via:

$$\theta = \frac{F_b l^2}{2E_{beam} I} = \frac{3}{2l} u_A \quad (4)$$

Where F_b shows the total reaction, force applied on the beam inside the actuator part with length l, from actuator wires and the beam part. Taking into account the combined effects of force and thermal expansion and using the superposition method, the displacement at the top of the actuator can be represented as:

$$u_A = u_A^F + u_A^T \quad (5)$$

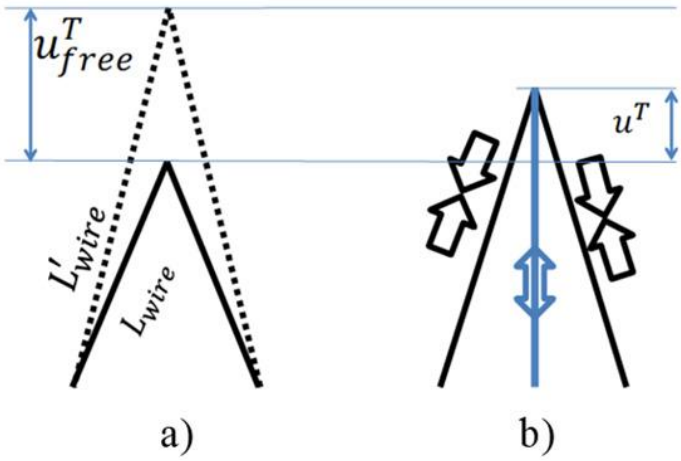

Figure 24. (a) Thermal elongation in the actuator wire if not connected to beam; (b) Effective thermal elongation in the actuator connected to the beam

In Eq. (5), u_A^F represents the component of displacement from the applied forces between actuator part and the beam part, and u_A^T is the displacement due to temperature change and elongation in the actuator. According to superposition, each can be found by ignoring the other and solving the mechanics of materials equations with respect to that particular effect. For example, the relation for the applied interaction force between actuator part and the beam part, F_A, and the force induce displacement, u_A^F, is found by the following:

$$u_A^F = \frac{F_A}{2K_{wire}\cos(\emptyset) + K_{beam}} \quad (6)$$

Where ∅, is the angle made between actuator wires and vertical axis (Fig. 23).

In order to find u_A^T superposition can be used again to find the total displacement at the top of the actuator. First, without the beam stiffness, u_{free}^T is found as shown in Fig. 24(a). From basic geometry, length of the actuator wires after temperature change, denoted as L'_{wire} can be formulated as:

$$(L'_{wire})^2 = L_{wire}^2(1 + \alpha_{wire}\Delta T)^2 = [L_{wire}\sin(\emptyset)]^2 + [L_{wire}\cos(\emptyset) + u_{free}^T]^2 \quad (7)$$

Where α_{wire}, is the coefficient of linear thermal expansion for the actuator material and ΔT is the change in the temperature. Expanding the above equation and ignoring the terms with $O(\alpha^2)$ and $O([u_{free}^T]^2)$ results in the linearized equation:

$$u_{free}^T = \frac{L_{wire}\alpha_{wire}\Delta T}{\cos(\emptyset)} \quad (8)$$

It is important to note that u_{free}^T is a free expansion without any force involved. Nevertheless, including the beam stiffness that resists this displacement, results in compression in the actuator elements and upward elastic deflection (tension in the analogous stiffness element) in the beam section of the actuation part. This interaction results in a middle ground displacement between 0 and u_{free}^T found via:

$$u_A^T = \frac{2K_{wire}\cos(\emptyset)\,u_{free}^T}{2K_{wire}\cos(\emptyset) + K_{beam}} \quad (9)$$

Combining equations (5), (6), and (9), the governing equation in the actuator part (i.e. actuation part model) that relates reaction force (F_A), degree of freedom (u_A), and thermal actuation (ΔT) can be defined as:

$$\begin{aligned} F_A &= [2K_{wire}\cos(\emptyset) + K_{beam}](u_A - u_A^T) \\ &= [2K_{wire}\cos(\emptyset) + K_{beam}]u_A - 2K_{wire}L_{wire}\alpha_{wire}\Delta T \end{aligned} \quad (10)$$

The equation of motion for a long narrow beam, given small deformations is [30]:

$$E_{beam}I\frac{\partial^4 u(x,t)}{\partial^4 x} + m\frac{\partial u^2(x,t)}{\partial t^2} = q(x,t) \quad (11)$$

Where $u(x,t)$ is vertical displacement along the beam; m is the weight per unit length of the beam, and distributed load on the beam (from surrounding fluidic forces along the beam) is denoted by $q(x,t)$. The spatial coordinates, x and t, are the coordinates along the length of the beam, and time, respectively. The above equation can be solved with the initial and boundary conditions. As shown in Fig. 22(b), the following boundary conditions can be identified for this beam:

$$u(x,t)|_{x=0} = u_A, \quad (12a)$$

$$\theta = \frac{\partial u(x,t)}{\partial x} = \frac{3}{2L}u_A, \quad (12b)$$

$$V(x)|_{x=0} = EI\frac{\partial^3 u(x,t)}{\partial x^3}\bigg|_{x=0} = -F_A$$
$$= -[2K_{wire}\cos(\emptyset) + K_{beam}]u_A + 2K_{wire}L_{wire}\alpha_{wire}\Delta T, \quad (12c)$$

$$M(x)|_{x=L} = E_{beam}I\frac{\partial^2 u(x,t)}{\partial x^2}\bigg|_{x=L} = 0, \quad (12d)$$

$$V(x)|_{x=L} = E_{beam}I\frac{\partial^3 u(x,t)}{\partial x^3}\bigg|_{x=L} = 0, \quad (12e)$$

Where V and M represent the shear force and bending moment on beam cross section respectively. To solve the Eq. (2), the method of separation of variables [31] can be utilized via replacing $u(x,t) = w(x)g(t)$. Note that this system is vibrating under small deformation and only free vibration and harmonic response are tackled. The time dependent component is substituted by its harmonic form, $g(t) = e^{i\omega t}$. This results in the following forms of the equation of motion for the beam:

$$E_{beam}I\frac{\partial^4 w(x)}{\partial^4 x} - m\omega^2 w(x) = Q(x,\omega) \quad (13)$$

The harmonic form of hydrodynamic forces on the micro-cantilever, $Q(x,\omega)$, is represented by the following general form equation [32]:

$$Q(x,\omega) = \frac{\pi}{4}\rho\omega^2 b^2\Gamma(\omega)w(x) \quad (14)$$

Where ρ is the density of the fluid medium, b is the dominant length scale (diameter for a circle and width for a rectangle), and $\Gamma(\omega)$ is a dimensionless function. This equation can be stipulated through solving the fluid motion equations around a rigid beam. Therefore, for a beam with a circular cross section an analytical solution for $\Gamma(\omega)$ is [33]:

$$\Gamma(\omega) = 1 + \frac{4iK_1(-i\sqrt{iRe})}{\sqrt{iRe}K_0(-i\sqrt{iRe})'} \quad (15)$$

Where $Re = \rho\omega b^2/(4\eta)$, and $K_i(x)$ is the modified Bessel function of second kind, and η is the viscosity of the fluid.

Therefore, Eq. (13) can be simplified to the following form:

$$\frac{d^4w(x)}{d^4x} - \beta^4 w(x) = 0, \quad (16a)$$

$$\beta^4 = \frac{m\omega^2 + \frac{\pi}{4}\rho\omega^2 b^2\Gamma(\omega)}{E_{beam}I} \quad (16b)$$

Which is a fourth order differential equation with the following generic homogenous answer:

$$w(x) = C_1\sin(\beta x) + C_2\cos(\beta x) + C_3\sinh(\beta x) + C_4\cosh(\beta x) \quad (17)$$

Where the C_i coefficients are the constants of this equation; they can be determined by the boundary conditions. In the boundary conditions, Eq. (17) results in the following algebraic form:

$$C_2 + C_4 - u_A = 0, \quad (18a)$$

$$\beta C_1 + \beta C_3 - \frac{3}{2l}u_A = 0, \quad (18b)$$

$$-EI\beta^3 C_1 + EI\beta^3 C_3 + [2K_{wire}\cos(\emptyset) + K_{beam}]u_A = 2K_{wire}L_{wire}\alpha_{wire}\Delta T, \quad (18c)$$

$$-C_1\sin(\beta L) - C_2\cos(\beta L) + C_3\sinh(\beta L) + C_4\cosh(\beta L) = 0, \quad (18d)$$

$$-C_1\cos(\beta L) + C_2\sin(\beta L) + C_3\cosh(\beta L) + C_4\sinh(\beta L) = 0 \quad (18e)$$

These five equations can be summarized in a matrix form to explain the effect of surrounding fluids:

$$Ax = b \quad (19)$$

Where:

$$A = \begin{bmatrix} 0 & 1 & 0 & 1 & -1 \\ \beta & 0 & \beta & 0 & -3/(2l) \\ -EI\beta^3 & 0 & EI\beta^3 & 0 & D_1 \\ -\sin(\beta L) & -\cos(\beta L) & \sinh(\beta L) & \cosh(\beta L) & 0 \\ -\cos(\beta L) & \sin(\beta L) & \cosh(\beta L) & \sinh(\beta L) & 0 \end{bmatrix}, \quad (20a)$$

$$x = \{C_1 \;\; C_2 \;\; C_3 \;\; C_4 \;\; u_1\}^T, \quad (20b)$$

$$b = \{0 \;\; 0 \;\; D_2\Delta T \;\; 0 \;\; 0\}^T, \quad (20c)$$

$$D_1 = 2K_{wire}\cos(\emptyset) + K_{beam}, \quad (20d)$$

$$D_2 = 2K_{wire}L_{wire}\alpha_{wire} \quad (20e)$$

The free vibration (modal) analysis of the micro-cantilever is done with no external load on the system. This is achieved by replacing $\{b\} = \{0\}^T$. In this case, the resulting form of Eq. (19) has a non-trivial zero answer only when the determinant of A is zero ($|A| = 0$). Therefore, for the free vibration of the beam the following characteristic equation is extracted:

$$1 + \cos(\beta L)\cosh(\beta L) + \frac{E_{beam}I\beta^2}{D_1}\left\{\frac{3}{2l}\sin(\beta L)\sinh(\beta L) - \beta[\sin(\beta L)\cosh(\beta L) - \cos(\beta L)\sinh(\beta L)]\right\} = 0 \quad (21)$$

This characteristic equation reduces to the equation of a simple cantilever beam (i.e. $1 + \cos(\beta L)\cosh(\beta L) = 0$) if $D_1 \to \infty$, which can be used to verify it. Also, note that $l \to 0$ has the same effect, as it makes $K_{beam} \to \infty$ and therefore $D_1 \to \infty$, after solving the indeterminate form of $0 \times \infty$, it again reduces to the characteristic equation for a regular cantilever beam. The complexity of this non-linearity equation makes it unsolvable analytically; therefore, numerical methods are used to solve it. Eq. (21) has

multiple complex roots in the form of $r = \omega_d - i\epsilon$, where ω_d is the damped natural frequency, and ϵ is the attenuation (damping) in the system [34].

To find the harmonic response of the system, the following form of harmonic loading is imposed on system in Eq. (20):

$$b = \begin{Bmatrix} 0 \\ 0 \\ D_2\overline{\Delta T}e^{i\omega t} \\ 0 \\ 0 \end{Bmatrix} \quad (22)$$

Note that this represents a simplified form of the thermal excitation relying on the following assumptions:

First, the electrical current supplied to the actuators, to generate heat through resistive heating, can be sinusoidal/harmonic. However, because of the nature of the thermal conduction, the resulting temperature changes are not (forgoing the second harmonic). Furthermore, there is non-homogeneity in the temperature distribution along the length of actuator. The assumption of perfect sinusoidal $\Delta T(t)$ is a simplification of a more complex function. Nevertheless, due to the small time-constant of micro-scale systems [35], the temperature changes in the actuator can be adjusted rapidly according to the magnitude of electrical current and steady-state can be achieved rapidly.

The second assumption is, active cooling cannot be practically implemented in this system. However, assuming that after achieving steady-state, there is a base temperature and $\Delta T(t) = \overline{\Delta T_0} + \overline{\Delta T}e^{i\omega t}$, where ($\overline{\Delta T_0} \geq \overline{\Delta T}$), the above formula can be valid for the harmonic part. The constant static deformation due to the steady-state temperature increase ($\overline{\Delta T_0}$), can be calculated easily and added to the dynamic response via the superposition of static and dynamic deformation. Only the harmonic part of mechanical displacement is considered.

Even though Eq. (19) can be solved analytically to find the closed form of C_i coefficients, the resulting closed forms lead to complex terms that do not reduce the complexity of algebraic equations and numerical computations. On the other hand, using a numerical matrix solver package for direct evaluation of C_i coefficients from its matrix form proved to be computationally and programmatically more efficient. The numerical

linear algebraic (linalg) modules of NumPy package in Python programming language are used for this purpose here.

In addition to displacement that is directly calculated from the Eq. (17), the stress inside the beam can be found via [36]:

$$\sigma(x, z, \overline{\Delta T}) = -E_{beam} z \frac{\partial^2 w(x, \overline{\Delta T})}{\partial x^2} \quad (23)$$

Therefore:

$$\sigma(x, z, \overline{\Delta T}) = E_{beam} z \beta^2 [C_1 \sin(\beta x) + C_2 \cos(\beta x) - C_3 \sinh(\beta x) - C_4 \cosh(\beta x)] \quad (24)$$

In which z is the distance from the natural axis of the beam.

The quality factor is also studied to investigate the efficiency of this system. Quality factor, Q, is defined as [37]:

$$Q = 2\pi \frac{U_s}{U_d} \quad (25)$$

Where U_s, is the maximum stored energy and U_d, is the energy loss over one cycle. Hence, we have:

$$U_s = |U_k + U_b|, \quad (26a)$$

$$U_k = \frac{1}{2} K_{beam} u_1^2 + K_{wire} \cos(\emptyset) \, (u_1 - u_{free}^T)^2, \quad (26b)$$

$$U_b = \frac{1}{2} \int_0^L E_{beam} I \left(\frac{d^2 w(x)}{dx^2} \right)^2 dx \quad (26c)$$

Note that, U_k is from the total elastic energy stored in the actuation section, and U_b is for the elastic bending energy stored in the beam part. By using the general form of $w(x)$ function in Eq. (17) and having C_i coefficients, the answer to this integral is found to be:

$$U_b = \frac{1}{4}EI\beta^3\left\{C_1^2\left[\beta L - \frac{\sin(2\beta L)}{2}\right] + C_2^2\left[\beta L + \frac{\sin(2\beta L)}{2}\right] - C_3^2\left[\beta L - \frac{\sinh(2\beta L)}{2}\right]\right.$$
$$+ C_4^2\left[\beta L + \frac{\sinh(2\beta L)}{2}\right] + 2C_1C_2[1 - \cos^2(\beta L)]$$
$$- 2C_1C_3[\sin(\beta L)\cosh(\beta L) - \cos(\beta L)\sinh(\beta L)]$$
$$- 2C_1C_4[1 + \sin(\beta L)\sinh(\beta L) - \cos(\beta L)\cosh(\beta L)]$$
$$- 2C_2C_3[\sin(\beta L)\sinh(\beta L) + \cos(\beta L)\cosh(\beta L) - 1]$$
$$- 2C_2C_4[\cos(\beta L)\sinh(\beta L) + \sin(\beta L)\cosh(\beta L)]$$
$$\left. + 2C_3C_4[\cosh^2(\beta L) - 1]\right\} \quad (27)$$

In this system the dominant energy loss is due to the hydrodynamic force, fluid drag. Therefore, energy loss over one full cycle is equal to the work done by the fluid force:

$$U_d = \int_{x=0}^{L}\oint q(x,t)dudx = \int_{x=0}^{L}\int_{t=0}^{T} re\big(Q(x,\omega)e^{i\omega t}\big)re\big(i\omega w(x)e^{i\omega t}\big)dtdx \quad (28)$$

Where $re(z)$, refers to the real value of complex number z, and $T = f^{-1}$ is the period of cycles in oscillatory motion. Solving this integral analytically is a tedious task. Therefore, it is solved using numerical integration in Python using the NumPy package.

Alternatively, if the dissipative effects in the fluid is small (i.e. $Q \gg 1$) the following approximation can be used:

$$Q_n = \frac{\frac{4m}{\pi\rho b^2} + re(\Gamma(\omega_n))}{im(\Gamma(\omega_n))} \quad (29)$$

Where $im(z)$, is the imaginary component of the complex number z, and Q_n is the quality factor at n^{th} natural frequency with ω_n.

3.1.2. Analytical results

The analytical formulations presented in the previous section are used to study the behaviour of the micro-cantilever and draw conclusions on the design of the scanning fiber. The derived mathematical models for the effect of prominent geometrical

factors and the performance of the system in terms of deflections at resonance frequency and harmonic response are implemented in numerical codes using open source NumPy and SciPy libraries of Python programming language.

In order to find the damped natural frequencies of the micro-cantilever, its harmonic response, and quality factor, the following initial and boundary conditions were used. The cantilever beam is made of pure silica ($E = 73$ GPa, density $\rho = 2200$ kg/m^3) and the actuator wire is made of pure aluminum ($E_{base} = 71$ GPa, and $\alpha = 4.0 \times 10^{-5}$1/ºC). The geometrical dimensions used for this study are: optical fiber (micro-cantilever) length ($L = 800$ µm), diameter ($d = 10$ µm), the actuator distance from clamp point ($l = 100$ µm). For the actuator part: actuator wire length (at least $L_{wire} = 100$ µm), diameter ($d_{wire} = 100$ µm), and an actuator wire angle ($\emptyset = 25°$) are chosen. Air and water and considered for the ambient fluid with $\eta_{air} = 1.98 \times 10^{-5}$ Pa· s and $\eta_{water} = 0.0014$ Pa· s, and $\rho_{air} = 1.024$ kg/m^3, $\rho_{water} = 998$ kg/m^3. According to gas laws, the effect of ambient air pressure is reflected as an increase in the density while air viscosity is assumed to have negligible changes due to pressure.

The figure below shows the natural frequencies of the system with the dimensions given above for a surrounding fluid of vacuum, air in 1 and 10 atm, and water:

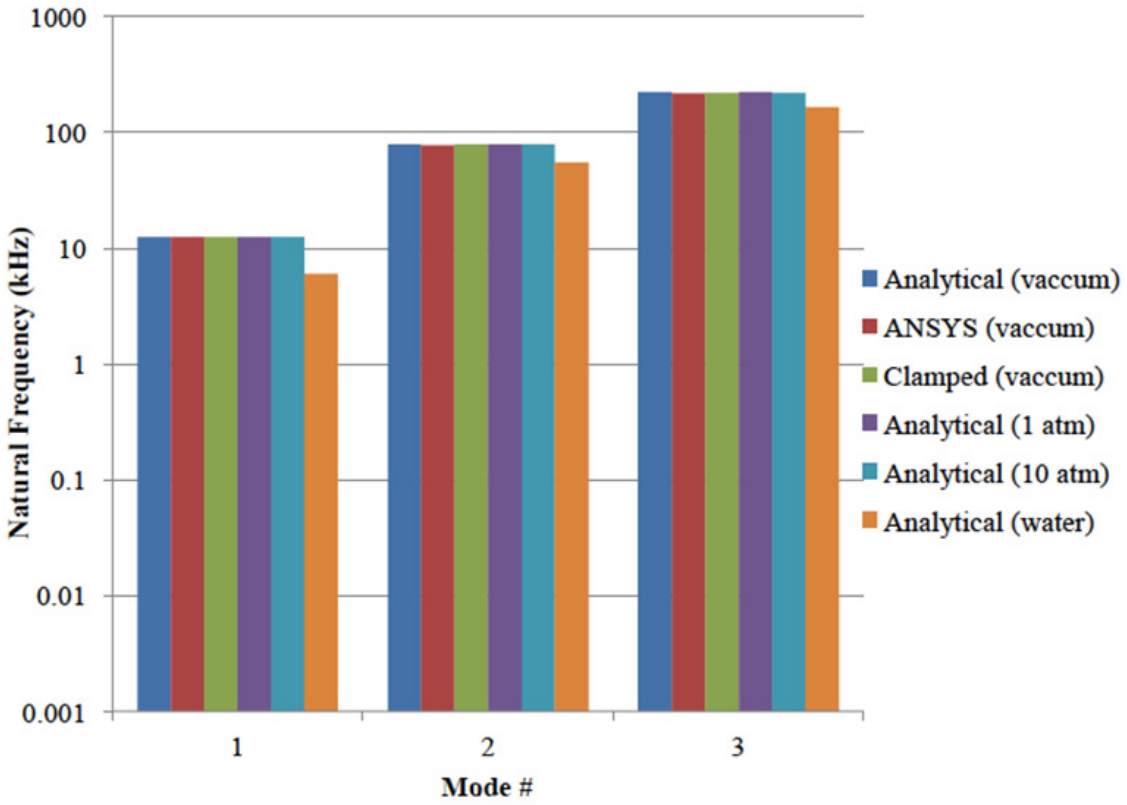

Figure 25. First 3 natural frequencies obtained from the analytical model in vacuum and different fluid mediums, compared to FEM model

The drop in natural frequency when the system is exposed to denser fluids is clearly visible. This can be because of the fact in a denser fluid, more mass needs to be displaced during vibration, which in turn increases the effective mass of the system thus decreasing its natural frequency. These results are consistent with the results obtained in Fig. (15) from Komeili et al. [9]. However, denser fluids seem to have less of factor on the natural frequency based on the new calculations. A comparison to the natural frequencies obtained from a FEA ANSYS model is shown below:

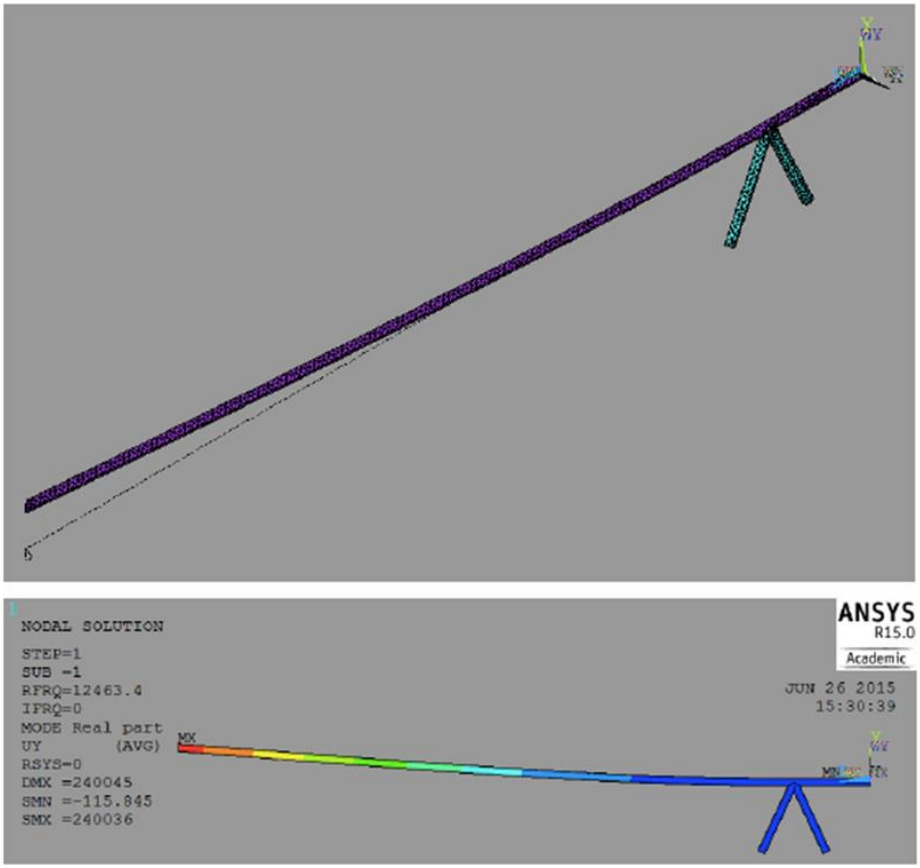

Figure 26. A FEA model used to verify the natural frequencies calculated from the mathematical model

Additionally, this comparison shows that this system, at least in terms of natural frequency, resembles a clamped beam with length L. More investigations on the effect of actuator wires (dimensions and stiffness) as well as distance of the actuator to clamp point, l, shows that these parameters have a negligible effect on the natural frequency.

The eigenvalues of Eq. (19) are used to find the mode shapes of the corresponding natural frequencies. The figure below depicts the aforementioned mode shapes found analytically compared to those obtained in ANSYS:

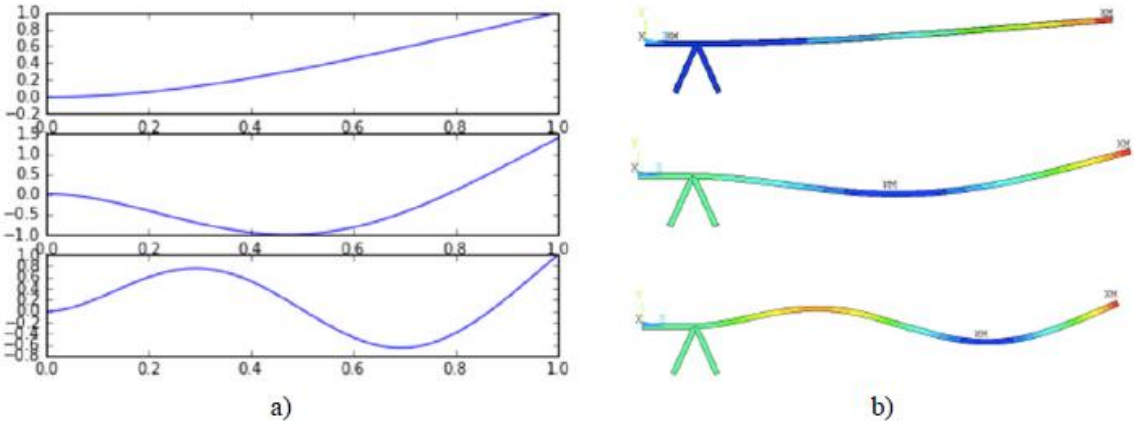

Figure 27. The first three mode shapes obtained via (a) analytical solution (b) ANSYS

Note that only flexural modes are considered and not torsional or longitudinal modes.

Harmonic response of the beam over a frequency range of 0 to 300 kHz is studied for $\overline{\Delta T} = 1°C$. The results are compared to an analogous ANSYS model where the effect of thermal expansion is substituted by an equivalent cyclic force input. The figure below which displays the normalized amplitude of displacement at the tip point of the beam and the maximum stress ($z = \pm d/2$) at the mid-section of the beam (1 nm actuation), confirms the results match each other:

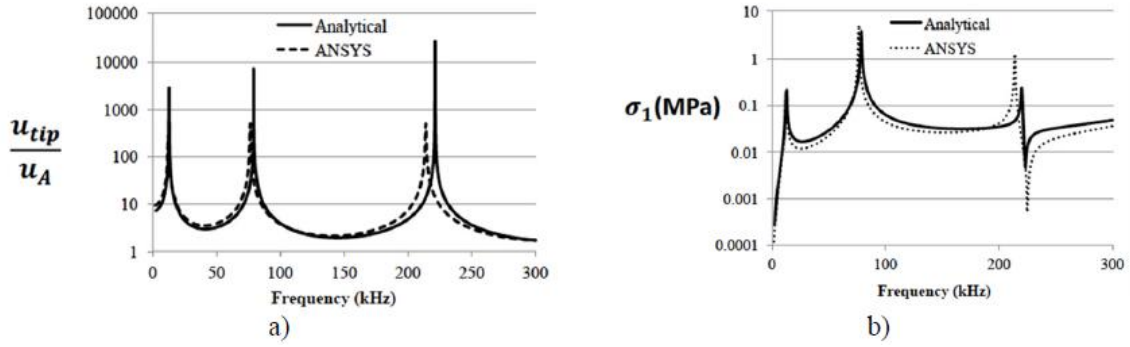

Figure 28. Harmonic response of the micro-cantilever obtained via analytical modeling and ANSYS; (a) tip displacement (b) stress magnitude

The harmonic response of the system with the dimensions specified above are compared to the case where the actuator wire length (L_{wire}), the actuation distance (l), and the actuator angle ($\emptyset$) are changed. Although, it was reported that these variables do not have a significant or noticeable effect on the natural frequency, the results show that they can substantially influence tip displacement and mid-span stress values. Jumps

in the magnitude of the displacement as well as stress at the frequencies that corresponds to the natural frequency are observed. This is due to the resonance phenomenon. It can be deduced that the response of the system is largely the same both in vacuum and air. However, there is a noticeable drop in magnitude of response at the resonance frequency because of the effect of damping which is particularly dominant at the resonance frequency [38].

The following figure displays the tip displacement of the micro-cantilever at its fundamental frequency as a function of actuator distance from the clamp point (l) for several values of actuator wire length (L_{wire}) at 1 atm air pressure:

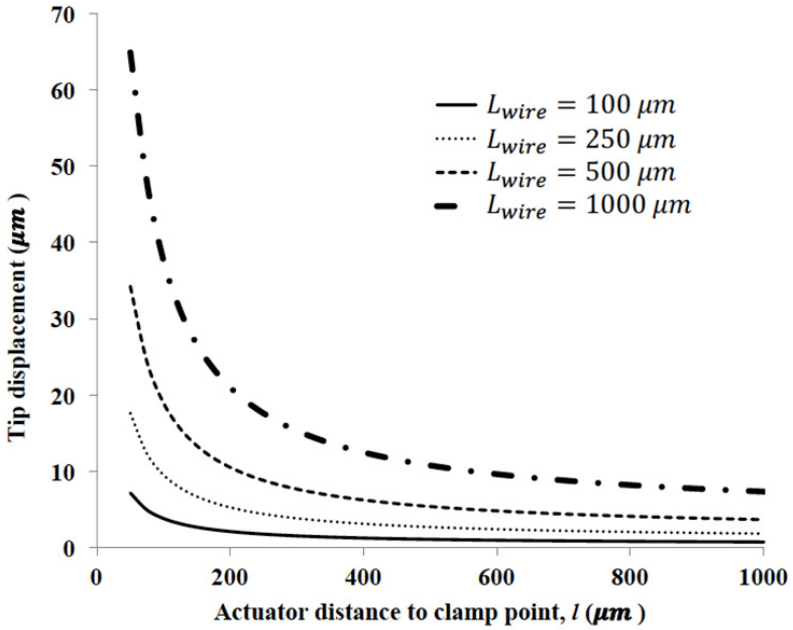

Figure 29. Effect of actuator distance from the clamp point and the length of actuator wire on the tip displacement magnitude at first natural frequency

It is evident that increasing the length of the actuator wire increases the tip displacement almost proportionally. This was expected from Eq. (8). On the other hand, the tip displacement falls drastically as a result of increase in the distance from the base. This can be seen in Eq. (4) since a shorter distance between the actuator and base increases the slope of the beam.

Calculated values for the quality factor of this system show that it is independent of the parameters of the actuation part and only depends on the beam part (its length and diameter) as well as ambient pressure and mode number (when other sources of

damping are ignored). The quality factor was calculated using the integration method described in Eq. (25-28). The following figure shows the quality factor for the first two modes of the system and changes in the length and diameter of the micro-cantilever:

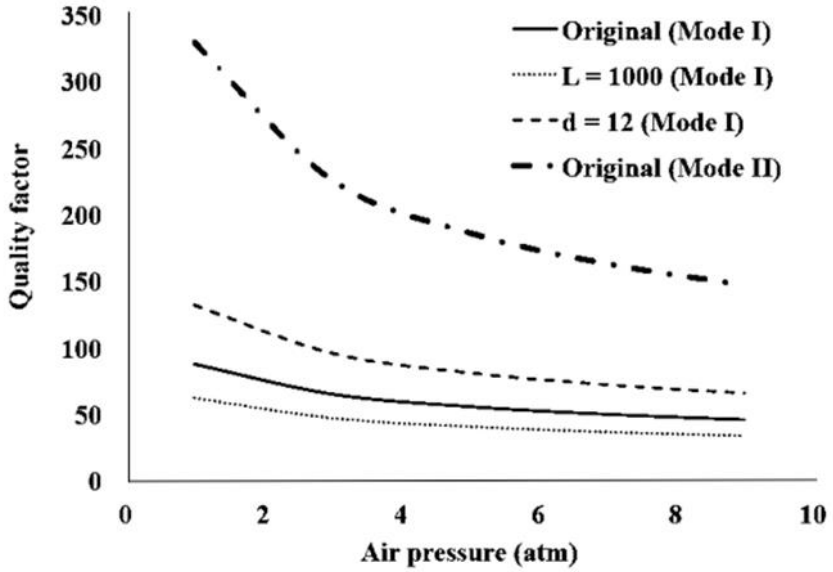

Figure 30. Effect of actuator distance from the clamp point and the length of actuator wire on the quality factor at the first natural frequency

Although each line represents a different resonance frequency depending on mode number and beam length or diameter, similar trends in quality factor can be noticed as a function of surrounding fluidic pressure (air). It was demonstrated in Fig. 25 that the effect of air pressure on the natural frequency in each system is minimal and negligible. However, a considerable change in the quality factor is observed in the case of increased air pressure. It results in a rapid decline of the quality factor initially, but this slows down as the magnitude of pressure is increased. Increasing the beam length and/or decreasing the beam diameter result in more displacement of the beam due to lower flexural rigidity (this will decrease the natural frequency however). Moreover, higher displacement amplitudes escalate the effect of drag force and eventually decrease the quality factor, as it is seen from the lines that represent increasing length ($L = 1000$) and decreasing diameter ($d = 12$).

3.2. Summary

A new actuation system for resonance vibration of an optical fiber at micro-scale is further studied in this chapter. The actuation method relies upon base excitation of a

micro-cantilever. Actuator wires are connected to the micro-cantilever at a location close to its base. Repeated cycles of heating and cooling in these wires induce small perturbations and vibrations in the micro-cantilever (optical fiber). When the frequency of the actuator matches the natural frequency of the fiber, resonance occurs, and it increases the deflections in the micro-cantilever substantially.

An analytical model was presented to find the natural frequencies of the system, mode shapes and its harmonic response, taking into account the effect of surrounding fluid. This model was compared to the finite element models created in ANSYS and verified to be effective in predicting the free vibration and harmonic response. This system is separated into the actuation part (actuators and length of beam before their connection point to beam) and the beam part (span of beam after its connection point to the actuators). Results of free vibration analysis showed that the dimensions of the actuation part have negligible effect on the natural frequencies. In fact, the natural frequency of the beam can be estimated from a simple cantilever beam with a total length equal to the length of beam section. On the hand, dimensions and factors in the actuation part have considerable effect on the harmonic response of the beam, which includes the deflections and the stress magnitudes. Parameters such as distance of actuator to the base and length of actuator wire can be used to optimize the mechanical response of the system while having no impact on the natural frequency. The quality factor in the system was reported to be independent of the actuation part and only dependent on the beam length and diameter as well the ambient fluid. It was concluded that increasing air pressure and/or decreasing the flexural rigidity of the beam results in lower quality factors. Nevertheless, due to the many simplifications and assumptions in the models, the main take away from this section are the models on resonance frequency.

Chapter 4. Feasibility and Preliminary Study of the Design

The work proposed by Komeili et al. [8] [9] [10] [11] [12] and the expanded models in Chapter 3 showed that it should be possible to reach resonance in a micro-cantilever using the novel approach of cyclic electro-thermal actuation using just a single conductive wire near its base. Even though, the results were cross verified by an FEA software, there were a lot of fundamental assumptions that were made that might not translate to a real-world scenario. In the models and simulations, the heat sink at the base of the actuating wire was assumed to have a constant or near constant temperature. It was also assumed to have a perfect thermal interface with the wire. The backend of the small fiber in the model was not simulated and was assumed to be completely rigid and fixed in place to represent a fixed-free beam (Euler-Bernoulli beam theory).

Therefore, there is a need for further study of the problem. The main goal of this chapter is to study the feasibility of resonance vibration of an optical fiber micro-cantilever using electro-thermal actuation. This is achieved by trying to verify the expanded analytical models in practice using prototypes made in the lab. The results of the analytical formulation and experimental observations are compared to each other to gauge the effectiveness of the suggested method. This chapter covers thesis objective number 1.

4.1. Experimental Verification of the Analytical Models

In order to verify the theoretical procedure and conclusions expanded in Chapter 3, a series of thermally actuated micro-cantilever prototypes were manufactured. A number of assumptions were made both in the previous research, presented in section 2.4., and work presented in chapter 3 and it is important to check these results against real-world results to test whether these assumptions were reasonable and whether they can be used to design the new endoscope tip enclosure.

To prove the concept, a number of prototypes of various sizes were produced in various configurations. To become familiarized with the process of handling the thin wires and to develop and come up with manufacturing methods that work, it was decided

to start at a larger scale and scale down incrementally; not as small as needed for the final design but with the same ratios and proportions.

In the original proposal and all the subsequent analytical models, only the beam made of an optical fiber and the actuator made of a rectangular shaped metal wire located near its base were modelled and realized and discussed. With an assumption that the wire is going through sinusoidal thermal cycles because of a current passing through it. The wire and actuating wire were also assumed to have approximately the same diameter. Therefore, with every other aspect of this proposal open to interpretation, initially, two small via holes were made on a copper FR-4 sheet using a Protomat machine. A Protomat machine is essentially a 2D CNC milling machine meant for prototyping and testing printed circuit board (PCB) designs before sending them out to a fabrication house. A 127-micron thick copper wire was routed through holes (500 microns apart), bent around a 250-micron fiber and soldered on the other side to test the structural rigidity of the loop. The ‘U’ shaped wire was assessed to be surprisingly rigid and resilient to bending moments. The backside of the board was milled into traces leading up to each hole to resemble the conducting wires. One can be seen in the figure below:

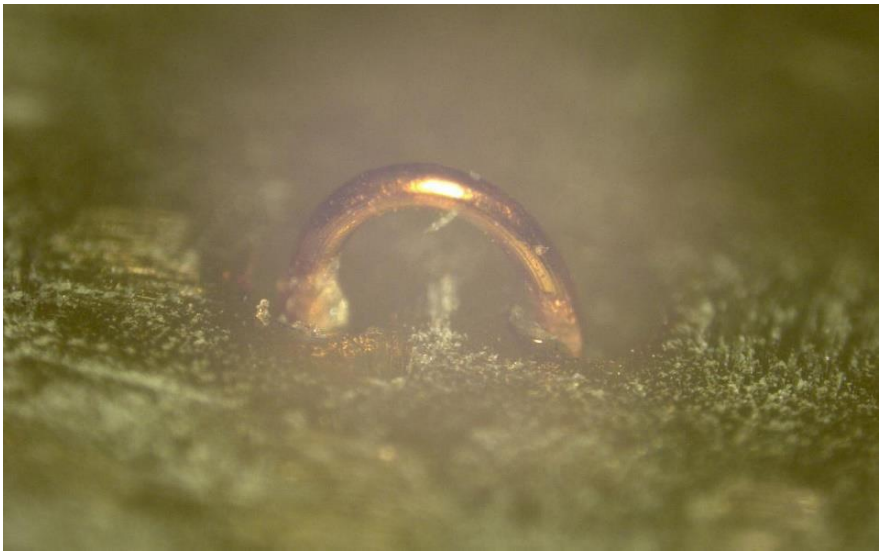

Figure 31. A copper loop made on a milled Protomat board

After making sure the small wire loops were structurally sound, the first attempts to make a working resonance cantilever wire prototype begun. Aluminum was used for the actuating wire in the analytical models due to its excellent thermal diffusivity.

However, at 127 microns, an aluminum wire (or most metals) would have such a low resistance that in order to heat it up to the desired temperatures, excessive and unsafe amounts of current would be needed. Therefore, for these large-scale samples a 127-micron thick nichrome wire was used. Nichrome (alloy of nickel and chromium) on the other hand, is extremely resistive and heats up with very little current, making it a suitable specimen for the large-scale models. Note that nichrome has very poor thermal conductivity but at larger scale the fiber itself has a much lower natural frequency (due to its increased length) and therefore, actuating wire's thermal conductivity is not as important.

The first working samples were made using nichrome. Initial nichrome samples used standard 125-micron thick optical fibers which were then scaled down to 50-micron fibers. The fiber is aligned over the bridge and then fixed in place with super glue. One of these very early samples can be seen below:

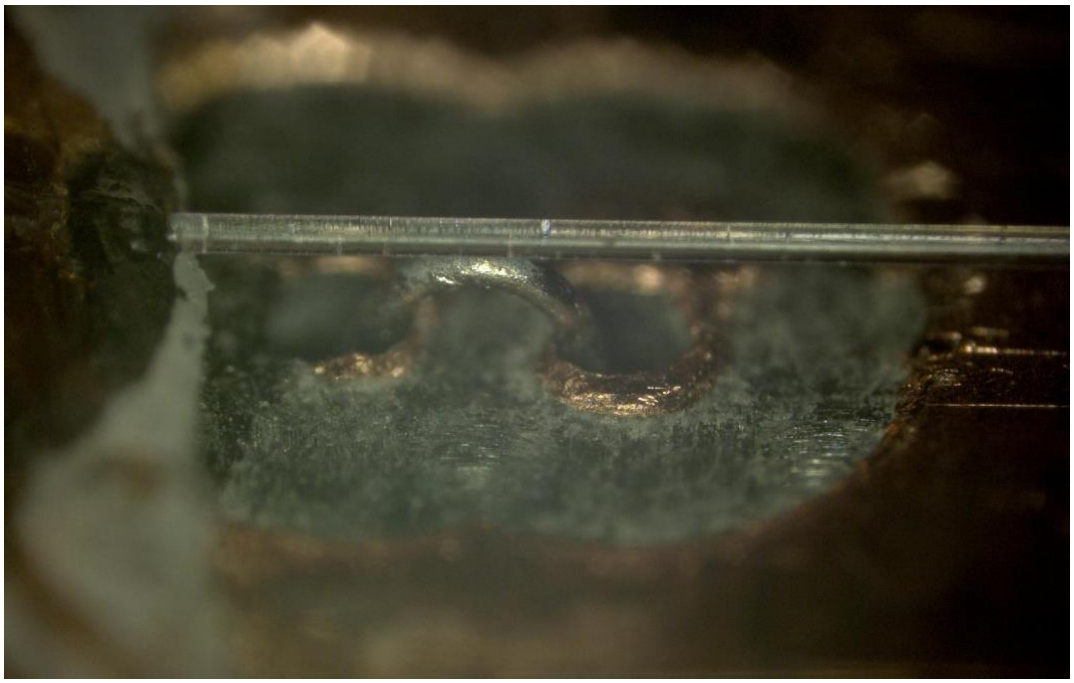

Figure 32. An early nichrome prototype. Standard 125-micron optical fiber, 127-micron thick nichrome wire, via holes 500 microns apart

In order to line up the fibers with the top of the wires, a platform with the exact height of the wire had to be made. To create the platforms, a CO_2 laser cutter system at Simon Fraser University's Engineering Science Lab was used. For this task, the behavior and response of the laser cutter to input needed to be characterized. On the

laser cutter, the user has the option of controlling the power of the pulse, the speed at which the laser moves and the PPI which is the laser pulse density per inch. The PPI number was set the max value of 1000 and the other two parameters were changed one by one. Various plexiglass sheets were etched with each setting and then their thicknesses were measured using a micrometer. The results were tabulated and graphed in order to get an equation for the thickness as a function of power and speed.

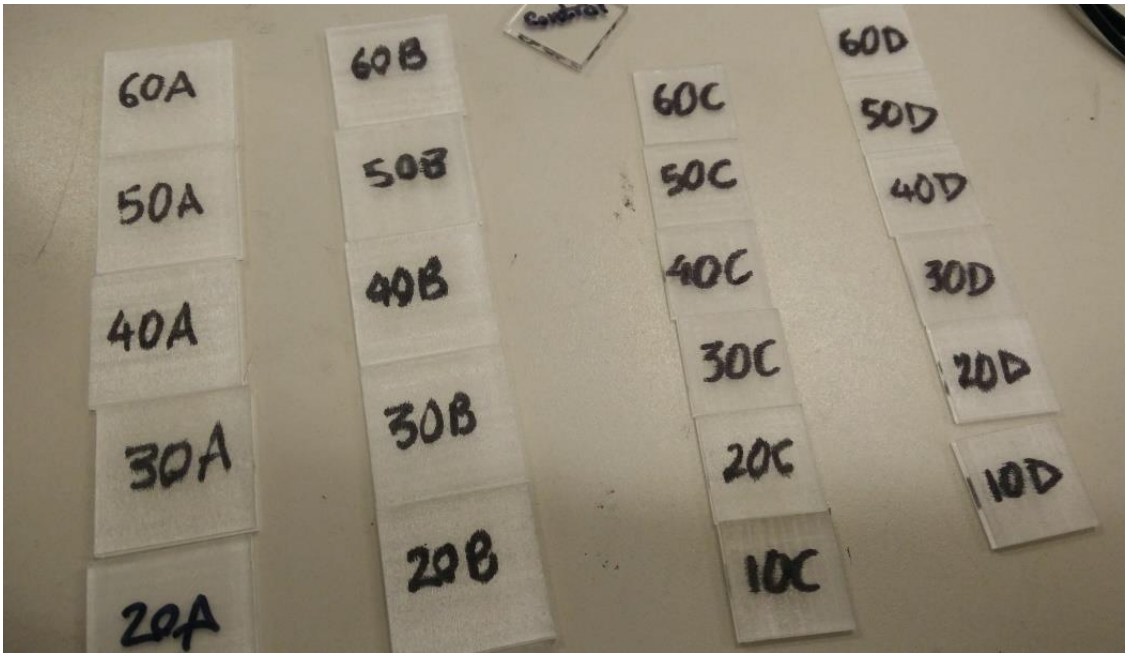

Figure 33. Some of the etched plexiglass pieces used to characterize the laser cutter

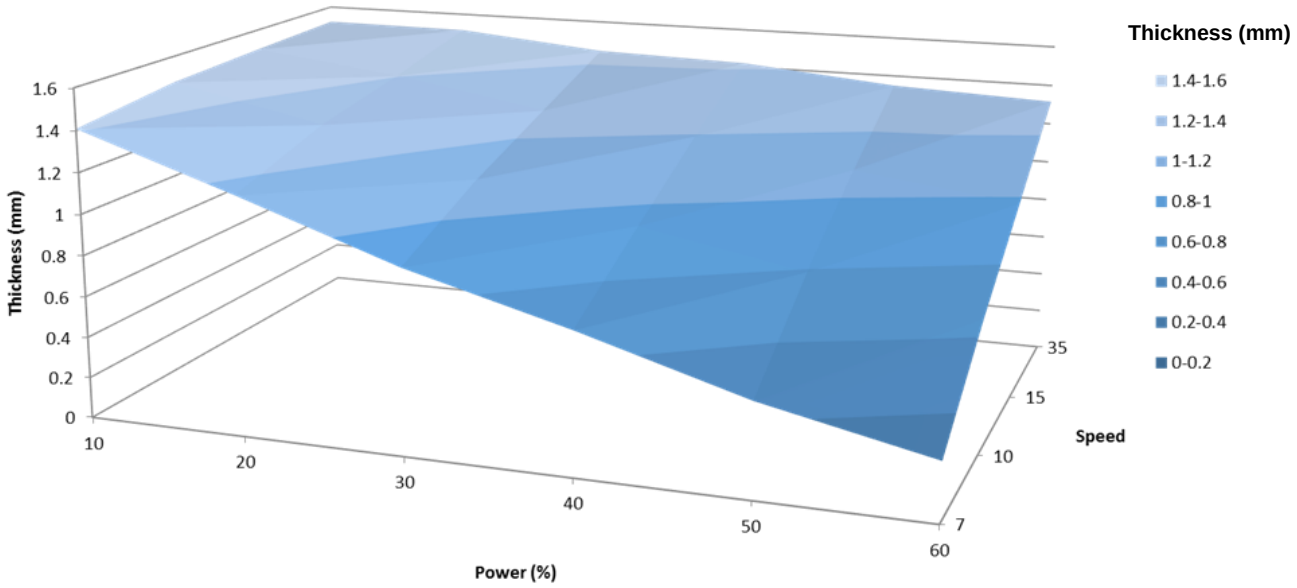

Figure 34. The resulting characterization graph of laser cutter as a function of power and speed; Power is given as percent of the total power of the laser and speed is an arbitrary unitless value in the controls UI.

The resulting graph showed that the parameters affecting the thickness of the laser cut plexiglass can be treated as a piecewise linear equation. This allowed for laser cut plexy platforms that are accurate to ± 10 micron of the desired thickness. After this stage, professional PCBs were made in order to bring down randomness caused by the unreliable Protomat machine. The PCBs were essentially just a flat platform with equality spaced lines on them for alignment purposes and just 2 via holes. The actuating wires were also scaled down to 50-micron stainless steel 302 wires at this point. Stainless steel 302 was used for the 50-micron prototypes because it is readily available, and it is very resistive.

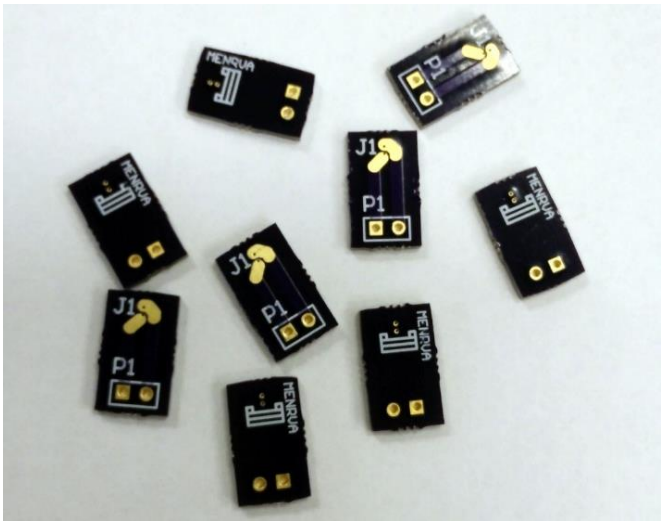

Figure 35. The first batch of PCBs made intended to be used as a platform

Note that neither stainless steel nor nichrome can be soldered to copper traces directly. For this reason, the ends of the wires had to be wrapped in nickel sheets, spot welded and then nickel sheets would be soldered to the coper pads to make the electrical connection.

A prototype made with this configuration can be seen below:

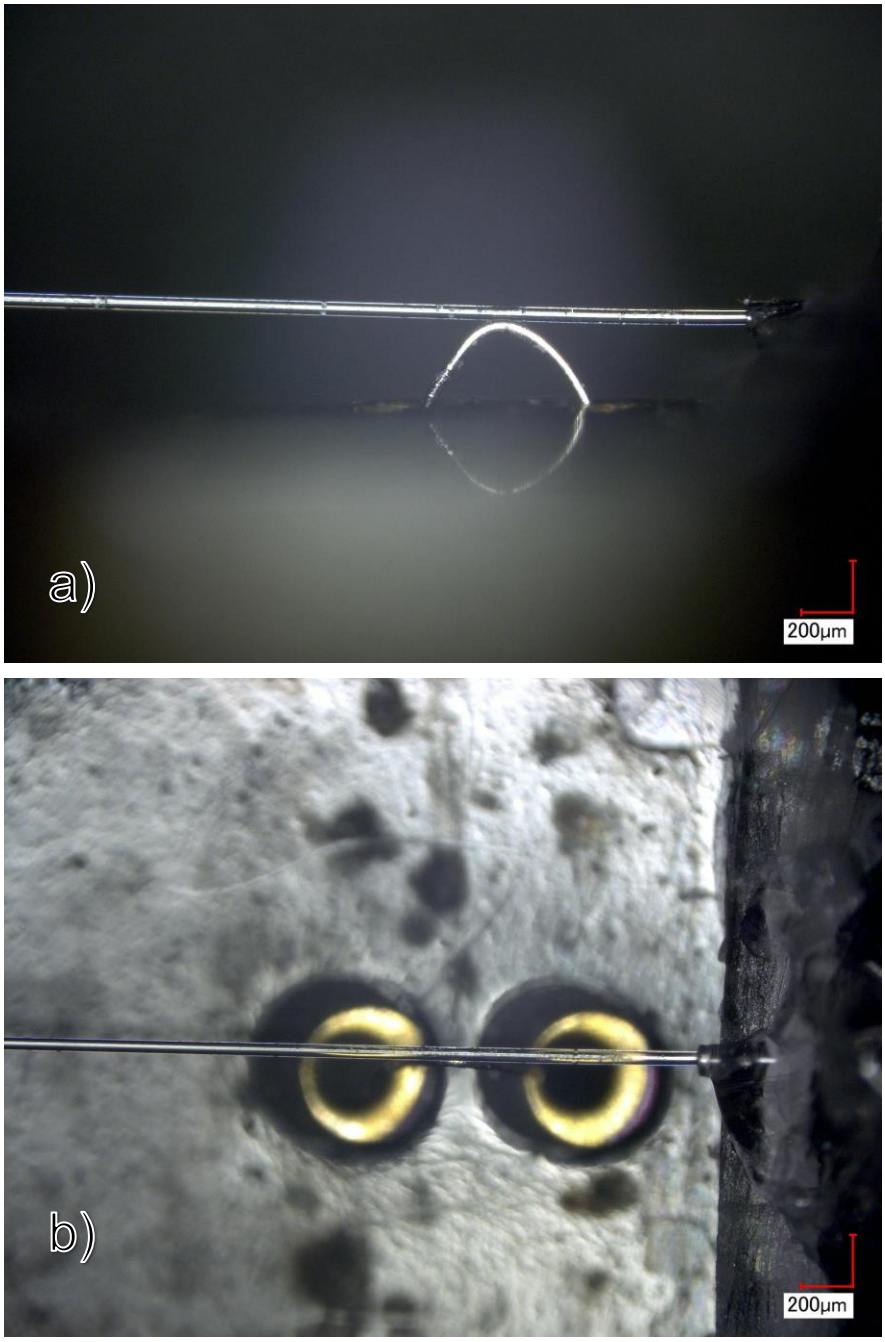

Figure 36. A 50-micron stainless steel, 50-micron fiber sample on a PCB; (a) side view (b) top view

Then, there was attempt made to move to the final scale using 20-micron aluminum 1199 wires and 15-micron fiber a reliable electrical connection could not be made between them. Consequently, a few samples were made using brass at the correct scale because it could easily be soldered to the copper pads and according to

the simulations brass should have been just good enough to reach the desired tip displacement values.

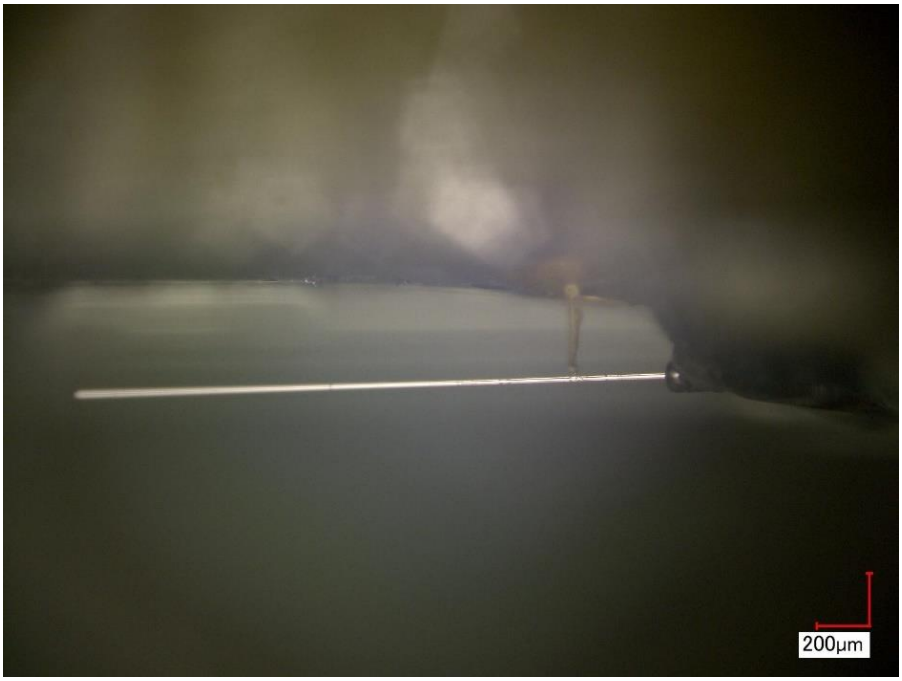

Figure 37. A 20-micron brass sample with a 15-micron optical fiber on a PCB in a perpendicular set up

Note that the wire is no longer parallel to the fiber. This was done to ease the task of making 20-micron samples. The wire being perpendicular to it should make no difference in the performance compared to a sample with parallel alignment as long as the contact point has the same distance.

4.2. Driver Circuit

In order to heat up and cool down the actuating wire, current has to be run through it in a periodic manner. A square wave signal is chosen for this driver circuit. The amount of current through the wire will dictate the power dissipated in the actuator. Power is given by the following formula:

$$P = I^2 \cdot R \quad (30)$$

And since the resistance of the actuating wire is fixed, the current is the only parameter than can be controlled. The frequency of the signal is dictated by the natural frequency of the optical cantilever and the natural frequency of the fiber is a function the

physical shape and size of the fiber. Therefore, there is little leeway in the signal frequency as well. It can only be slightly changed by how close the actuating wire is to the base of the micro-cantilever. Given these restrictions and requirements, the following circuit was designed:

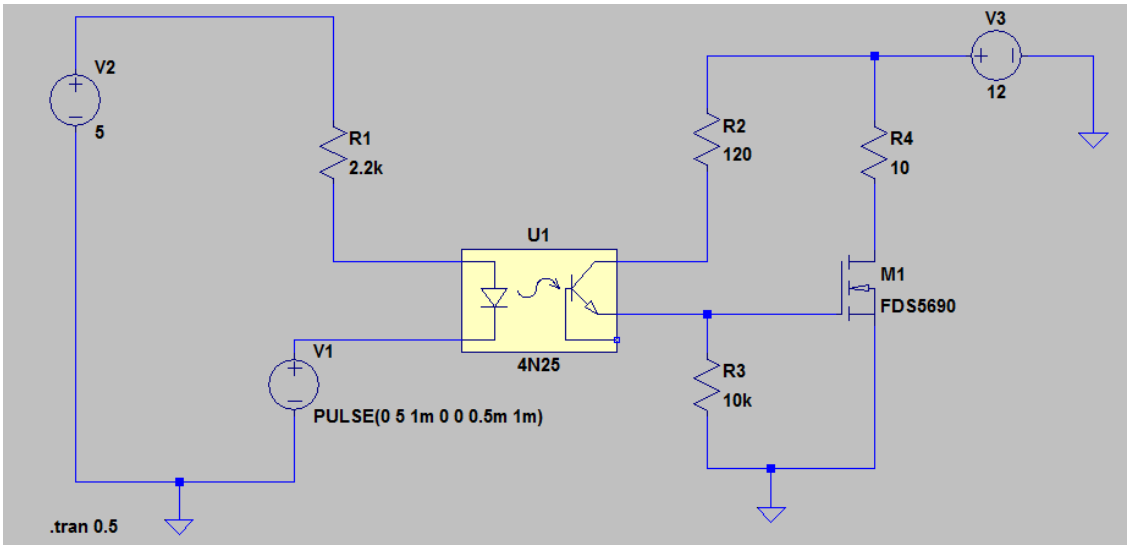

Figure 38. Schematic of the first driver circuit

Since a lot of current has to be passed through the actuating wire, decision was made to use an opto-isolator (U1 in Fig. 38) to isolate the low voltage electronics, such as the microcontroller generating the square wave (V1 in Fig. 38) from the high power sections of the circuit. Voltage source (V3 in Fig. 38), is the source for the high-powered side of the circuit. The low voltage signal generated by the microcontroller will only dictate the frequency of the signal out of the opto-isolator but the voltage is function of the R2 resistor. For this phase of the experimentations, an Arduino Uno board was used for signal generation [39]. The low quality 16MHz crystal oscillator of the microcontroller board was not a cause for concern at this stage because of the relatively low frequency of the large scale samples (though, the generated frequency not being very steady and drifting from the target can decrease performance somewhat); Though the oscillations and changes in performance could have also been caused the shifting resonant frequency of the fiber. The output of the opto-isolator is then used to activate the high powered N MOSFET (M1 in Fig. 38). The actuating wire is placed in series between the MOSFET and the pull up resistor, R4. The pull-up resistor is needed because of the actuator wires' very low resistance. The pull-down resistor, R3, is needed because the opto-isolator is a leaky source and without it, the current leakage might fill the P channel

of the MOSFET and cause accidental activations. A LTspice [40] simulation of the signals at various points is shown below:

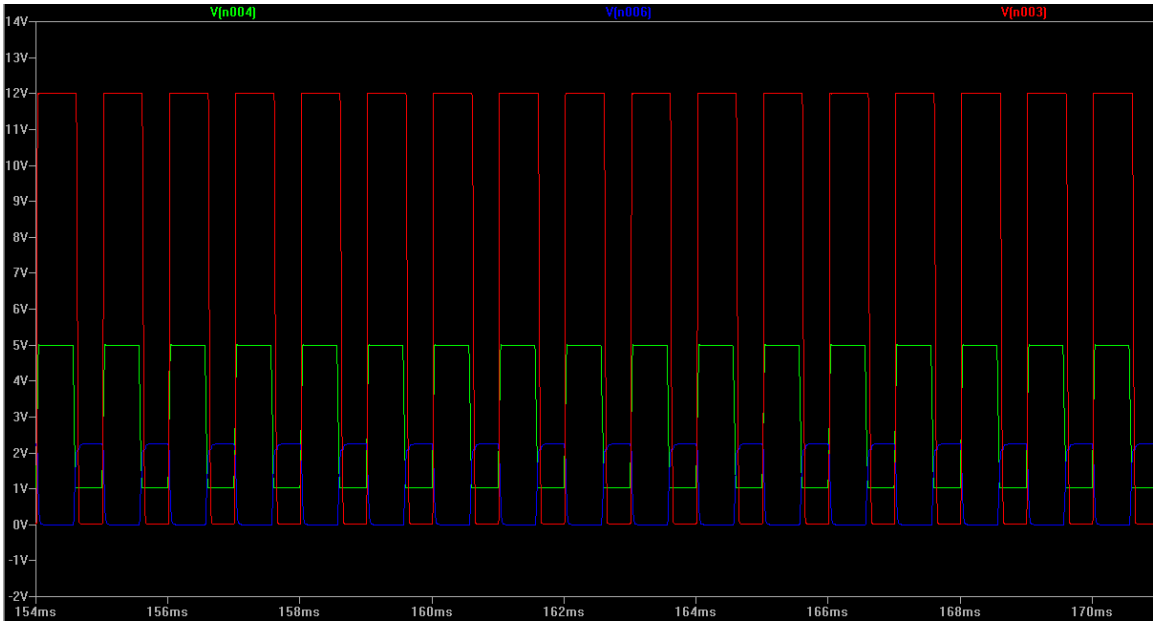

Figure 39. LTSpice simulation of the first driver circuit; The red signal is through the actuator, the green signal is the output of the opto-isolator, the blue signal is the output of the microcontroller (notice it is inverted)

4.3. Experimental Results

In order to test the performance of the samples, a frequency sweep near the expected natural frequency was done to find the actual natural frequency. Then, the input power was increased till the lateral vibrations plateaued. All of this was done with a microscope focused on the tip of the fiber to observe and record its movements.

Results of all the major experiments has been tabulated in chronological order. Multiple samples with similar set-ups and performance have been grouped together and their results have been averaged out. The nichrome and stainless steel samples had a resistance of a few ohms while the brass and aluminum samples had a resistance of about 0.2 ohms on average.

Table 1. Experimental results from the first wave of prototypes

Sample #	Wire Material	Wire Thickness (microns)	Fiber Thickness (microns)	Fiber Length † (mm)	Expected Natural Frequency (kHz)	Actual Natural Frequency (kHz)	Displacement (microns)
1	Nichrome*	127	125	11	0.590	0.559	36.8
2	Nichrome*	127	50	7.5	0.780	0.864	20.2
3	Stainless Steel 302	50.8	50	12	0.280	0.252	563
4	Stainless Steel 302*	50.8	15	<1	12	~11+	25
5	Brass 7030*	20	15	<1.5	5.4	~5.6	45
6	Brass 7030*	20	15	~2.2	2.5	~2.7	79
7	Brass 7030*	20	15	~1.5	5.4	~5.7	53
8	Aluminum 1199*	20	15	<1.8	4.1	~4.2	70
9	Aluminum 6061*	25	15	~2	3	~3.1	45

† - Length after contact with the actuation point
* - Represents data from multiple samples and tests

The calculated natural frequency for sample #1 is 590 Hz, experimental natural frequency is found to be about 560 Hz. The harmonic response depicted in Fig. 40 shows the jump in the tip displacement and the mid-span stress values for this micro-cantilever calculated analytically assuming $\overline{\Delta T} = 1°C$.

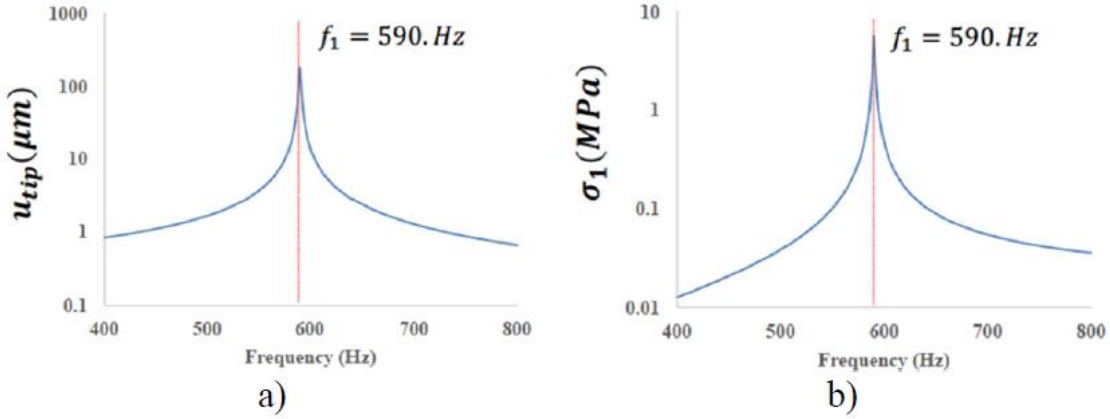

Figure 40. The predicted harmonic response of the tested micro-cantilever sample #1; (a) displacement magnitude (b) stress at mid-span

The displacement of sample #3 can be seen below:

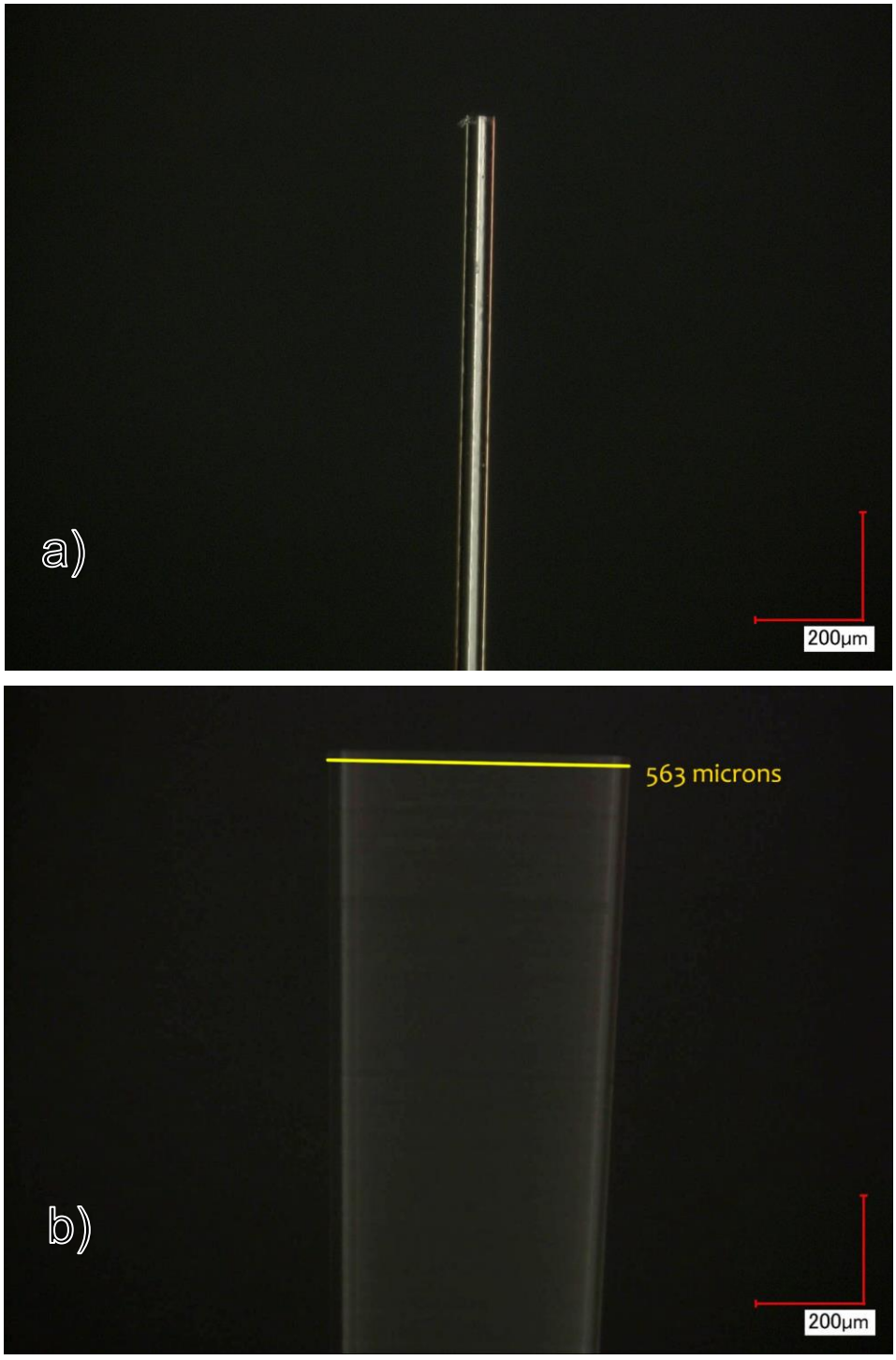

Figure 41. Test results from sample #3; (a) no excitation (b) excited to resonance

Considering the small variations from the idealistic model to the manufactured micro-cantilever, we can conclude that the analytical model can generally predict the response of the system. The larger deviations between predicted and recorded

displacement amplitude is due to simplifications described in section 3.1.1. The actual magnitude of displacement is considerably lower than what is expected but the calculations assumed uniform temperature change in the actuating wire, when in reality that is not the case. Furthermore, in this configuration, the actuators were connected to the conducting copper wires which are supposed to act as heat sinks via blobs of solder in the via holes. Solder is largely made of tin (and sometimes lead) which has a lower thermal conductivity value than aluminum or copper which means it can hold on to heat during ‘off’ states and dampen the temperature difference, thus lowering the performance.

The sample with the 50-micron stainless steel wire and a long 50-micron fiber gave us the best experimental result but it is important to note that the extreme length of the cantilever in this case lowered the natural frequency to 250 Hz. This highlights the importance of thermal conductivity and how much a factor thermal throttling places in a design like this. Various samples were made using aluminum 1199 and 6061 using numerous methods. Nevertheless, the electrical and thermal connection between copper and aluminum remains poor resulting in very subpar performance. The poor performance can also be attributed to the rather large actuators in these samples and inadequate cooling of the PCB copper traces.

4.4. Summary

A laboratory model of the proposed optical fiber and actuator system was created in the lab. Using a frequency generator to sweep over a large frequency range, showed occurrence of resonance at a particular frequency, which is close to the predicted frequency obtained from the analytical model. However, harmonic response cannot be easily predicted here due to the fact that the real distribution of temperature inside the actuator wire is not known in this model and a simple assumption is replaced it to study the response. Some of this work is published in a paper by Komeili, Ahrabi and Menon [28].

Nevertheless, even with the aforementioned shortcomings, it was observed that this method is capable of inducing resonance in micro-cantilever and results generally follow the expected response and behavior and for the most part the empirical results matched the analytical models to a somewhat reasonable degree or followed the same

trends. This stage identified some problem areas but also showed the potential of this proposal to meet the requirements for this project and demonstrated that it is certainly possible to induce lateral vibratory motion in an optical fiber by and expanding and contracting metal wire thus meeting objective 1.

Chapter 5. Design and Development of the Ultra Thin Endoscope Enclosure

5.1. Design Overview, Objectives and Requirements

The concepts explored, and results presented in chapter 4 were adequate to reach the conclusion that the proposed thermal actuation method could be used to excite the optical fiber micro-cantilever to resonance in a small form factor and therefore, reduce the overall size of the system to levels that would allow a medical endoscope to be used inside of lung airways.

While the calculations and analytical modelling show that the underlying concept is sound, they do not include or explain how such a system would be fabricated and how it should be arranged. The mathematical models only examined the interactions of the actuator wire and the cantilever beam in relation to each other, isolated from all other external factors and conditions. This chapter is aimed at providing detailed information on the efforts that were taken towards designing a system that would satisfy the project requirements in an ultra-thin package.

In order to assess the success and performance of the system, a number of requirements were set for the project. The sub 500-micron outer diameter size limitation is the defining factor and the single most important characteristic of this proposed endoscope enclosure and many design decisions arise from it. The second benchmark is the amount of lateral displacement achieved by the tip of the optical fiber cantilever during resonance. The higher the displacement, the higher the image resolution. 200 microns is set as the minimum requirement for displacement. The frequency of the vibrations is also important. It is ideally set at 6 to 8 kHz, but it can go as low as 2 kHz. Other considerations for this project, though not as important, are the manufacturing time and cost. Keeping the cost down would open the door to a disposable and one time use endoscope head. The proposed thermal actuation method fits the size limitations and works on the basis of thermal expansion due to the heat generated by the internal resistance of a small wire when current is passed through it. Despite being novel, compact and relatively simple, it has some inherent flaws such being very inefficient and generating a lot of heat while relying on efficient heat dissipation by the conducting wires

before the next time cycle. This makes heat transfer the single most important design decision.

At the core of this design lies a single mode dual channel optical fiber custom made by BC Cancer Agency (BCCA). In order to fabricate this fiber, a standard optical fiber is heated up and pulled to form a neck. When the neck narrows down to the desired width, it is cut off and spliced to the center core of a 127-micron dual channel fiber. One such fiber can be seen below:

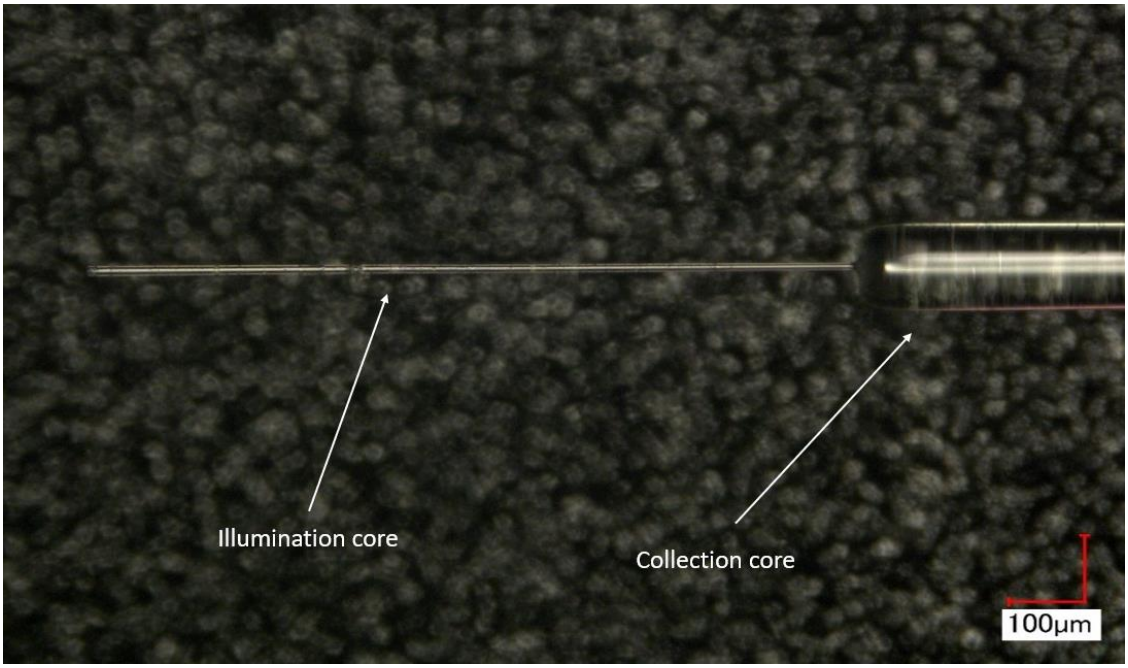

Figure 42. A dual channel single mode optical fiber

The internal core transmits the blue laser light (442 nm), while the outer core collects the reflected light. The thin portion of the fiber, referred to as the micro-cantilever has a diameter of 11-15 microns, while the thick section of the fiber has a diameter of 125-127 microns. A 3-micron core is used for the transmission of the blue laser light.

Due to the dimensions of the fiber, it cannot transmit and subsequently collect enough light to form a picture in a stationary state. What it captures, can be thought of as a single pixel. For this reason, the smaller portion of the fiber that transmits light has to be oscillated significantly. This essentially allows the set up to illuminate a line in front of it and consequently capture a line. If the entire set up is rotated, then it starts collecting light in a propeller raster shape as explained in section 2.2. The data collected

can be reconstructed into a circular image. The system is set to be rotated at 25 RPM. Because of the propeller pattern, the fiber is going to capture more light form the center than the outer edges (Fig. 7). In order to compensate for the lower number of data points from the outer edges, higher frequencies are desired. This limitation dictates the desired sampling rate, i.e. the vibrational frequency of the fiber.

The fiber itself is excited from the base by a fine wire that is expanding and shrinking due to a periodic current passing through it. The fine wire has to be more resistive than the conducting wires so that it heats up more than them but at the same time has to be very thermally conductive to cool down in time during the off portion of the cycle at such high frequencies. The periodic signal through the fine wire matches the natural frequency of the vibrating fiber. The fine wire is cooled down by the larger conducting wires which act as heat sinks. Thermal conduction is the only effective mean of heat transfer at this scale and frequency; effects of convection and radiation are negligible.

The original design that was proposed in the grant documents for project can be seen below:

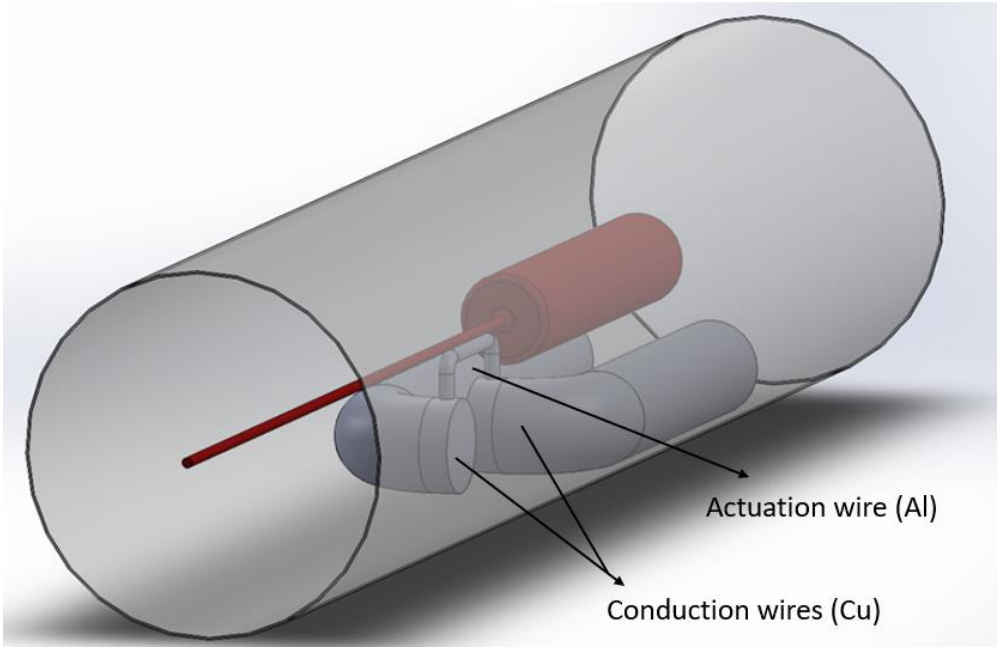

Figure 43. The original design proposal

The original design proposal, despite being simple and capturing the essence, was not realistic from a manufacturing point of view. First off, 500 microns is the outer diameter

and even the smallest tubes will have at least 30 to 50-micron thick walls, reducing the internal diameter size to just about 400 microns or less which leaves no room for alignment, placement and assembly work. Therefore, the structure has to be made and assembled outside and then just be inserted into the tube. Or at least be secured to a solid platform. Furthermore, the proposed metals, copper for conducting wires and aluminum for the smaller actuating wire, are dissimilar metals and cannot be easily joined together in the fashion shown. Handling and bending of the fine 20-micron diameter wires into the desired rectangular shape is also a very difficult task.

Nevertheless, the large scale early prototypes fabricated to prove the concept in chapter 4 were made to emulate this design. The PCBs with thick 2 oz thick coper traces (about 70 microns thick) and narrow and closely placed via holes were meant to act as a self-contained replacement for the loose copper wires. This would solve the issue of alignment and placement of the copper wires as well as being a secure platform for the actuating wire and optical fiber.

However, it was evident that the design was not going to work at the desired scale for various reasons. A PCB based design would still rely on handling, bending and placement of the 20-micron diameter actuation wire on the PCB by hand which leads to a greater variety and lower consistency in the produced samples. In addition, it reduces yield and increases production time for each single sample. On a via hole PCB, the actuation wire has to be routed through the via holes first (very difficult task) and then via hole has to be filled with solder and from the experiments it was evident that the existence of the solder at the interface between the heating element (actuation wire) and the heat sink (conducting wires) hampers the performance in terms of lateral displacement (as seen in Fig. 38). This is expanded upon in the following subsection on material selection (section 5.2.).

The use of wire bonders for a pad-based PCB was explored as well. For this, the wire bonder at the 4D Labs was used. The wire bonder was capable of making ball bond to wedge bond connections using both gold and aluminum and several samples were produced but the machine was designed to be used for making electrical connections between electrical chips. Therefore, the resulting bonds were never meant to bear any load and broke under the smallest of loads; or the over stretched wire buckled under load. One of these test bonds can be seen below:

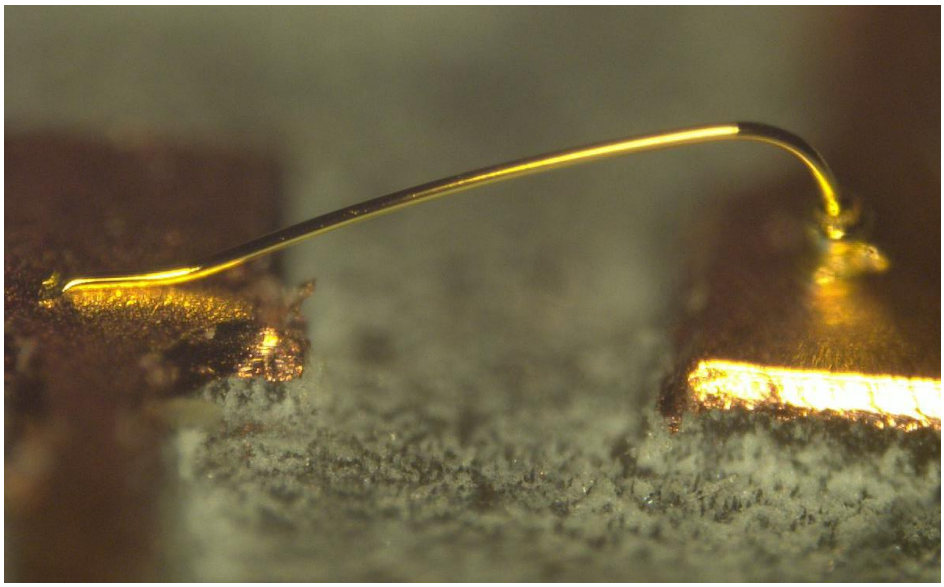

Figure 44. A gold wire bond between two Protomat machined copper pads

Another major issue was the manufacturing of a PCB that is actually small enough to be placed on the side wall of a 400-micron cavity. A few high-end fabrication houses were identified and contacted that advertised being able to make 2 oz, 1.25 mil copper traces and spacing (about 32 microns) on 100-micron thick boards; which would meet our requirements. However, aside from their high cost and long lead time, such PCBs were never ordered because of neither the manufacturer or us being sure how to cut or handle them or how structurally sound they would be even if they survived the cutting process. A 100-micron thick, 250-micron wide and a few millimeters long PCB would essentially be a glass-reinforced epoxy laminate needle.

Ultimately, the PCB design was abandoned because of the reasons mentioned above and a few others and after more than a dozen design changes and iterations the device morphed into what is depicted below:

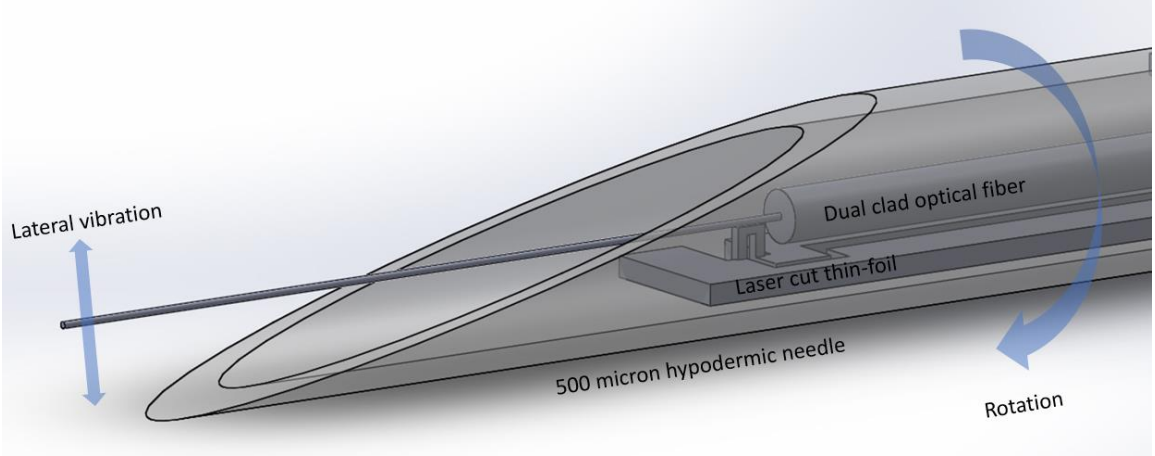

Figure 45. The final design iteration for the ultra-thin endoscope tip design

This chapter explains the thought process and reasoning that has gone into the design, development and fabrication of the proposed novel thermally actuated single fiber scanning endoscope tip enclosure and presents multiple configurations that meet the strict ultra-thin size requirements; in accordance to thesis objective 2.

5.2. Material Selection

The two metals considered for this project by Komeili et al. [8] [9] [10] [11] [12] were aluminum for the actuating wire and copper for the conducting wires. In those papers, the only consideration given to these two metals' properties were their excellent thermal conductivity and the fact that aluminum is about 40% more resistive than copper thus requiring less current through it to heat up compared to copper. However, these studies failed to consider the manufacturing point of views. Naturally occurring aluminum oxide, Al_2O_3, is a very hard crystalline with melting temperature of 2072 $°C$. This makes aluminum impossible to solder and extremely difficult to braze or weld. To exasperate the problem further, most of the methods used at macro scale simply do not work at the 20-micron scale; whether it is the welding methods, or physical surface prep or chemical cleaning procedures. At macro scale, copper and aluminum are used in conjunction with each other for cooling applications but they are either press fitted together, or aluminum is plated with a tertiary metal and then soldered to copper. Furthermore, galvanic corrosion is a real concern with aluminum and copper any time they come in contact because they are dissimilar metals. Galvanic corrosion is an electrochemical process in which one metal corrodes preferentially when it is in electrical contact with another. It happens because dissimilar metals and alloys have different electrode potentials and

one metal acts as anode and the other as cathode when in contact in an electrolyte. In the case of aluminum and copper, when there is metal to metal contact, copper will eat into aluminum and corrode it. The higher the humidity or potential difference, the higher the corrosion rate. Although It is possible to form copper to aluminum joints via cold fusion or specialized spot welders, the joints will be inherently brittle and weak which is not ideal for a load bearing vibratory application. In addition, while it is possible to slow down or stop the galvanic corrosion process by using a sacrificial layer like tin or nickel, it is not suitable for a high frequency thermal application because of differing heat conduction properties [41] [42]. Subsection 5.6. covers various joining methods used or explored in this project in more detail. Nevertheless, despite the inherent problems presented above, and being extremely difficult to work with, many aluminum samples were produced and tested because aluminum's unique set of material properties.

These reasons were compelling enough to call for a new material selection process; one that looks at other materials that might fit the project requirements and are either better than pure copper and aluminum in terms of performance or are easier to handle and work with. For this systematic material selection, software package 'Granta: CES Selector' [43] was used. Granta: CES Selector is an engineering software selection program that makes use of the Cambridge Engineering Selector (CES)'s data base of complete property data for over 3,500 material types (some 80,000 materials) across the full range of engineering materials and lets the user take into account four aspects during the selection process: feature, material, geometry and processes. These indices and comprehensive approach make it possible to rationally choose the most suitable materials for the specific application. The main criteria considered for the actuation wire in this project were:

- Coefficient of linear thermal expansion
- Thermal conductivity
- Young's modulus
- Electrical resistivity

The coefficient of linear thermal expansion is the fraction of a material that expands per degree temperature, i.e. it is the linear thermal strain per degree C. This important factor dictates how much heat needs to be generated by resistive heating in the fine wire in order to achieve the desired level of actuation. Thermal conductivity is the rate at which

heat is conducted through a solid at steady-state. It is measured by recording the heat flux flowing from surface at the temperature T_1 to one at T_2 in the material separated by a set distance. This factor determines how fast the fine actuating wire cools down after the power is cut off. If this number is not sufficiently high, the actuating wire will not cool down to the starting temperature before the start of the next cycle, thus reducing the temperature difference between the on and off states and consequently affecting the lateral vibrations of the fiber in a negative manner. Young's modulus is defined as stress over strain. It is the slope of the initial linear-elastic part of the stress-strain curve. It describes the elastic properties of a solid undergoing tension or compression in one direction and as such measures the ability of a material to withstand changes in length when under lengthwise tension or compression. In this project, it is used to determine how well the actuation wire is able to withstand the vibrations of the fiber without bending, buckling or deforming. Electrical resistivity is the resistance of a unit cube with unit potential difference between a pair of faces. Electrical conductivity is simply the reciprocal of the resistivity. In this context, a high electrical resistivity in the actuation wire is desired because it means a lower current value is required to heat the wire to the desired temperatures. For the conduction wires, lower resistivity and high thermal conductivity are the desired selection parameters [41].

Initially, the assumption was that he most suitable material would have the highest coefficient of linear expansion and as such it was prioritized more than any of the other factors. Therefore, first the materials that did not meet the minimum specified Young's modulus were filtered out. The remaining materials were graphed as thermal expansion over thermal conductivity and finally filtered for electrical resistivity as seen in the following graphs:

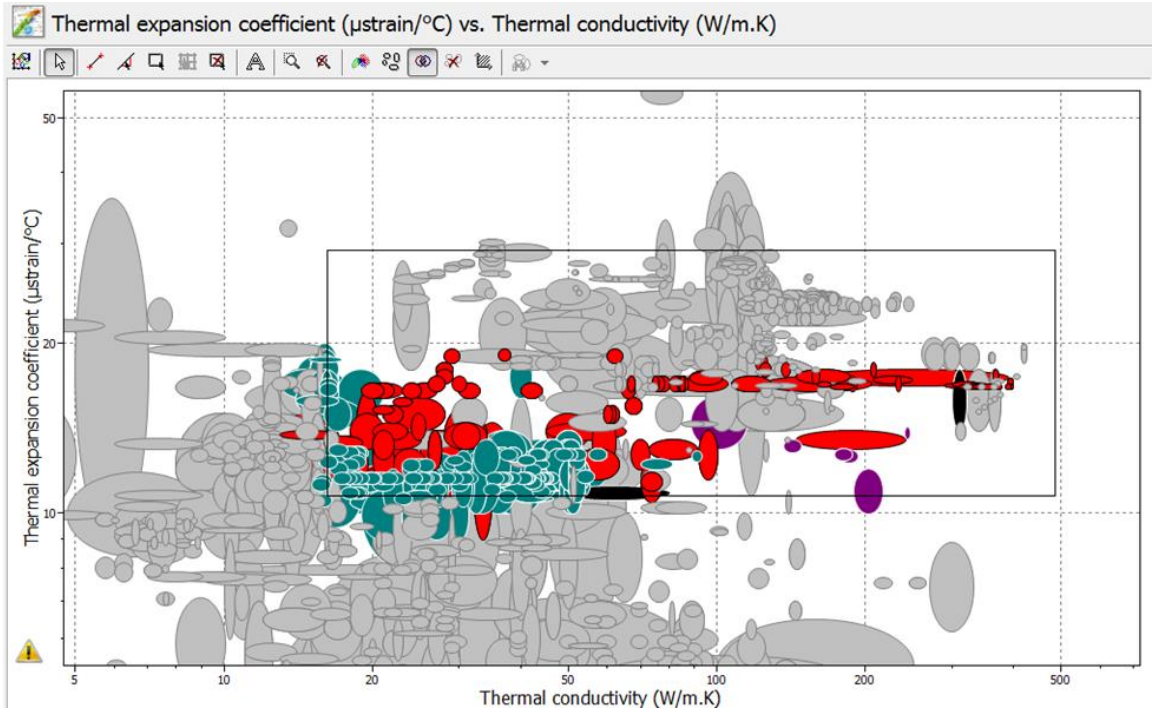

Figure 46. Material comparison based on thermal expansion vs thermal conductivity

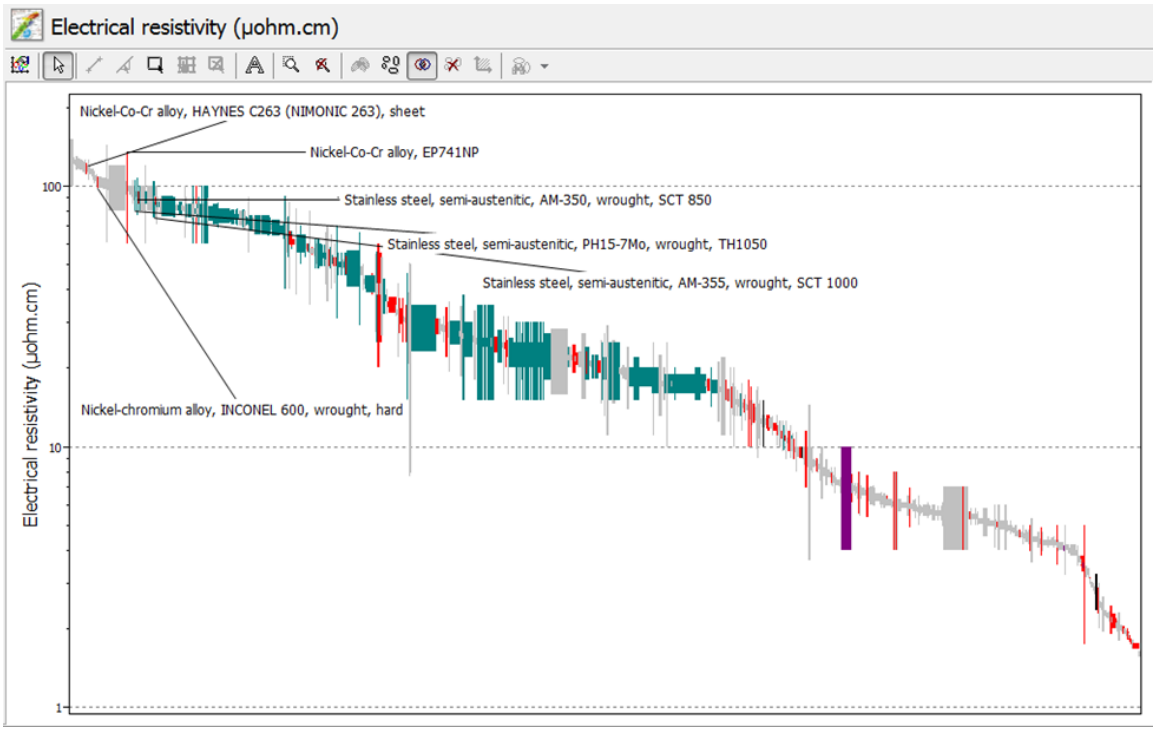

Figure 47. The remaining metals being sorted based on electrical resistivity

This selection process resulted in zinc-copper alloys coming on top followed by nickel-silver, aluminum-bronze, gold-platinum, palladium-silver, and aluminum 2 and 8

series alloys, respectively. However, many of these alloys are very rare and exotic and are only made to order for niche applications and a big portion of them do not come in wire form.

After the first batch of samples and their subpar results (section 4.3), and a second look at the range of these parameters amongst various metals, it was observed that the coefficient of linear expansion does not change all that much in metals. Instead, electrical resistivity and thermal conductivity are the parameters that can wildly vary. Therefore, the selection process was revised to prioritize thermal conductivity first and foremost followed by electrical resistivity and finally coefficient of linear expansion. Note that, generally speaking, electrical resistivity and thermal conductivity are inversely proportional to each other. Meaning, a material that has good thermal conductivity, tends to be electrically very conductive as well. The resulting selection graphs with the revised priority list can be seen in the following figures:

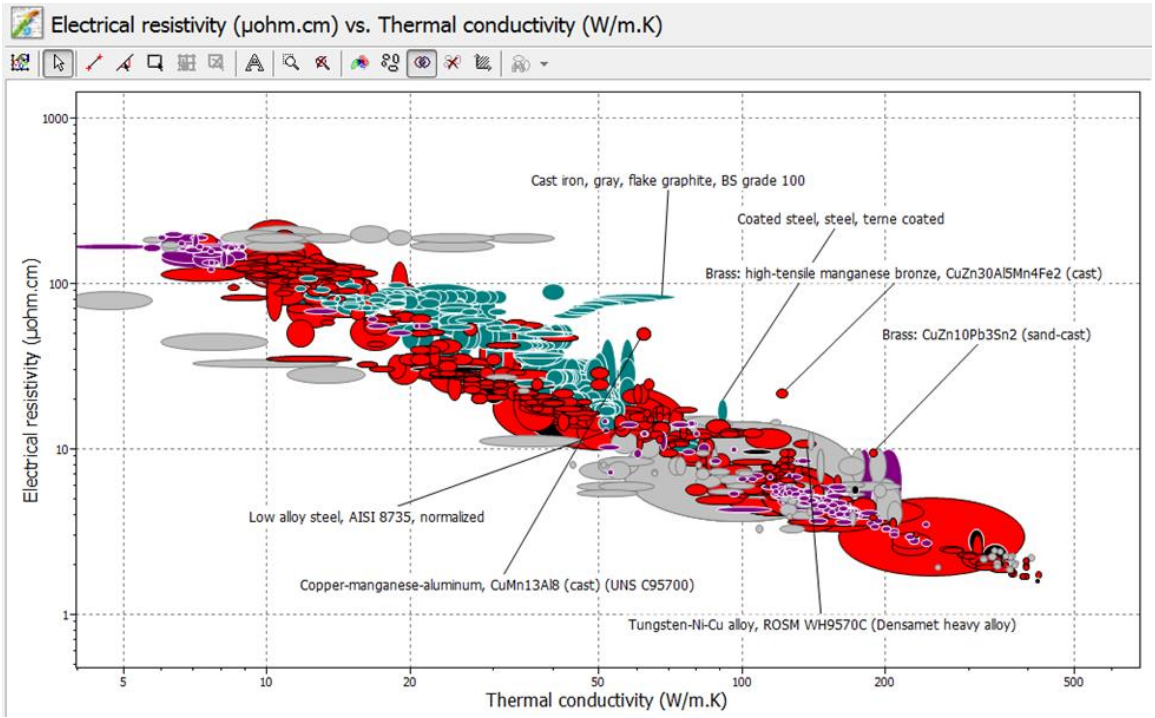

Figure 48. Electrical resistivity vs thermal conductivity

As mentioned above, Fig. 48 shows that metals that have excellent thermal conductivity generally have very low electrical resistivity values. This is problem because if the actuation and conduction wires have the same resistance, for the same given current, the actuation wire would have a marginally higher temperature and therefore a

lower temperature differential. For this reason, the group of metals in the middle right of the graph were chosen because they offered a nice compromise of moderate electrical resistance and acceptable levels of thermal conduction.

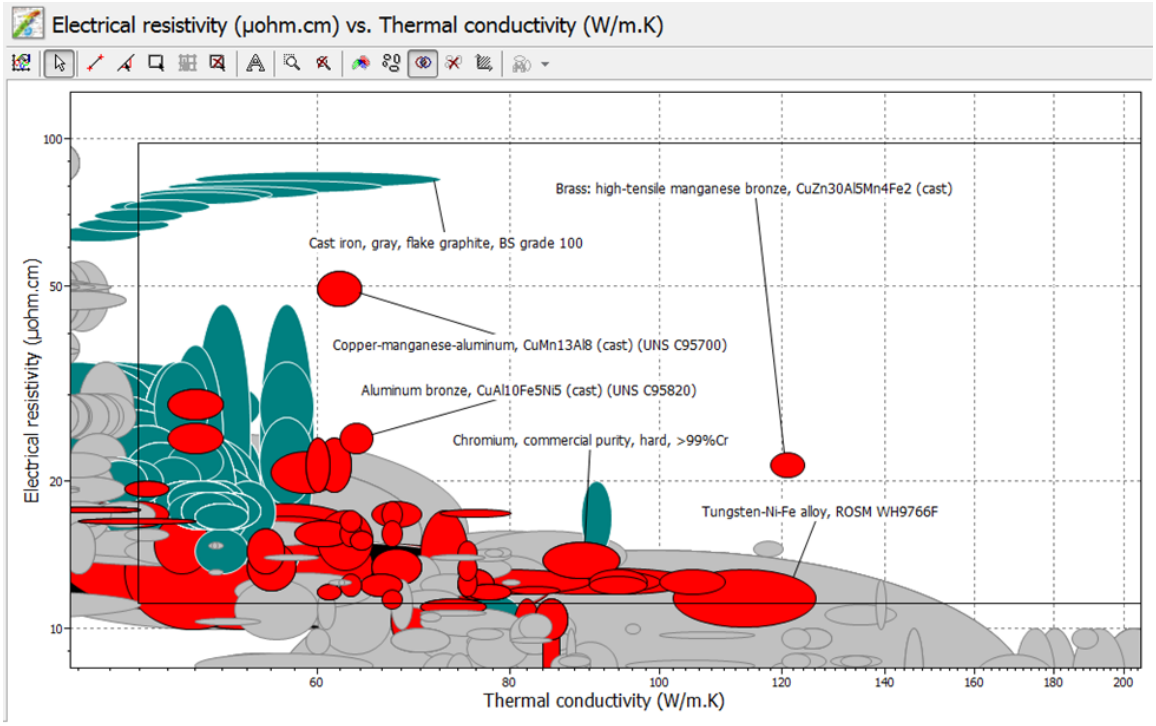

Figure 49. Metals with moderate levels of electrical resistivity and thermal conductivity

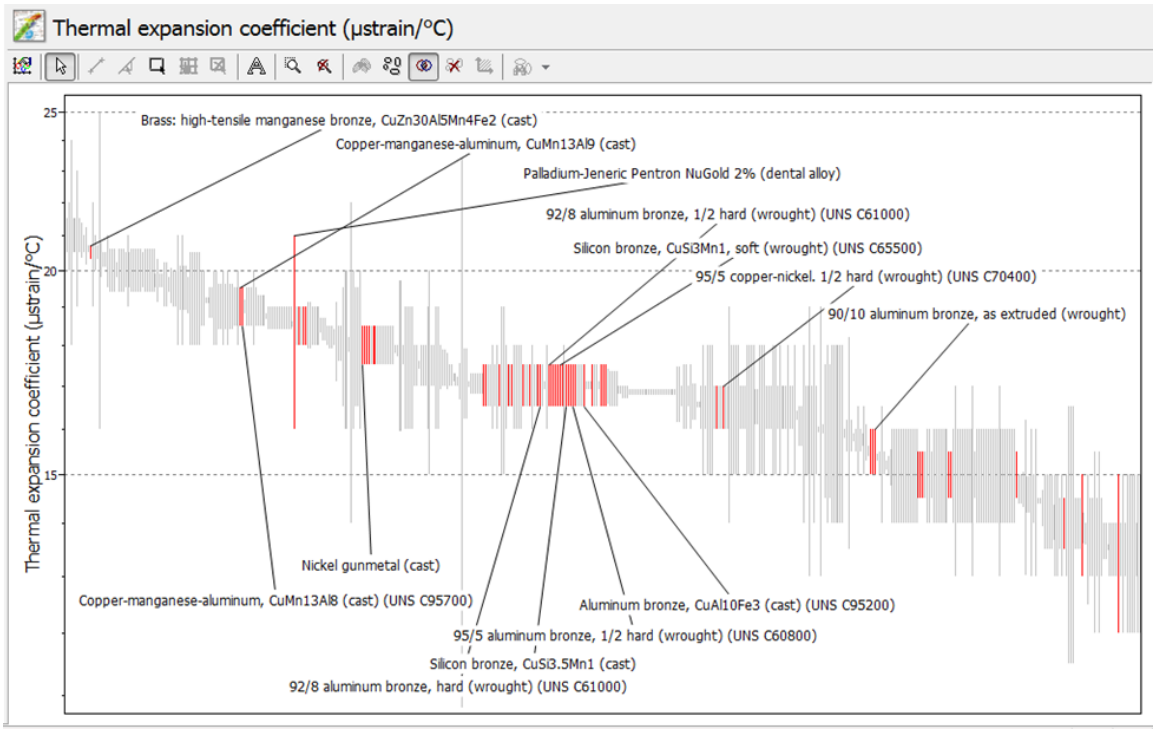

Figure 50. Remaining metals being sorted for thermal expansion coefficient

This new selection process identified manganese-bronze followed by common copper alloys such as brass and aluminum-silicon-copper alloys (aluminum 6 series alloys) as suitable materials for the actuation wire. Despite not being able to get manganese bronze as a wire in the desired dimensions, aluminum 6 series (6061 specifically) and brass alloys are readily available in wire form or thin-foil. Relative to pure aluminum, aluminum 6xxx series are easier to machine, and are weldable and can be precipitation hardened (though not to the levels of 2xxx and 7xxx Al alloys) and for these reasons are one of the most commonly used general-purpose aluminum alloys. Aluminum 6061 has a slightly lower thermal conductivity, but it is not so low that it would start to affect its performance at our frequencies. However, it is significantly more resistive than pure aluminum and it has a higher thermal expansion coefficient. Even though yellow brass (brass 7030) is marginally worse than aluminum 6061, in terms of its material properties, it is a high alloy of copper which means it can easily be joined to the conducting copper wires via multitude of methods, giving it a significant edge in ease of use.

Table 2. The properties of various metals used in the prototypes

	Nichrome[2]	Stainless steel 302[2]	Nickel[3]	Aluminum 1199 (pure)	Aluminum 6061	Brass 7030	High tensile manganese brass
Linear thermal expansion (μstrain/°C)	13	20	13	22.4	24.6	19	21
Thermal conductivity (W/m.K)	15	24	96	220	170	126	121
Young's modulus (GPa)	210	197	170	75	71	110	91
Electrical resistivity (μΩ.cm)	114	70	7	2.5	4.4	6.5	23

Nickel is the most commonly used metal as an intermediary layer in between copper and aluminum joints. For the conduction wires, silver edges out copper with ever so slightly higher thermal conductivity (420 W/m.K as opposed to 400) and 6% lower electrical resistivity but those marginal improvements are not worth the significant price increase. At some point material selection becomes an optimization problem where it has to be decided how much small improvements are worth in the grand scheme of things. For example, a copper 24% silver alloy is a better candidate for the conduction wires solely from a material characteristics point of view because it has a much higher maximum service temperature as well as slightly better thermal conductivity and comparable electrical resistivity, but it is rare and therefore more expensive than both.

In section 4.3. it was mentioned that the large-scale models did not perform as well as they were expected to and a big portion of it was attributed to using solder at the base of the actuating wire; where it is connected to the conducting copper traces. This is due to Tin's (and Lead's) material properties which most solder wires consist of. Tin has a very low electrical resistance value so when current passes through it to the actuating wire, it does not heat up. However, during the 'on' stage, when the actuating wire heats

[2] Only used in early large-scale prototypes outlined in section 4.3.

[3] Most common metal used in between copper and aluminum to facilitate a fine joint

up, the heat is transferred to tin (solder blob) via conduction. Tin has a very high specific heat capacity (compared to most metals) which means that a lot of energy is required to increase its temperature, but it also has a low thermal conductivity value of 67 W/m.K (similarly, tin has a thermal diffusivity of 40, compared to copper at 111, aluminum at 97 mm^2/s) [41]. This means that during the 'off' state instead of the desired fast heat transfer from the hot actuating wire to the copper, tin will slowly give off heat to copper. This raises the temperature floor and decreases the cyclic temperature difference. As a result, this pegs the value of the actuating wire to that of tin because of their relative mass and the fact that the heating wire is connected to the copper heat sinks by the blob of tin. This means that the actuating wire cannot possibly be at a lower temperature than the blob of solder at any point, making solder act exactly the same as a 'smoothing capacitor' which is used in an AC circuit to smooth out the signal and reduce the ripples. For reference, the figure below depicts the effect of a smoothing capacitor in a rectifier circuit [44]:

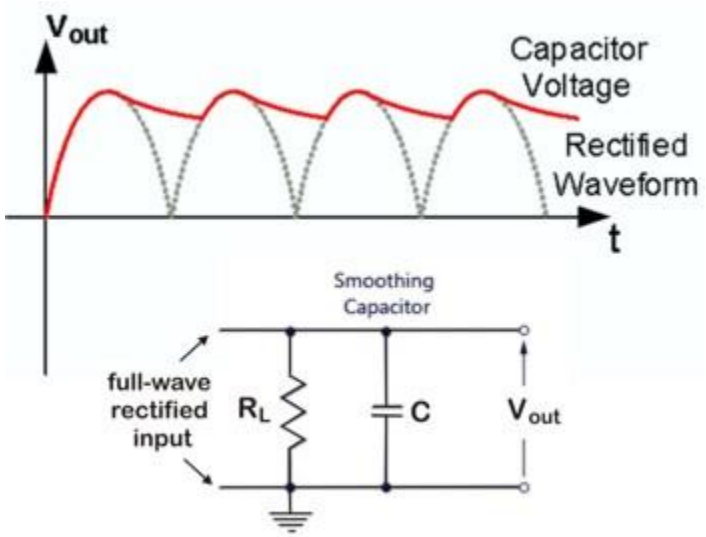

Figure 51. The effect of a smoothing capacitor

In the circuit, the capacitor charges up during the on cycles and discharges slowly during the off cycles reducing any ripples or variance in the output level. In a similar vein, during the on cycles, the actuating wire heats up and warms the blob of solder and during the off state, the warm blob of solder with a larger relative mass starts to slowly give off heat to the copper but because of its low thermal diffusivity it does not go back to the starting temperature thus reducing the variance between the maximum and minimum temperatures and consequently lowering the absolute expansion and

contraction of the actuator which reduces the overall performance of the system. This is an undesirable effect and because of this, solder (or any other material with low thermal conductivity) should not be used at any of the thermal interfaces in the system; unless as an absolute last resort.

5.3. Resonance Frequency

As mentioned previously, the principle behind the actuation method in this design is the resonance phenomenon; i.e. the tendency of a mechanical structure to vibrate at a great amplitude when it is excited at its natural frequency. The first mode shape, the fundamental frequency, yields the greatest amplitude. Therefore, the large lateral displacement of the tip of the optical fiber is only possible at its natural frequency which in turn dictates the frequency at which the actuator has to be vibrating. It also determines the sample rate for image acquisition purposes. A higher frequency means a higher sample rate and a higher sample rate results in more data points and a higher picture quality; especially with the uneven propeller scan pattern where fewer data points are collected from the outer edge. Mechanical resonance of an object, i.e. its natural frequency, is a function of its shape and size. So, in order to achieve the desired frequency for the system, the dimensions of the vibrating optical micro-cantilever have to be changed. The characteristics equation for the system was derived and presented in Eq. (21) in section 3.1.1. Due to the complexity of this non-linearity equation, it is solved using the ‘fsolve’ function (returns the complex roots of a non-linear function) from the scipy library in the Python programming language. This function is used to map the damped natural frequency of the system with varying micro-cantilever lengths and diameters as seen below:

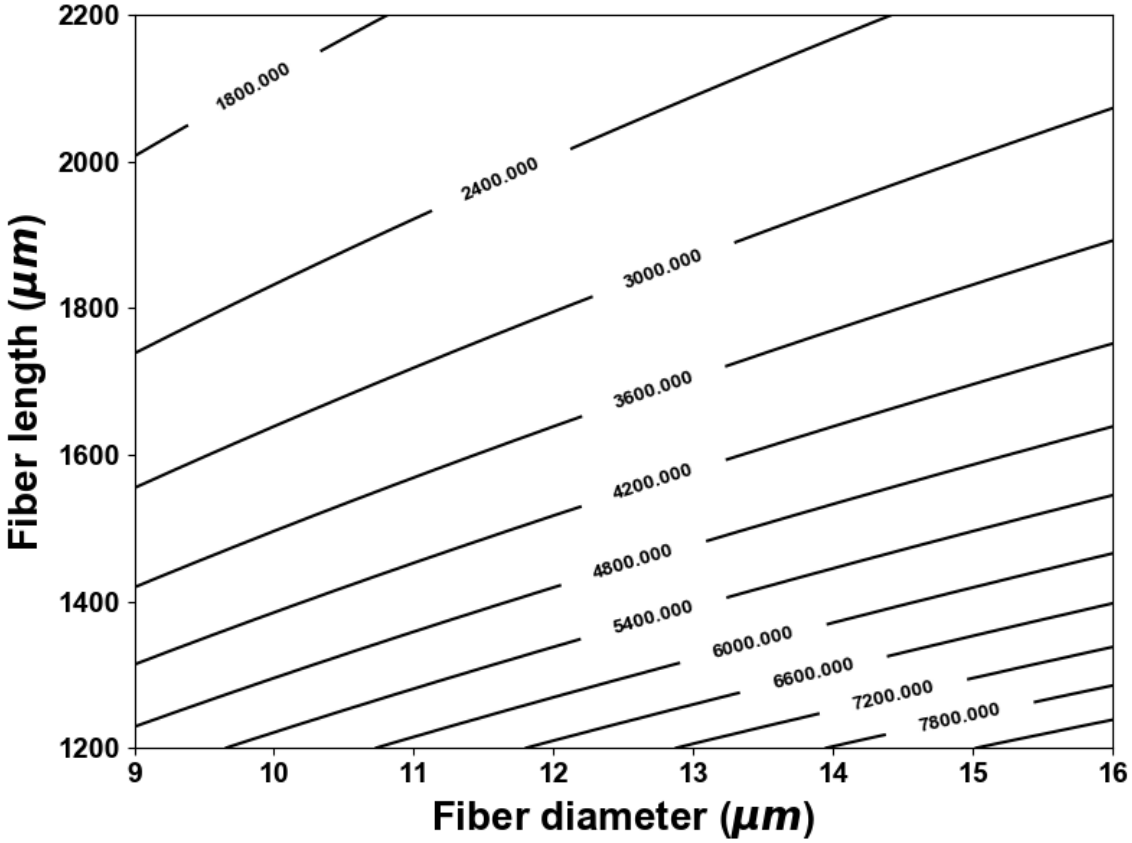

Figure 52. Damped natural frequency of the system (in Hz) as a function of micro-cantilever length and diameter

As expected, the system behaves very similarly to a fixed-free cylindrical cantilever model. The shorter the fiber, the higher the frequency. Similarly, a larger micro-cantilever diameter results in a higher natural frequency. Ideally, the actuator is placed as close to the base of the cantilever as possible. Although, a high degree of oscillations is desired, it comes at a cost. A higher natural frequency value decreases the time between each thermal cycle and at some point, the system is not going to have enough time to cool back down to the starting temperature which can lead to a rising average temperature and lower the magnitude of tip displacement. Furthermore, a larger diameter and shorter length increase the flexural rigidity of the micro-cantilever and decrease the amplitude of the lateral vibratory motion. Therefore, the dimensions of the optical fibers are chosen in a way that the resonance frequency is maximized while the desired level of tip displacement is maintained. Currently, most of the samples made and tested have a resonance frequency of about 2.3 to 3.4 kHz and are about 1.7 to 2.1 mm in length and 11 to 14 microns in diameter.

5.4. Driver Circuit

A square wave at the resonance frequency is given to the actuator as the input to the system. The principle behind the driver circuit (Fig. 38) discussed and presented for the preliminary prototypes in section 3.2. remains the same. A low voltage input controls a power MOSFET which acts as a high frequency switch for the actuator wire. However, the initial design had a few drawbacks that were only evident in higher frequency smaller samples. The initial design used an opto-isolator and a single coil-wound 10W ceramic power resistor as the pull up resistor. At lower frequencies, they performed as expected. However, at higher frequencies, required for the smaller prototypes, both started distorting the signal. The opto-isolator was simply taken out, but the pull-up resistor could not be taken out and had to be replaced. Most power resistors are made by winding a long metal wire around a solid form, often made of ceramic, fiberglass or plastic. One of such resistors can be seen below [45]:

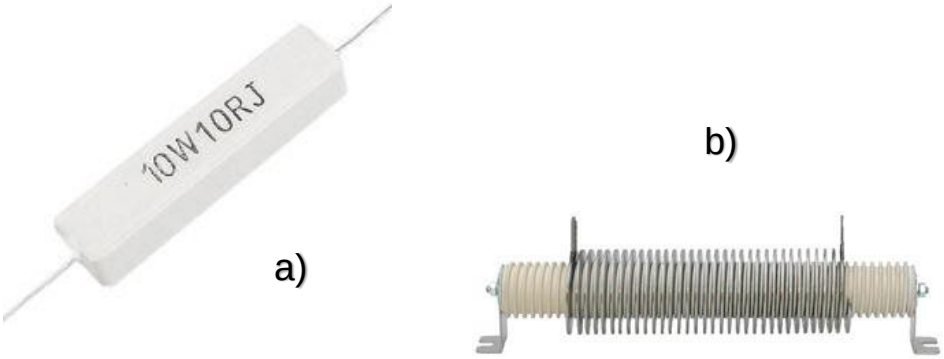

Figure 53. A ceramic 10 W power resistor; (a) package (b) its internals

This coiled wire construction causes these resistors to essentially act as parasitic inductors when a high frequency signal is passed through them; for example, when an 8 kHz square wave is used as an input. This can be modeled as an AC series resistor-inductor circuit. Therefore, at higher frequencies, this causes the current lag applied voltage, creating a phase shift. This response is shown in the following oscilloscope graph:

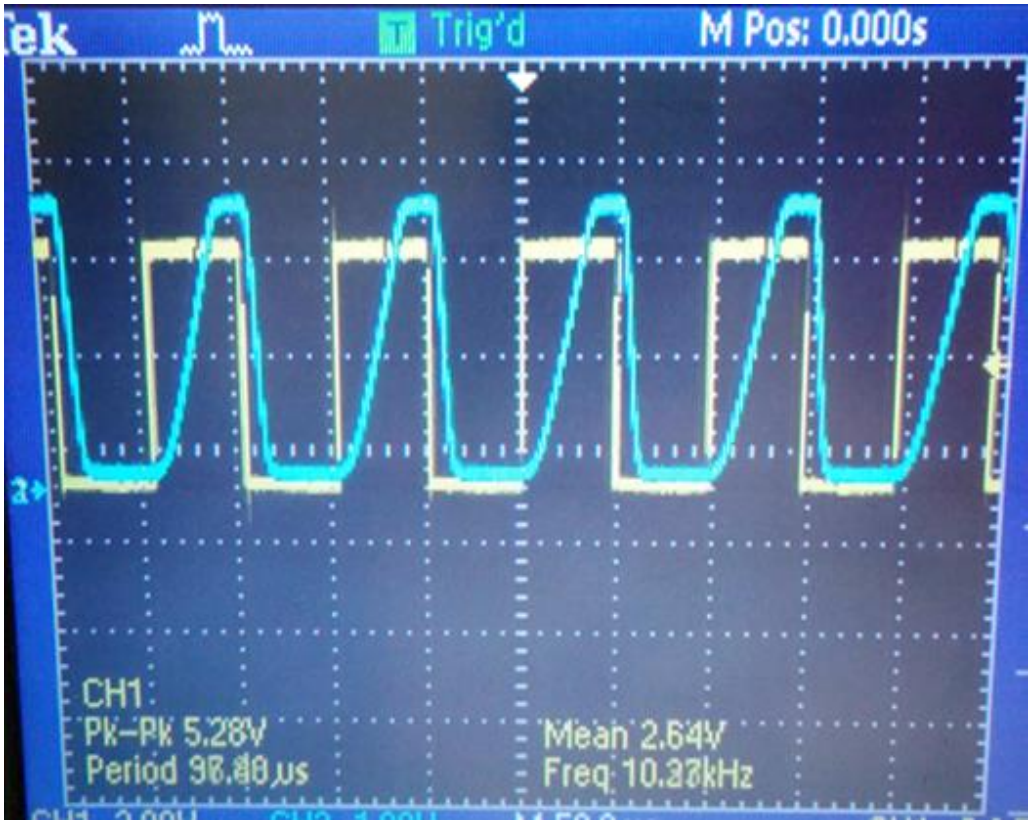

Figure 54. Phase lag induced by the parasitic inductance of the coil wound power resistor at higher frequencies with a square wave input; yellow signal is input and blue is output

As seen, there is so much phase lag caused by the parasitic inductance of the coil wound resistor that the input signal changes to an 'off' state before the output can peak, effectively creating a sawtooth signal. In order to address this issue, metal oxide film resistors were used. Multiple of them were placed in parallel to effectively increase their power rating to the desired levels. The revised schematic for the driver circuit can be seen below:

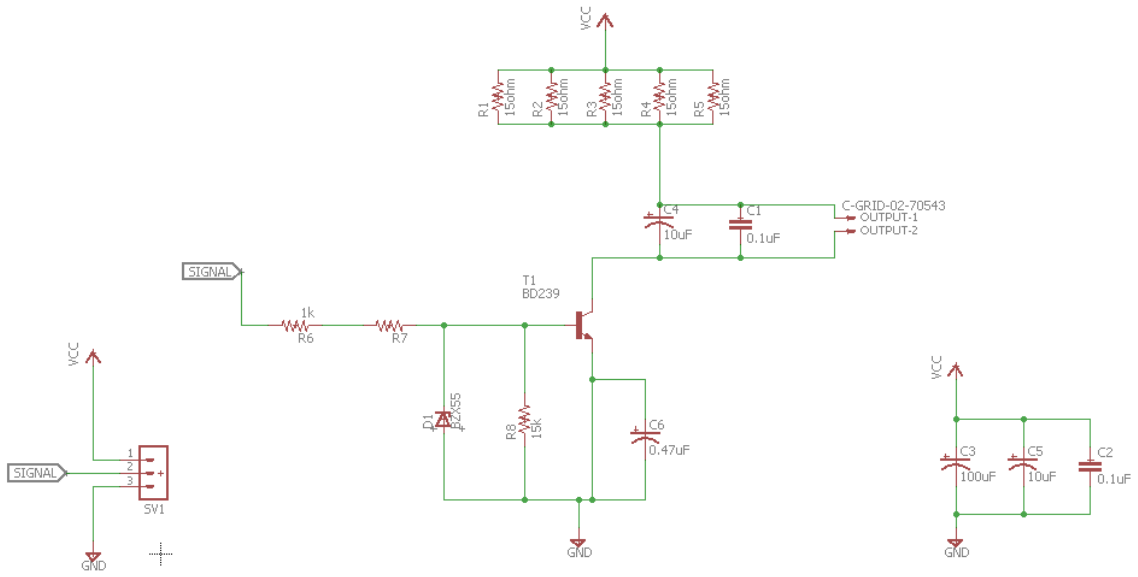

Figure 55. Revised schematic of the driver circuit

Resistors R1-R5 are 5 15-ohm 2 W metal oxide film resistors in parallel effectively creating a single 3-ohm, 10 W pull up resistor. Signal is the input signal generating the desired frequency used to control the gate of the MOSFET device, T1. The pull-down resistor, R8, is needed to make sure leakage current during the ‘off’ cycle cannot accidently fill the P channel of MOSFET and trigger an ‘on’ state. The Zener diode, D1, is used as an overvoltage protection. The capacitor, C6, C5, C3, and C2 are decoupling capacitors. The resulting PCB schematic created in EAGLE software is depicted below:

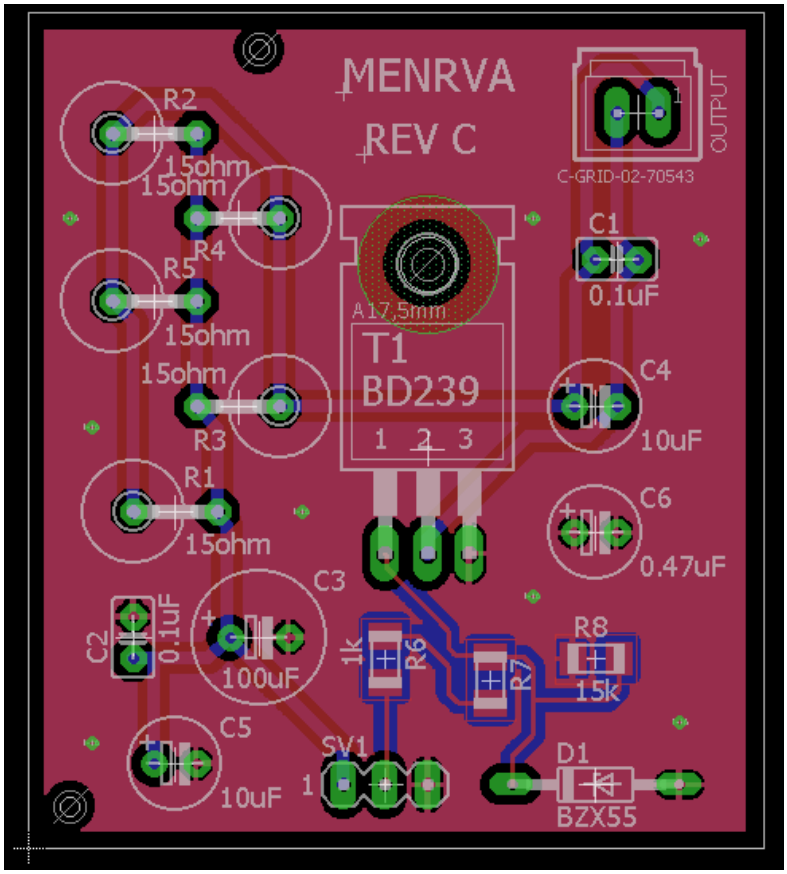

Figure 56. The gerber file view of the driver circuit

The designed PCB is a standard 2-layer board. Copper trace thickness is 2 ounces. Surface mount components were used on the signal side to save space. A screw terminal is used for the output to prototype wires. Due to the thermal nature of the system, one of the layers was almost entirely dedicated to ground with a near complete fill. This is done to help distribute the heat better and use the entire surface of the board as a makeshift heat sink. The manufactured PCB with all the components soldered on can be seen below:

Figure 57. The manufactured driver circuit PCB with all components on it

The PCB has a shared ground for both signal and power side. The red wire is VCC, yellow is signal input and black is ground. The output of this driver circuit is shown below:

Figure 58. Output of the driver circuit

As seen in Fig. 58, there are no more distortions in the circuit signal even at 16 kHz. In the figure, the yellow line is the input signal and the purple line is the output.

5.5. Joining Methods

5.5.1. Welding, Crimping and Soldering/Brazing methods

For this project to be successful, a good electrical connection as well a good thermal interface is required between the more resistive material that the actuator is made of and the conducting material that acts as the heat sink. However, as mentioned in the sections 4.1. and 4.2., copper and aluminum are dissimilar metals and cannot be easily joined together; despite having excellent heat diffusivity properties for cooling applications. At macro scale, the most common methods of joining them are crimping where one or both metal pieces are deformed to hold them both together or they are press fit together, or they are welded or brazed together. In welding the metals are joined by fusion where the base metals are melted together to create a bond that is at least as strong as the base material. Brazing and soldering are lower temperature metal joining techniques where a third material is melted at the joint area and cooled to create the connection. The base metals do not melt in brazing and soldering.

Crimping, or contact method, was the first method explored because it only required constant pressure over the contact area. For this, a copper thin foil was wrapped around the thin aluminum wire or sheet to form one side of the actuating bridge and pressed together using a laser cut plexiglass piece that acted as a type of ‘C clamp’. Another 100-micron glass slide with copper on each side was placed in between the layers to electrically isolate them. The pressure from either side of the wire pressed the aluminum wire into the soft copper thin foils, creating the desired electrical and thermal connection. One of such samples with a 20-micron aluminum wire can be seen below:

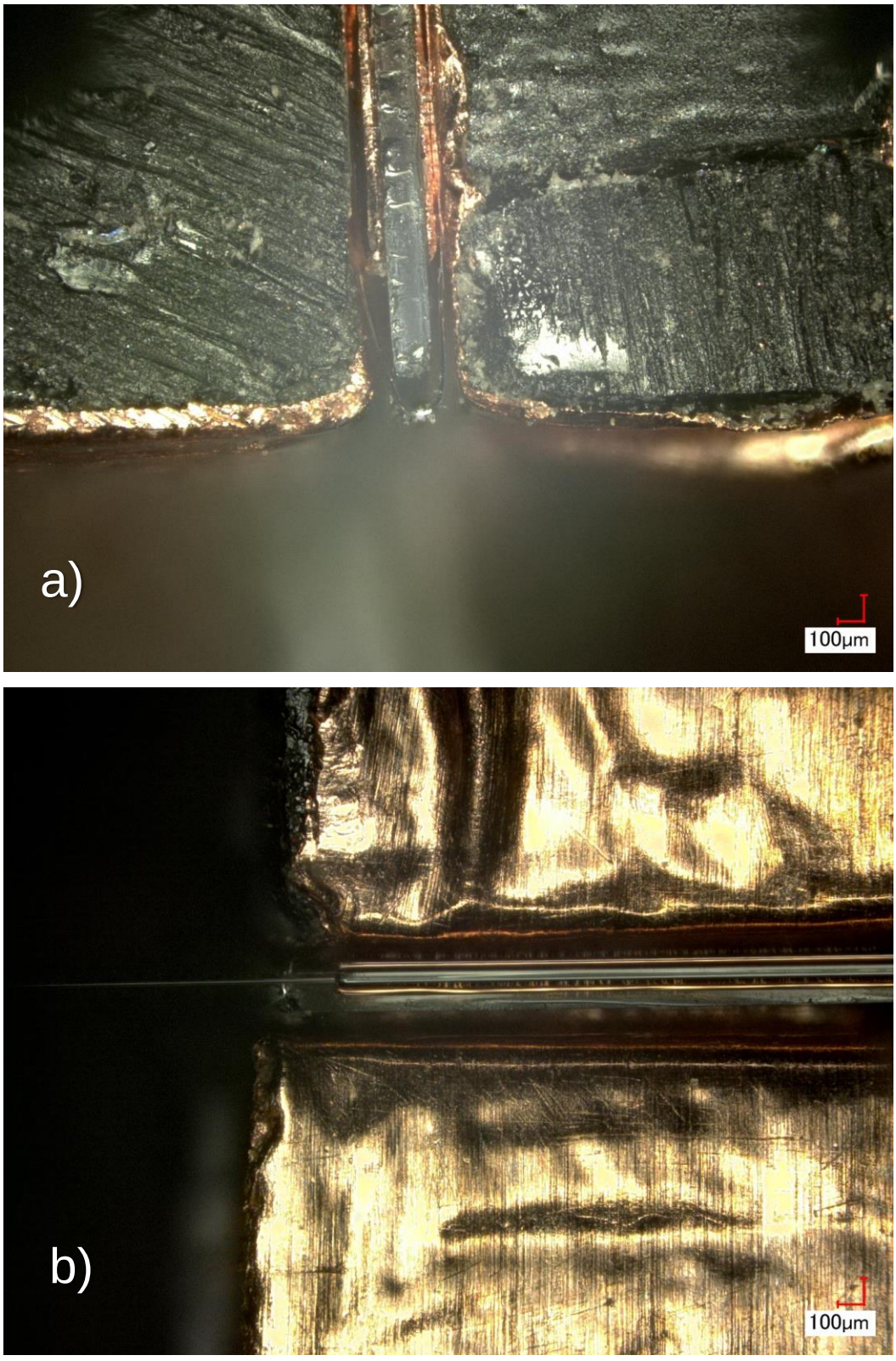

Figure 59. **A 20-micron aluminum wire and copper thin foil prototype made using the contact method; (a) front view (b) top view**

The contact method worked fine in terms of creating a near perfect electrical connection. However, a lot of pressure was required to create and maintain the connection and while the large-scale prototypes seemed to work fine in this set up, no possible way in which this could be replicated at the final desired dimensions was seen. In addition, this process made the task of aligning and fixing the fiber and other pieces extremely difficult and time consuming due to the number of small pieces that had to be aligned, placed and kept together with no adhesive. Therefore, the contact method was crossed out as one of the possible joining methods.

The most common method for joining aluminum to aluminum or aluminum to copper is arc welding; gas tungsten (TIG) and gas metal (MIG) arc welding to be more specific. However, this method was explored and quickly dismissed. A shielding gas blowing over the entire set-up would misalign and misplace the pieces before they could be fixed and joined to other parts permanently. Furthermore, for these procedure, the aluminum surface has to be thoroughly prepped and cleaned of any aluminum oxide by either physically brushing the surface to remove a layer or using corrosive acidic gels; neither of which would work in this application. Also, the thin metal sheets and wires were found to be incapable handling an electrical arc, unsurprisingly. Nevertheless, in order to verify this, an arc welder was constructed in the lab using a 45 V boost converter and a couple of high capacity capacitors but not matter the voltage, charge, or discharge time constant, the thin 20-micron aluminum wire literally vaporized because of the electrical arc and craters were formed in the copper thin-foil (25 to 50-micron copper foils).

Welding methods such as electron beam and laser welding were examined too; both commonly used in MEMS devices. Electron beam welding works by heating the piece by focusing the beam of high velocity electrons at the weld spot. The kinetic energy of the electrons is converted into heat when it hits the work piece which has to be contained in a vacuum chamber and it must be a conductor. However, electron beam welding has lower penetration making it not suitable for lap joints and it is not very precise and very expensive. An electron beam welder could not be accessed for testing and verification purposes. In laser welding a laser spot is pulsed over the weld regen to create a keyhole melt pool at the joint interface and weld to the two materials together. Nevertheless, these two methods are generally used for flange, tee, and butt joints of similar metals making them unsuitable for this application. It is important to note that

even with the a clean and oxide free aluminum surface, a copper to aluminum joint is very hard to make because of the extremely strict set of conditions needed for it. It is not impossible but very difficult and even with a successful weld, the resulting joint will be inherently brittle and susceptible to galvanic corrosion. The copper-aluminum phase diagram is shown below, the very narrow strip on the right side of the graph is the target area required for a joint [41]:

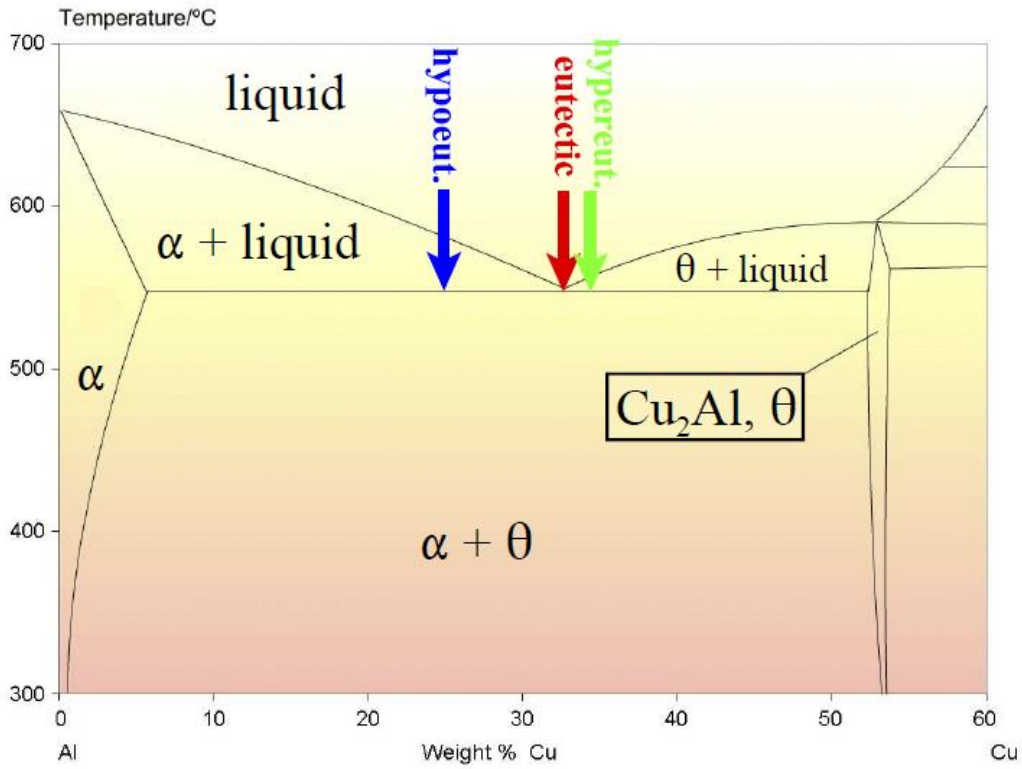

Figure 60. Cu-Al phase diagram, the narrow strip on the right side is the target for a weld

The method of ultrasonic welding was explored as well. Ultrasonic welding works by applying pressure, high frequency vibrations (60KHz typical) and heat to a point producing a localized slip and plastic deformation between the parts which rolls up oxide and contaminant films to create a solid phase weld. Removing any need for surface preparation. Most applications are foil and thin sheet. It is also used for joining fine wires to pads on PCBs. Weld time is very short (about 1 sec). The same process at the micro scale is called a single-point tab bonding. This makes it extremely desirable and suitable for this project. Multiple manufactures were identified and contacted. Although, they were confident that single-point tab bonding would work for our case, the quoted device

prices were in the order of one to two hundred thousand dollars and prohibitively expensive. Nevertheless, these devices are commonly used in chip manufacturing facilities and one such bond is depicted below [46]:

Figure 61. 25-micron wide copper ribbon cable bonded to a gold pad inside of a hard drive

Spot welding was another method explored. Spot welding is a type of electric resistance welding and it works by pressing the two pieces in one spot together and passing very large amounts of current through the spot, heating the piece due to electrical resistance and forming a small pool of molten metal which forms the weld. Spot welders are meant for relatively thin materials. Due to the nature of this project, dimensions and materials being welded, very fine and granular levels of control is needed. One company, Sunstone Welders, produces a line up of capacitive discharge micro spot welders designed for welding thin foils [47]. Multiple test samples were sent to them and they were able to successfully weld thin foils (20 to 25 microns thick) of copper to brass, bare copper to aluminum and nickel covered copper to aluminum without punching holes in them. One such device has a price of about fifteen thousand dollars US. A micro spot welder might be purchased from them for this project.

The last method explored for joining copper to aluminum is brazing. Brazing is similar to soldering. However, it typically happens at temperatures higher than what is achievable with handheld irons and the filler metal relies on capillary action to flow into the gap between the parts being joined. Gas torches or furnaces are often used for brazing. Brazing is used to join copper pipes to tubes on aluminum heat exchangers at an industrial scale. For this, both pipes are brushed, and an aggressive acidic flux paste

or gel is applied to remove any remaining surface oxide, then, the pipes are fitted inside of each other and the bond area is heated to the filler metals melting point and finally the filler rod is placed on the heated area to melt it and complete the brazing the process. In order to replicate this process at this scale, various aluminum and copper brazing fluxes and filler rods were tested. As previously mentioned, brushing and trying to physically scrape the oxide layer off just results in thin foils being ripped. The filler rods were all different alloys of aluminum with melting temperatures of 400-600 $°C$. The fluxes had zinc chloride, potassium fluoride, lithium chloride, sodium fluoride, potassium chloride and phosphoric acid as active ingredients to attack aluminum, aluminum oxide, copper and copper oxide. A propane torch with a fine head had to be used to achieve a somewhat reasonable level of control over the flame size at the desired temperatures. The gels were extremely toxic and corrosive and remained in place till they were melted and burnt off by the torch flames during the brazing process and outgassed noxious fumes. So, it was important to wear proper respirators, gloves, goggles and use a fume hood during the process which resulted in further complications for an already complicated and cumbersome task. Some of the results from trying to braze copper and aluminum thin foils is show below:

Figure 62. A 20-micron aluminum thin foil after applying the brazing flux for the minimum amount of recommended time

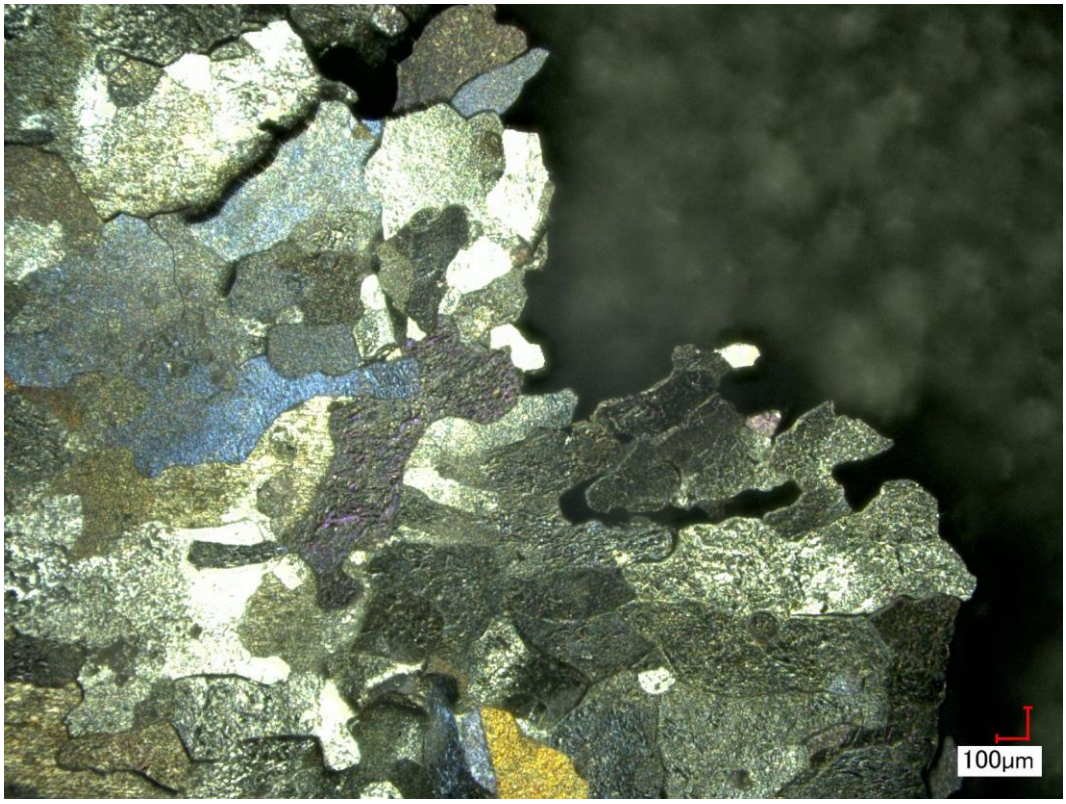

Figure 63. A 20-micron aluminum foil after applying the brazing flux for the recommended time

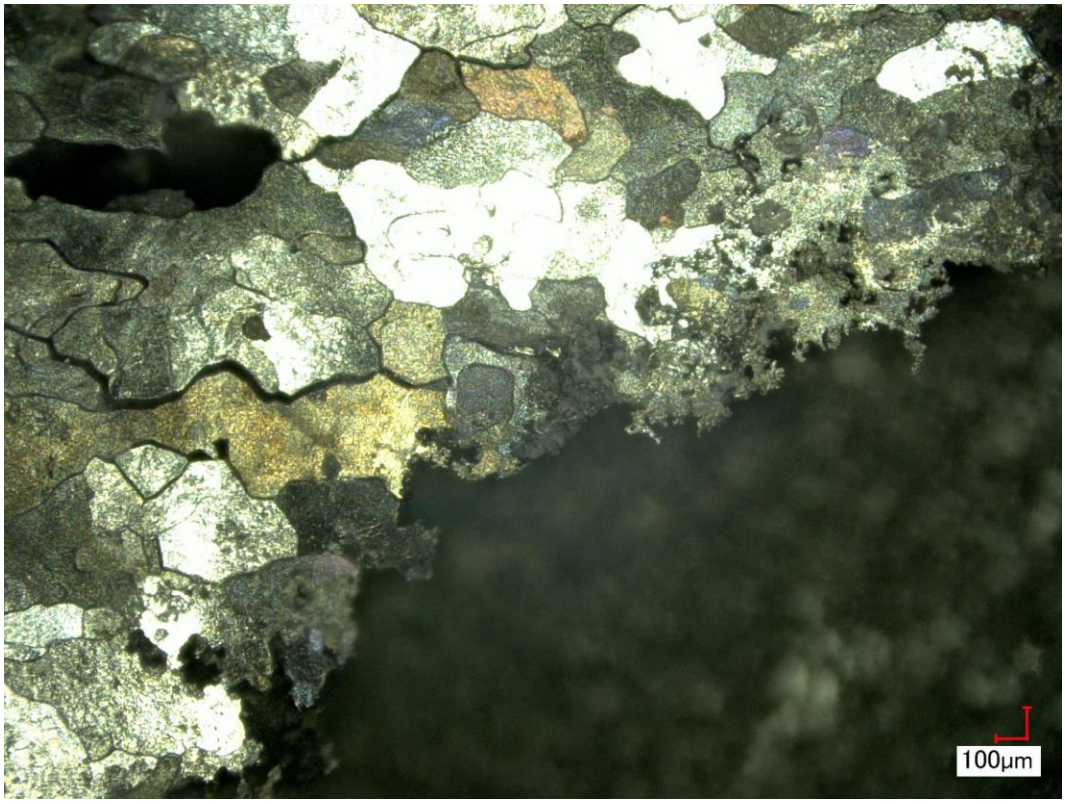

Figure 64. A 25-micron copper foil after applying the brazing flux for the recommended time

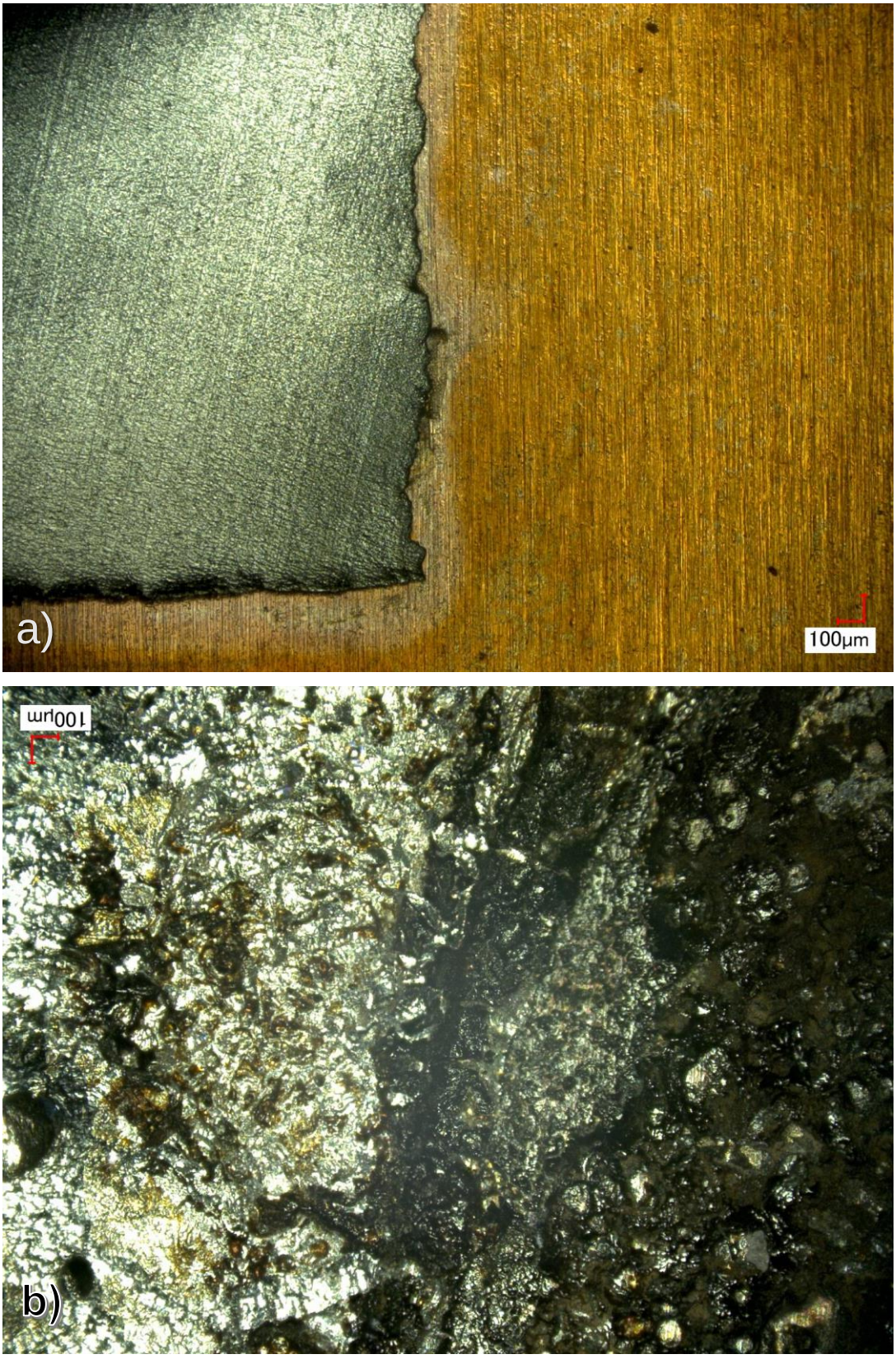

Figure 65. Result of brazing using a torch; (a) the prepared lap joint before brazing (b) result after brazing

As seen in Fig. (62-65), the flux pastes are so corrosive that they will quickly eat through the entire thickness of the thin foils in a matter of a few minutes. This was the result with all flux solutions purchased. The resulting braze joint was no better when a propane torch was used which resulted in damage to both metals because of lack of fine control both in terms of location and temperature. Both the joint and base metals were extremely brittle after the procedure too.

Therefore, the procedure for brazing was revised. Small shavings of the filler rod were placed on the lap joint location, very small amounts of flux were applied to only the joint location using a syringe and the piece, fixed to a glass microscope slide, was immediately dropped onto a hotplate. As soon as the filler metal melted the piece was removed from the hotplate and dipped in water to start neutralizing the flux. This increased control over temperature, alignment, time and amount of filler and flux used resulted in somewhat acceptable joints in terms of the quality and size. The picture below shows joint interface using the described method:

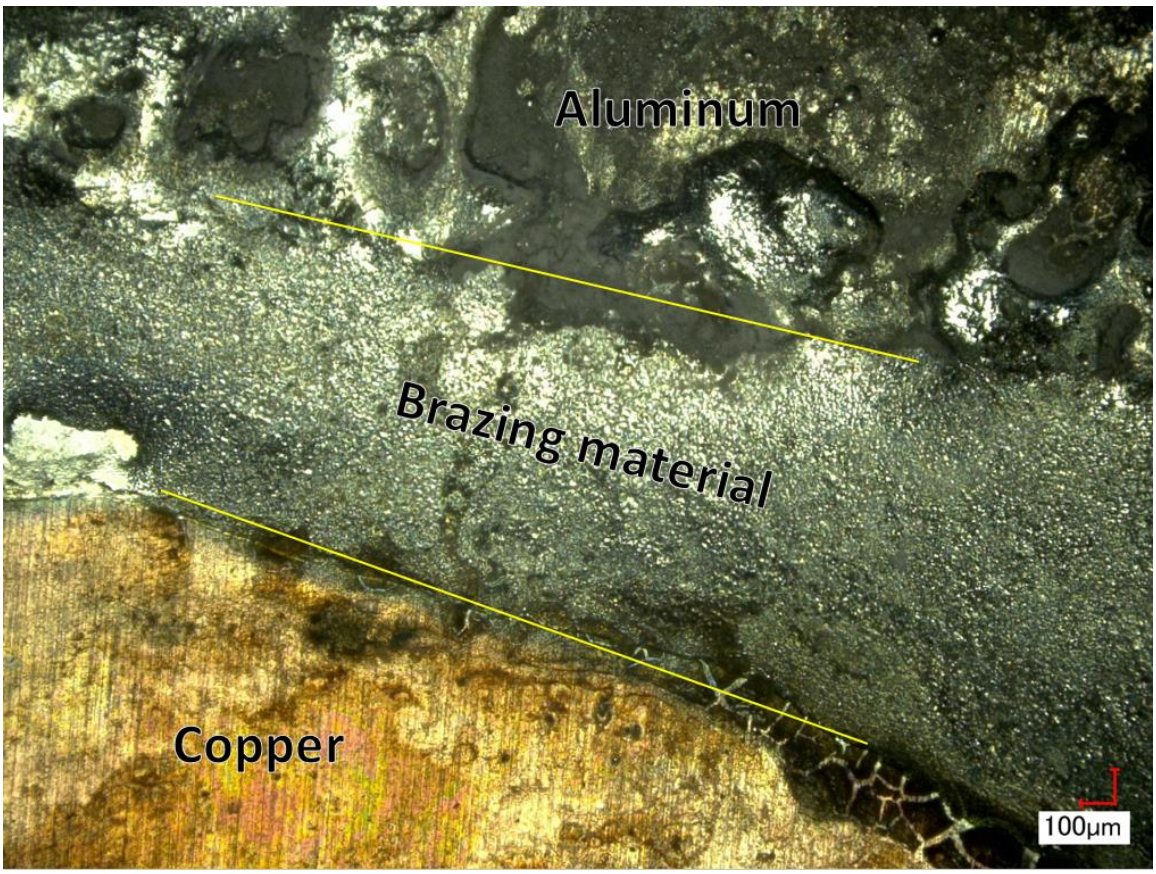

Figure 66. Brazing result after fine tuning the process on a hot plate

Low temperature filler rods seemed to do better than their high temperature counterparts, creating cleaner joints. In theory this should work significantly better than a soldered joint because the brazing filler is a high aluminum alloy. Even though, this set of experiments showed that brazing could potentially be used in this project to create the desired joints, overall it was a very awkward and cumbersome process that did not quite deliver the level control needed at the desired dimensions. So, no actual prototypes were made using brazed joints, but this could easily change with more work and fine tuning on it.

In short, many potential methods for joining copper and aluminum together were explored and a few were chosen as having potential to work. The table below summarizes the findings:

Table 3. Summary of copper-aluminum joining methods

Joining method	Can it work?	Reasoning/Comments
Contact	Not at micro scale	No way of providing the needed pressure
Arc welding	No	Just not the right application, parts too small
Electron beam	No	Poor level of penetration, poor control of targeting, expensive
Laser welding	No	Not good for lap joints, especially with Cu-Al
Single-point tab bonding	Yes	All indications point to it working, very expensive
Capacitive discharge spot welding	Yes	Works, not yet ordered due to price
Brazing	Possibly	Can potentially be used in project with more work and fine tuning

The methods presented as being able to join copper and aluminum together are also capable of being used to join alloys of copper (like brass) to copper.

5.5.2. Adhesives

Adhesives have been used throughout this project to fix the fiber and the platform (used to adjust the height of the fiber relative to the dimensions of the bridge) in place during the final assembly. Materials that need to be bonded together are metal, glass and various polymers. Furthermore, they should not shrink and expand during and after the curing process because that would misalign the fiber and bridge and it should be

hard enough that it does not dampen the vibrations (an absolute necessity for a fixed-free cantilever model). This limits the choice of adhesives. Initially the adhesive of choice and what was solely used in the fabrication of large scale prototypes presented in section 4.1., was Loctite 495 [48]. Loctite 495 is cyanoacrylate type glue, meaning it reacts with the moisture in the air to form long polymer chains to order to harden and set into a porous open celled sponge. Almost all commercial 'super glues' are of this class of adhesives. Loctite 495 was seen favorably for this application because it is a transparent, colorless (almost the same index of refraction as the fiber), low viscosity (can easily be applied to the desired locations), bonds all the materials used and cures at room temperature by itself in less than a min and at the time, appeared to be hard. The Shore scale is used to measure the hardness of rubbers, polymers and plastics that range in hardness from soft and flexible (scale OO), to medium and somewhat rigid (scale A), to hard with almost no flexibility (scale D). Cyanoacrylate glues generally have a hardness of about 85A and that was thought to be hard enough for this application. There is an overlap on the scales and a material with a Shore A hardness of 85 is about 35 on a Shore D hardness scale. For reference, car tire tread has a Shore hardness value of 60A, golf ball 60D, flexible epoxies 35-60D, rigid epoxies 70-90D and bone 100D (set as max hardness in the Shore scale).

After the disappointing performance of the large-scale models and investigation into the possible reasons, it was determined that Loctite 495 is not all that hard at room temperature and quite flexible. In addition, the performance of large scale models (tip displacement), instead of being linear as a function of power through the actuating wire, was rather logarithmic and started to plateau after a certain input power or even started to regress. This indicated at higher temperatures a couple of things could be going wrong. Solder as a culprit was already identified and discussed but this pointed to other issues as well. In order to understand what exactly is going on, it was important to know exactly how hot the actuating bridge is getting at the higher operating bounds and limits of the system. To measure the temperature of the bridge empirically, a special k-type thermocouple tip was constructed using 40-gauge wires. Then, this small thermocouple was inserted into a ball of carbon based thermal paste that covered all of the bridge. The power through the bridge was gradually ramped up, stopping at every interval to make sure the temperatures was at steady state before recoding the temperature. The temperature measurements are presented in the following graphs:

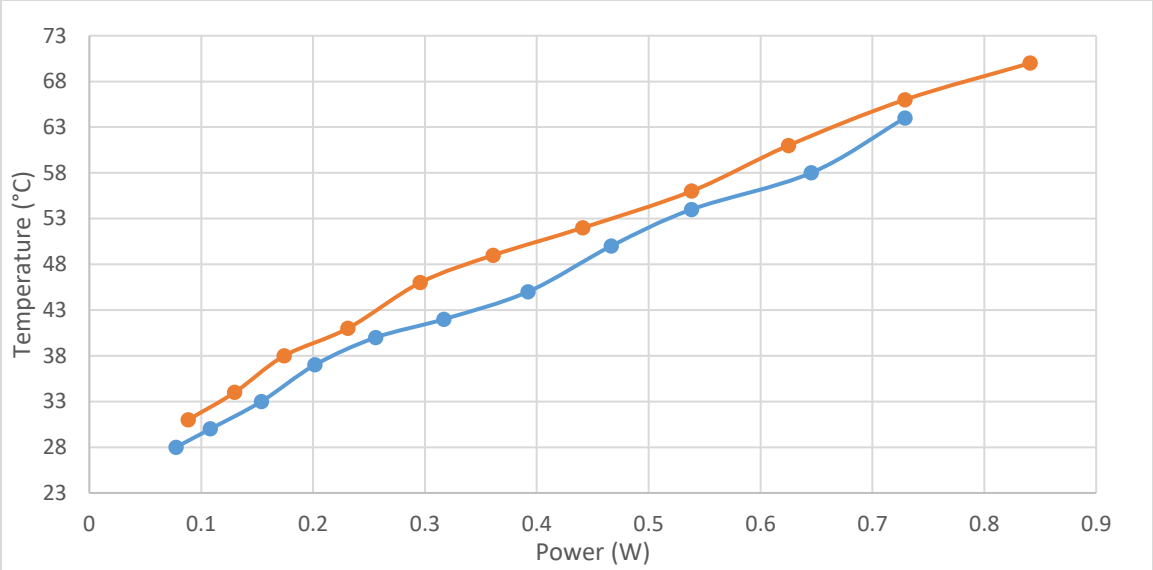

Figure 67. Temperature measurement of two different 150-micron tall brass actuator samples

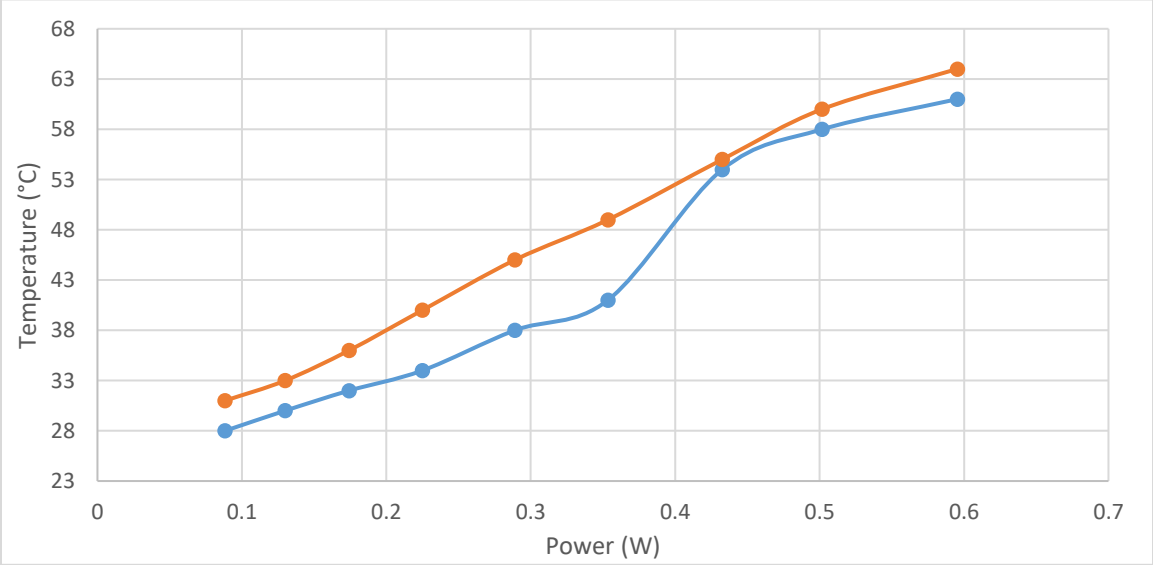

Figure 68. Temperature measurement of two different 150-micron tall aluminum actuator samples

Please note that the temperature measurements are gathered from samples made from one piece of laser cut thin foil. This method is presented in subsection 5.6. As seen in the graphs at the upper limits of the system (0.6 to 0.8 W), the metal foil has an average temperature of approximately 60-70 $°C$. This means that over time at higher levels of power, the adhesive holding the parts together can reach those temperatures as well. This is a problem because almost all polymers soften at higher temperatures. The hot strength of Loctite 495 is seen in the figure below:

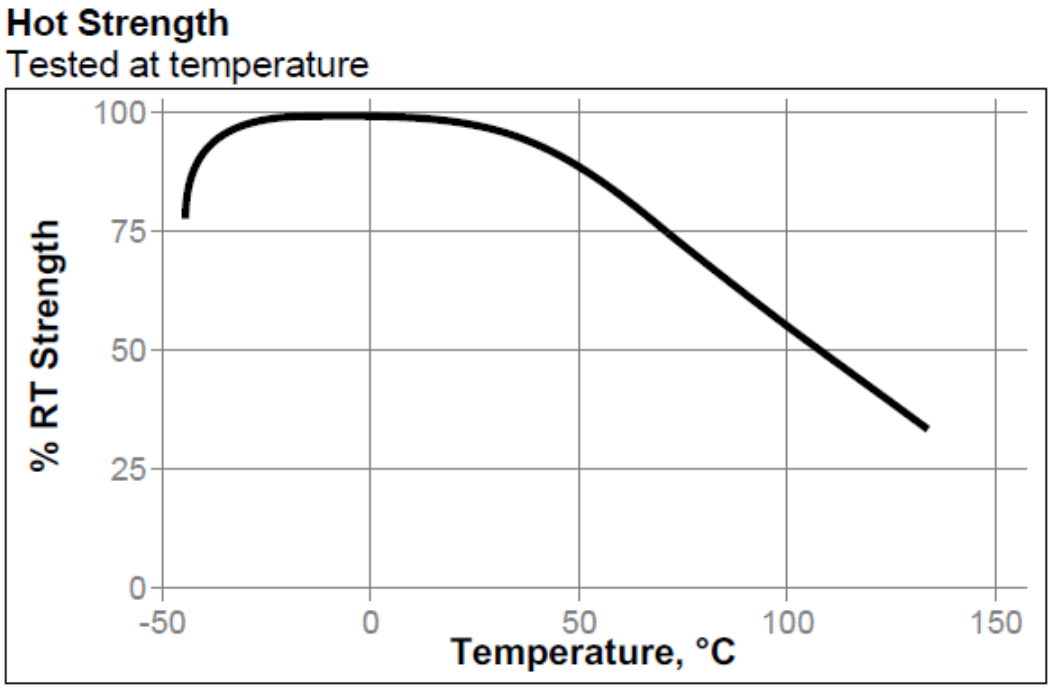

Figure 69. Strength of Loctite 495 at various temperatures, taken from the datasheet

This introduces another requirement to the selection process of the adhesive; the glass transition temperature. One that is difficult to address because most classes of adhesives that can withstand high temperatures are either soft and rubbery or cannot bond metals and glass together and adhesives that are hard are only rigid at low temperatures. Loctite 495 starts to soften at temperatures higher than room temperature and turns almost into soft rubber at around 100 $°C$ (tested in the lab on a hot plate), making it unusable.

For this selection process, all basic classes of adhesives were studied. These included acrylic, anaerobic, cyanoacrylate, epoxy, bismalaeimide/polyimide, phenolic, polyurethane, silicone, thermoplastic hot-melt, poly vinyl and ceramic based adhesives. Acrylic adhesives, adhere to a variety of substrates, are water resistant, quite durable, have excellent optical properties and low toxicity. Their flexibility is dependent on formulations, but they can be 100% rigid with UV or electron beam radiation. The main feature of anaerobic adhesives is that they cure rapidly in the absence of oxygen to produce strong bonds at room temperature. They are chemically resistant to oils and solvents, have low shrinkage because they contain no solvents. However, they become soft at elevated temperatures. Cyanoacrylates are ‘instant’ one-part adhesives that bond

a wide variety of materials but have poor gap filling and offer low temperature resistance. Loctite 495 and almost all super glues fall into this category. Epoxy adhesives rely on chemical reactions to achieve very high strength and endurance on many different substrates. A wide range of mechanical properties depending on formulation and curing can be achieved. They often have low shrinkage and have no by-products evolved during cure and are resistant to moisture, temperature and impact. Bismalaeimide adhesives are actually meant for high temperature applications offering operating temperatures upwards of 300 $°C$, and produce very stiff and strong bonds on a wide range of materials and the material itself is very dense and non-porous after curing. However, they produce volatile materials during the curing process, so extraction or high processing pressures are needed. Also, there are few commercial products available. The majority of these are designed for aerospace composite bonding applications and are very expensive. Phenolics are another class of high temperature adhesives that offer high mechanical and thermal strength and stability, good solvent and water resistance and are even flame retardant but they cannot bond glass or metals. Polyurethane adhesives offer good adhesion to a variety of substrates, have good chemical resistance to oils and solvents. They form tough, flexible and shock proof bonds and are available in many forms (e.g. liquids, dispersions, films, powders, etc) on top of being thermally resistant but they are too flexible for this application. Silicone adhesives are another group that offer a wide range of possible viscosities and are very resistant to high and low temperatures (-115 to 265 $°C$), UV and IR radiation, oxidation. They are cured by moisture or addition of cross linking agents. However, they too are very flexible and soft. Thermoplastic hot-melt adhesives offer high temperature resistance, rapid setting times, are easy to use and no special storage conditions is needed. They are solvent free, and a wide number of formulations are available for them with different properties like melting temperature and viscosity. Unfortunately, they are very soft as well. Poly vinyl acetates adhere to a wide variety of surfaces, have high cohesive strength and toughness and come in many viscosities. They are non-toxic, resistant to water, oxygen/ozone, UV and solvents and offer good mechanical stability and machining characteristics. However, they have low temperature resistance. Ceramic based adhesives can withstand very high temperatures; 400 to 1600 $°C$, far exceeding the capabilities of any polymer-based materials. They are also very resistant to harsh chemicals but cannot bond metals, glass or plastics [49].

Therefore, based on the requirements of this project, bonding glass, metals and polymers, high degree of hardness (80+ Shore D) and a high degree of temperature resistance, only epoxy and acrylic adhesives remain. After examining and testing many commercial adhesives, EP17HTND-CCM epoxy and UV25 UV cured acrylic adhesives, both my Master Bond Inc. were chosen for this project as the adhesives of choice. EP17HTND-CCM [50] (referred to only as EP17 for the sake simplicity from on on) is a one component high temperature resistant epoxy with the following standout properties:

- 80-90 Shore D
- Glass transition temperature of 235 °C (serviceable to 340 °C)
- Very good electrical insulation properties even at high temperature
- Black opaque color
- Flow profile suitable for glob topping

The curing procedure is slightly awkward however. It has to be heated at 150°C for about 2 hours and then post cured for 3-4 hours at 177°C. Similarly, UV25 [51] is a one-part moderate viscosity UV curable system with these properties:

- 80-90 Shore D
- Glass transition temperature of 185 °C (serviceable to 260 °C)
- Optically clear
- Fast cure upon exposure to UV light (~340 nm wave length)
- Adhesion to virtually all surfaces

After switching from Loctite 495 to these adhesives, a large performance improvement in lateral tip displacement was observed proving the softened glued was damping a lot of the vibrations by increasing the damping coefficient of the system. Performance results are presented and discussed in chapter 6.

5.6. Thermal actuator

It is important to remember that despite requiring micron level precision in fabrication, everything in this project is hand made and assembled. Therefore, any procedure that increases repeatability and reliability by removing any steps requiring

hand assembly is highly beneficial to the overall project. During the making the of large scale prototypes (section 4.1.), the single greatest fabrication challenge was the alignment of the round optical fiber on top of the round actuator wire. This led to low yield and many hours and days being wasted on the task essentially balancing two cylindrical objects, 12 to 50-micron in diameter on top of each other with a tolerance level of a few microns. Another big challenge was bending the actuator wire to shape and fixing it to the conducting wires. Even though, a few methods of joining the two together was presented in section 5.5.1., none of the devices required to do the task were purchased. This made it essential to think of a work around to move the project forward.

Many ideas were proposed and tested, but one method stood out from the rest; a laser cut thin foil, made from the same material as the actuating wire. It is important to remember that electrical resistivity increases proportionally when the cross-sectional area is decreased. Therefore, the resistive actuating wire can be made by cutting a narrow strip out of a larger thin metal foil and the metal foil that is still connected to it has a larger cross-sectional area and a relatively lower electrical resistivity. This means that the larger portion does not heat up as much as the narrow strip while maintaining a perfect electrical and thermal interface with it. This thin foil is then connected to the conducting copper wires, effectively creating a cascading design, with third level in between the actuating wire and copper. In order to cut the metal thin foils, the laser micromachining station at 4D Labs at Simon Fraser University [52] was used. In laser cutting/machining, a powerful laser spot is focused and pulse on the target area just long enough that it only heats up the pulse area high enough to vaporize without actually increasing the overall temperature of the material or surrounding areas. The laser system is an IX-280-ML manufactured by IPG photonics [53]. It features two separate lasers and beam delivery systems allowing for a high degree of flexibility. The first laser is an excimer deep UV (193 nm ArF excimer laser) ideal for precision micromachining of a wide variety of materials including glass and metals and the second, is a high powered QCW (1070 nm) laser used for thicker material cutting and drilling. The 2D laser cutting patterns are made in any CAD software that can output DXF files. The thin foils being laser cut are made of aluminum or brass and are 20 to 25 microns thick. In the CAD files, the actuating wire is supposed to be 25 microns wide but because of the laser cutter, cutting into the line by a few microns, the resulting strip is about 22 to 23 microns

thick which makes the actuating wires to have a cross-sectional area of 22x25 microns or 22x20 microns. A laser cut brass thin foil is seen below:

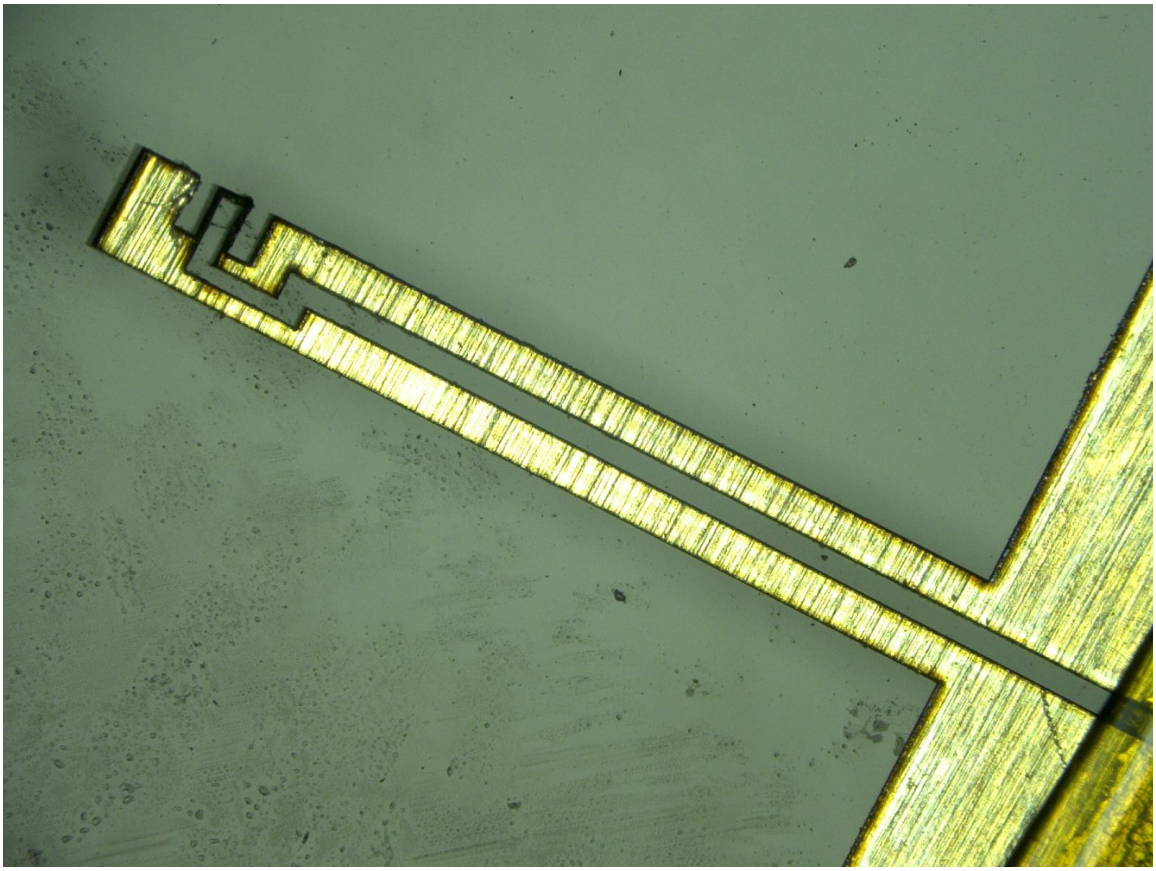

Figure 70. A brass thin foil cut into the desired shape[4]

The remaining pieces are removed from the surface by fine tweezers to leave what is seen in the picture above. Then, the bridge is lifted 90 degrees to an orthogonal position carefully to create the upright bridge. This method is very versatile in terms of creating the desired bridge shape and controlling its dimensions. The figures below show aluminum bridges that are 60, 100, 150 and 200 microns tall:

[4] This particular thin foil was laser cut by Yasong Li using the methods explained. However, this picture was used because it was the one of the nicer and only pictures of the thin foil cut-outs I have on file.

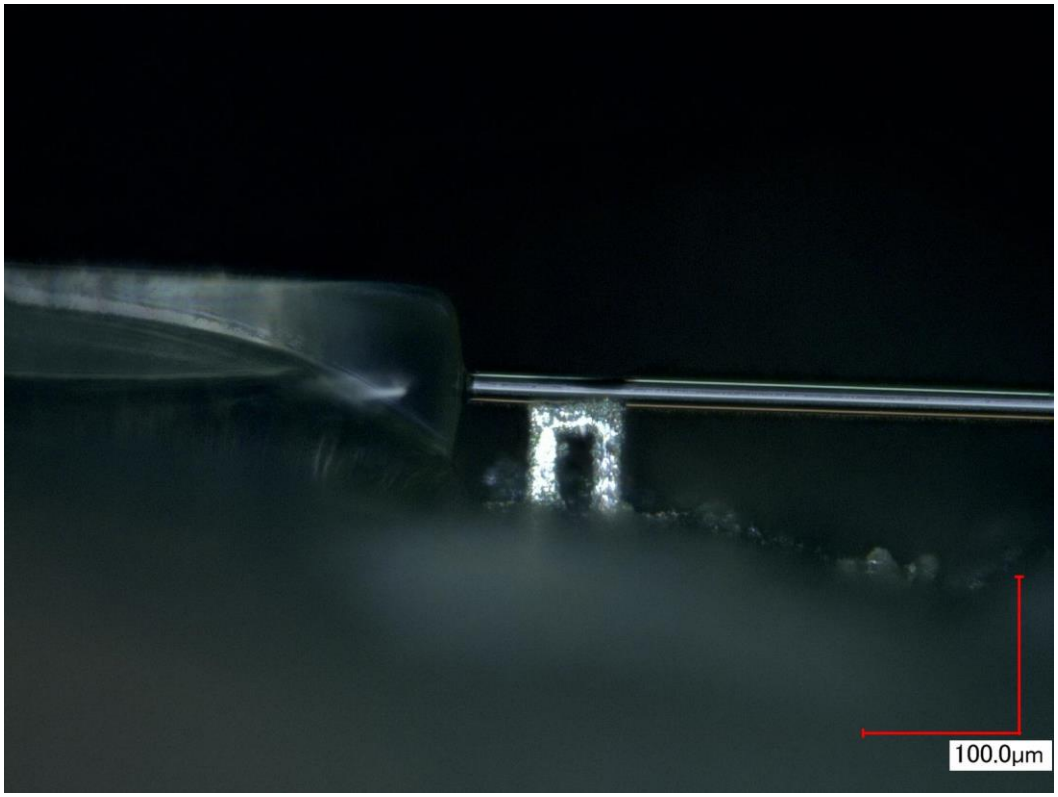

Figure 71. A 60-micron tall aluminum actuator bridge

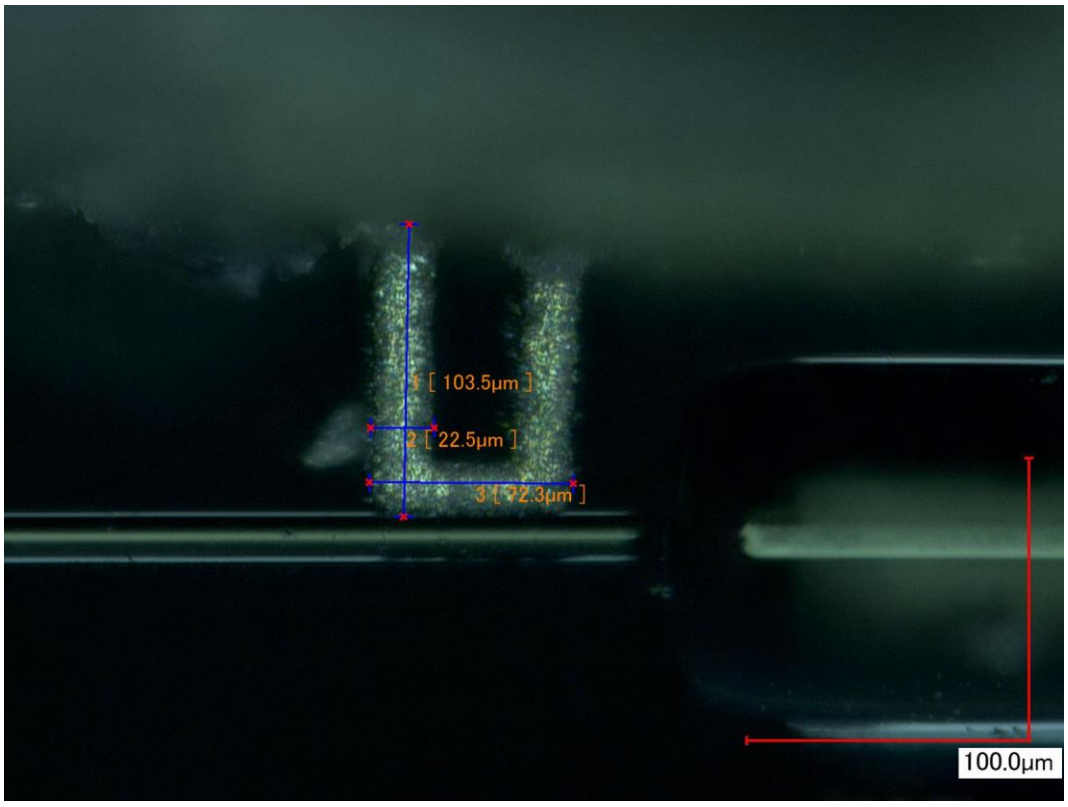

Figure 72. A 100-micron tall aluminum actuator bridge

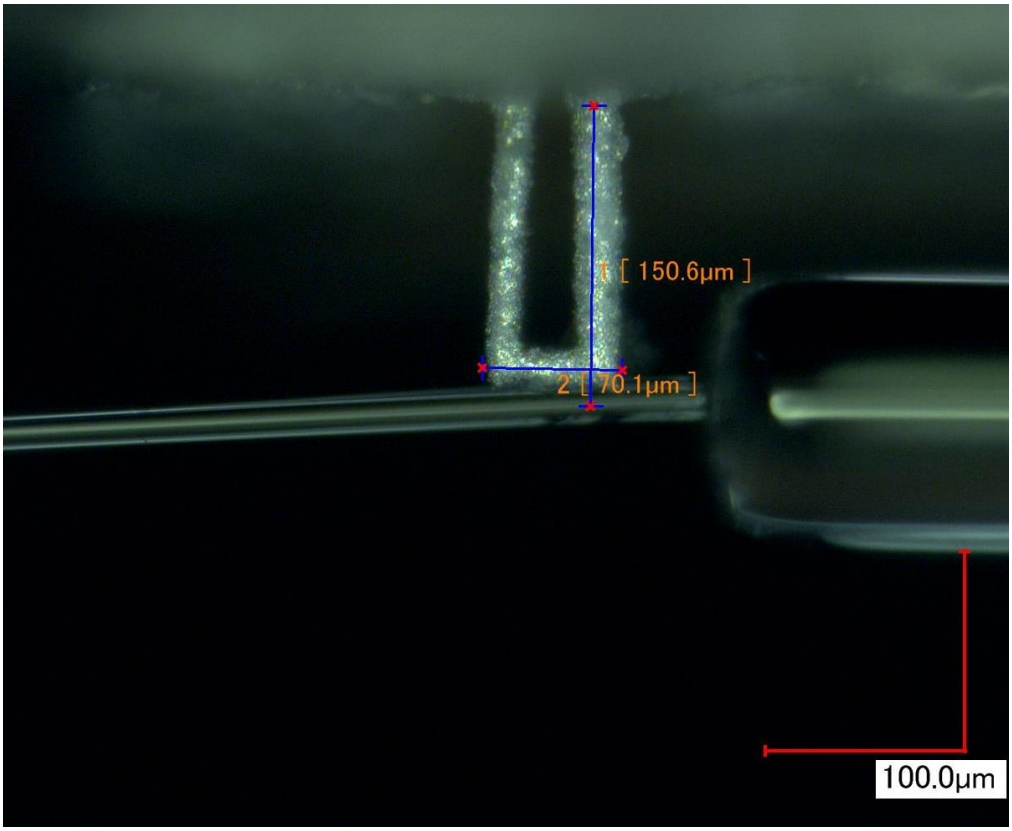

Figure 73. A 150-micron tall aluminum actuator bridge

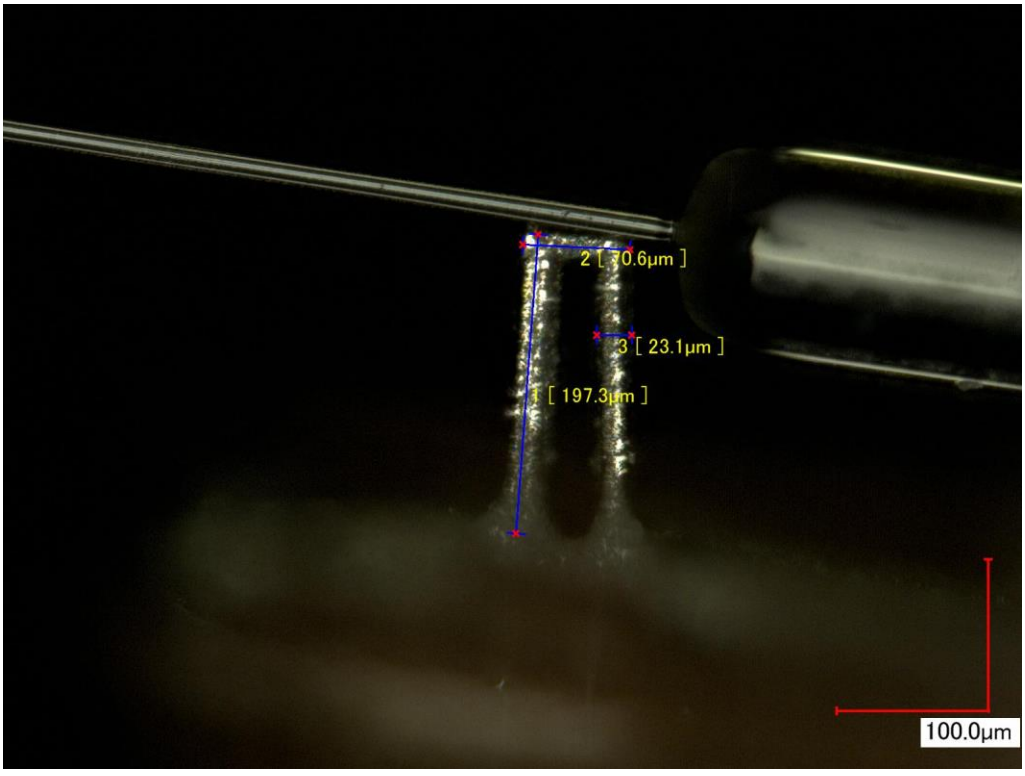

Figure 74. A 200-micron tall aluminum actuator bridge

Another advantage of this method is the incredible level of control that it gives it terms of alignment and placement of all the components in relation to together. The figure below highlights the fine level of control over the overall width of the device:

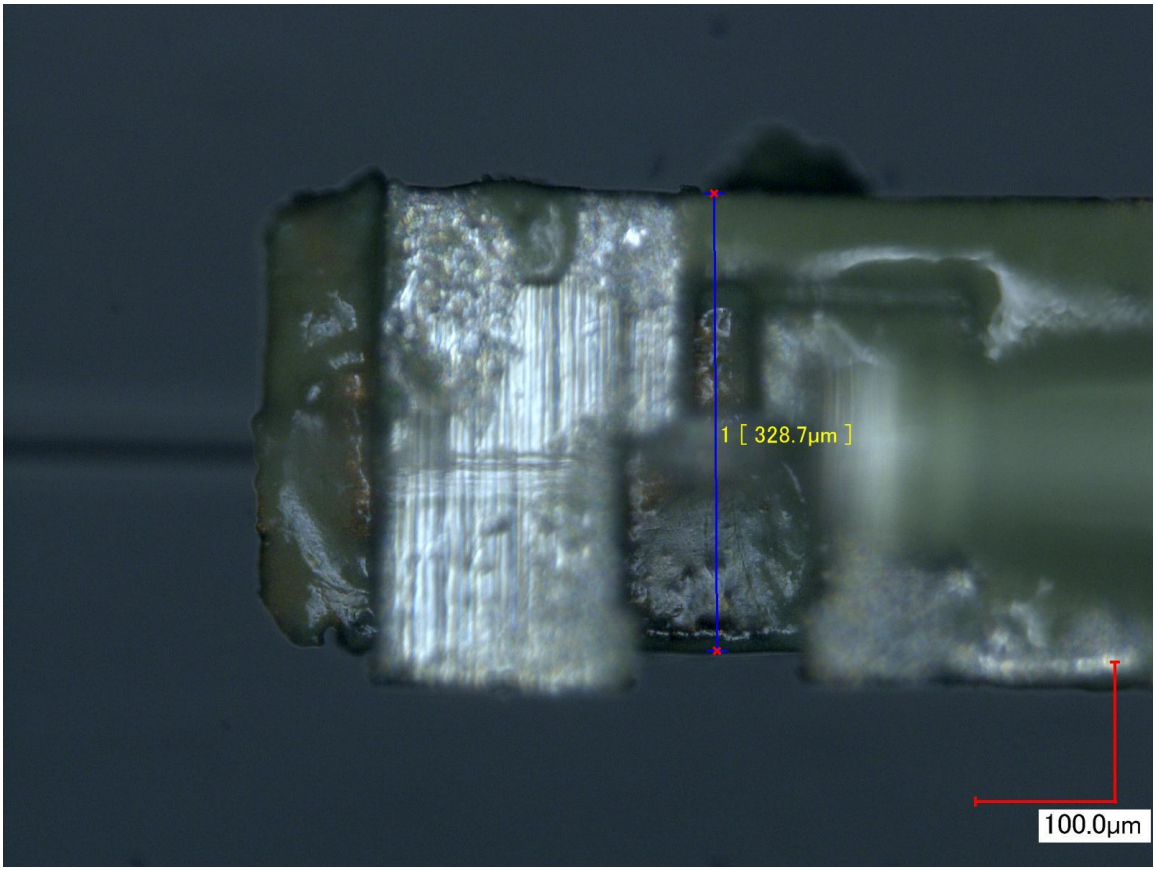

Figure 75. Top view of an aluminum sample attached to a backplate for rigidity

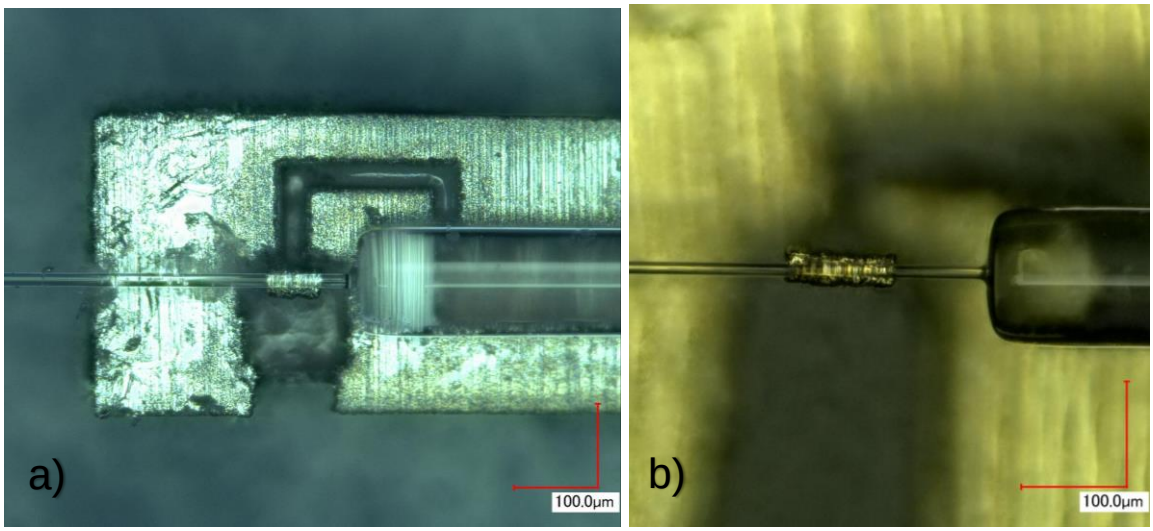

Figure 76. Two laser cut samples; (a) aluminum bridge (b) brass bridge

These cutout pieces are soldered to the copper wires at the back because of not having the required tools for a direct bond. However, as mentioned before, solder does not heat up by itself when current is passed through it. It still holds onto to heat but at the back, away from the actuating wire, it does not pose as big of a problem. It is not an ideal set-up, but it should do with what is available. In order to solder the aluminum cutouts, a strong flux is used in combination with silver solder and then the aluminum sheet is wrap around the copper wire and pressed down. This makes for an acceptable electrical connection, but it is very weak in terms of mechanical strength and quickly dewets and detaches under stress.

Instead of having a narrow cutout leading up to the actuating wire (i.e. what is seen in Fig. 70 and most samples), a couple of samples were laser cut with very wide side wings that had to be folded up in order to fit inside of the housing tube. This was done to for a number of reason. First reason was to make sure its cross-sectional area was big enough that going from copper to it, did not induce a sudden increase in electrical resistance and lower the thermal conductivity; thus, offering better thermal properties. Second, it was to increase the rigidity of the long and narrow and thin metal cutout like an I-beam. The samples with this feature had an excellent performance and the metal foil was indeed more rigid. However, due to the increased complexity arising from having to fold the wings to shape, and then dealing with the extra flaps, this design was put on hold. This winged design might serve well as a natural progression for the future iterations.

5.7. Housing and Packaging

This subsection acts as the logical conclusion for the work presented above. The main goal of this project is to make an endoscope system that is small enough to fit inside of a sub 500-micron housing. Early on, it was determined that it is impossible to assemble the device inside of the tube and everything has to be assembled and fixed in place first and then inserted into the tube. In order to achieve this goal, a series of acrylic (PMMA) collars and semi-circles were manufactured using soft lithography by Yasong Li to package the device while following the guidelines set for it in the previous subsections in this chapter. Yasong Li is a Post Doc working on this project in Dr. Menon’s lab, MENRVA, at Simon Fraser University. This work and accompanying figures are presented in Appendix A.

This method along with all the design decisions taken in this chapter show that it is possible to have a package that has an outer diameter of under 500 microns. In theory, nothing is preventing this design from shrinking down even further in size to about 300 microns in diameter. In addition, this combines for a rigid distal tip length of only about 3 to 5 mm which makes it possibly the smallest endoscope head ever. These results validate the proposed fabrication procedures in practice.

5.8. Methods Explored

As previously mentioned, the design went through more a couple dozen iterations before it morphed into what is presented in this chapter and a myriad of things were explored that did not make the cut. However, a few manufacturing methods were explored that showed promise but were not perused at the time. A number of them are presented here because they might provide an alternative to the current prototype design and be worthy of further considerations.

In order to fix the fiber in place in lieu of any rigid adhesives, brackets made of glass were imagined. They were to be made of glass slides; typically, about 160 microns thick. They were supposed to also help with alignment and keeping the fiber parallel at all times. However, the resultant 30-micron thick glass side walls did not survive the lasing process because of excessive heat. The side touching the anodized aluminum fared better in comparison due to the aluminum block acting as a heat sink. The results can be seen below:

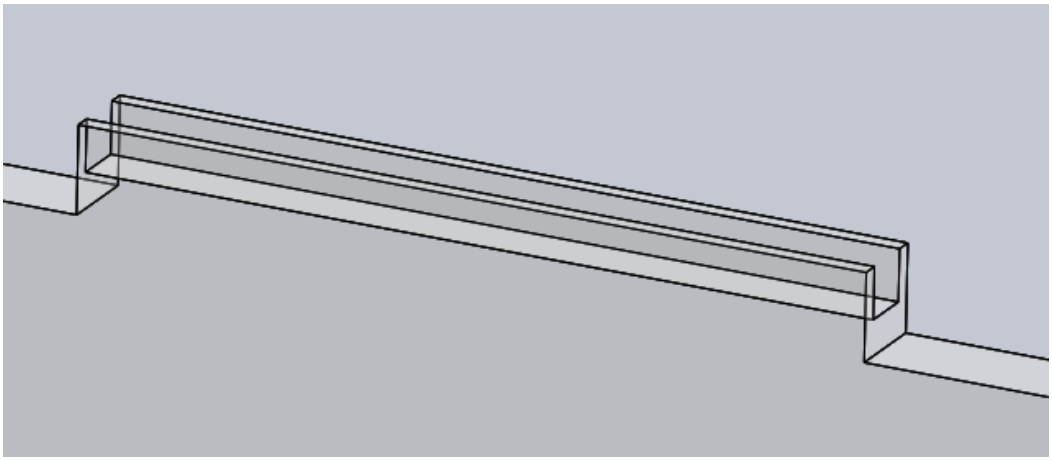

Figure 77. Solidworks model of the desired shape of the bracket

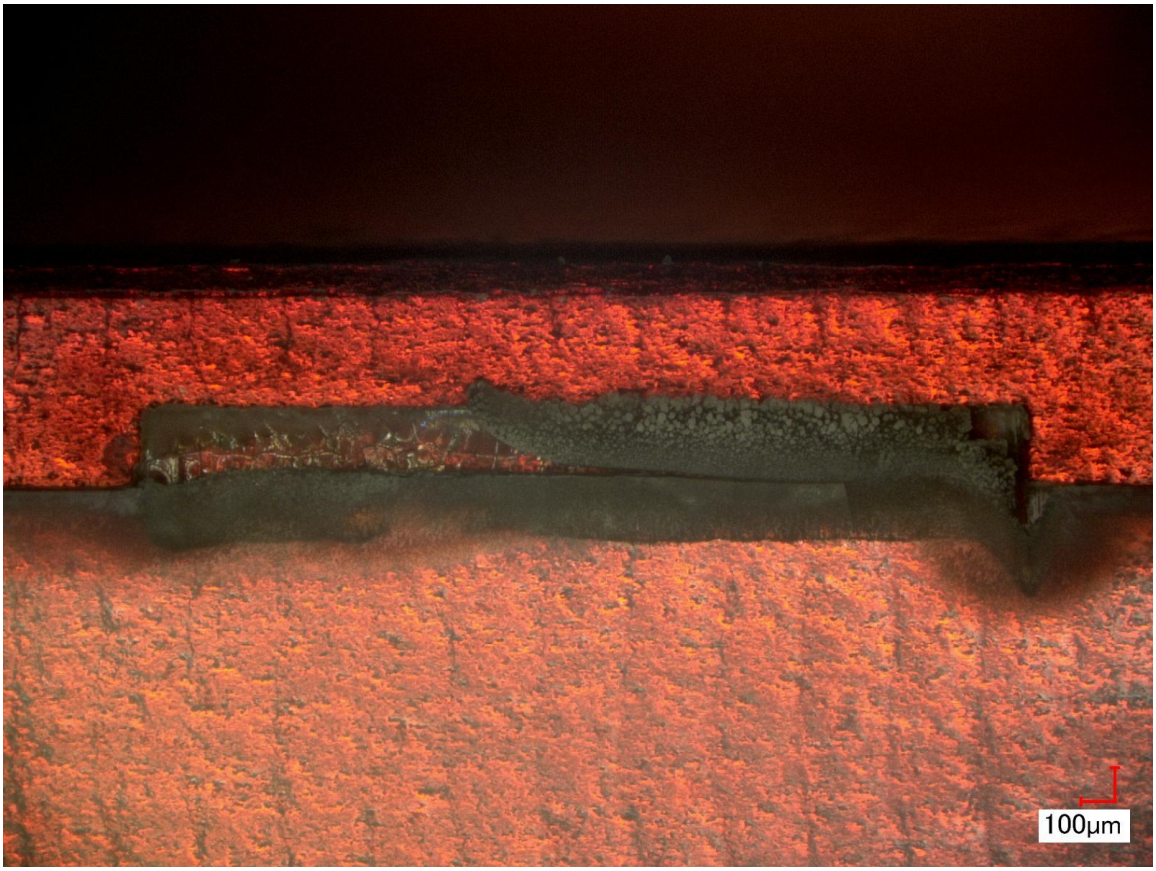

Figure 78. Front view of the glass slide after laser etching

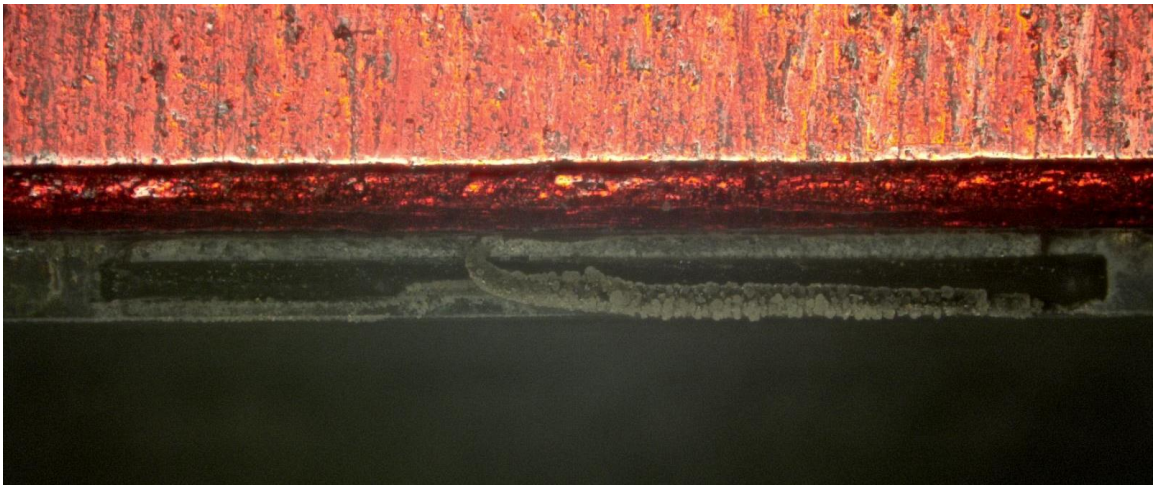

Figure 79. Top view of the glass slide after laser etching

With further work, better shielding of the piece during the lasing process and using a material with a lower coefficient of thermal expansion like borosilicate or sapphire, this method can be used to make complex holding brackets and improve the design in the future by increasing the rigidity of the fixture.

When the contact method was still being explored, about a half dozen all-in-one housing pieces were conceptualized to handle the task of aligning and holding the parts together while maintaining constant pressure. These parts might still prove useful in the head or tip of the endoscope to simplify the assembly process somewhat by already having a place for the parts inside of just a hollow tube. Two of these ideas can be seen below:

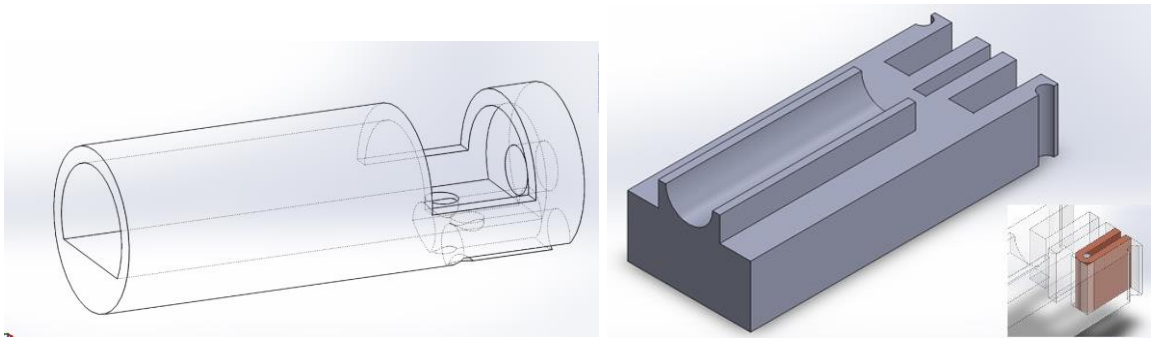

Figure 80. Two of the all-in-one housing head pieces meant to simply the assembly process

A literature review of micro-dispensing techniques was preformed, and three types of contact dispensers and two types of non-contact dispensers were examined and compared. Time-pressured, auger pump and piston valve were the contact mode dispensers and jetting and dynamic drop were the non-contact dispensers studied. The objective of the literature review was to explore the options for gluing the fiber to the top of the actuating wire. At the moment the fiber is either level with the top of the actuator, or it is below it by a few microns causing a preload and pushing the fiber into the actuator. It was determined that the desired droplet size for the top of the bridge would have the volume of about 11 picolitres. The smallest micro-dispensers, like ink jet printers can only dispense 2-25 picolitres of non-viscous fluids and there is none that can dispense that small of a viscous fluid accurately. Some jetting dispensers can atomize and spray the fluid over an area, but it is not precise enough to target only one small area. In addition, a blob of glue in between the cantilever and bridge might actually dampen the vibrations of the system and negatively affect the system. Nevertheless, more research can be done to improve the dispensing of adhesives in this project because at the moment all gluing is done by dipping a 125-micron thick optical fiber in glue and using it as a paint brush to essentially paint the glue on the desired locations. This method can certainly be improved.

As mentioned before, EP17, the main adhesive used in this design, due to its hardness and high glass transition temperature, requires a lengthy high temperature curing process. This process is taxing on a lot of the components like the optical fiber and also affects the metal thin foil. The effects of heat on aluminum and copper were studied under normal operating conditions and during the curing process required for the adhesive. During the curing process, aluminum and copper might be subjected to the first stage of the annealing process, recovery. In theory it should soften the metals slightly, but it should also increase their thermal conductivity. Further study is required in this matter.

Almost all materials that are thermally conductive are also electrically conductive. However, diamond is unique in that it is one of the most thermally conductive materials, far higher than any metal, while being an excellent electrical insulator. The use of diamond dust was explored to improve thermal conductivity of the system. However, nothing that worked or made a noticeable different could be made. This is a new area of research and IBM is actually exploring using diamond as a heat sink in some of their chips and MEMS devices. Further research into this might prove useful.

5.9. Summary

The second objective of the study, which was to develop and configure a novel thermally actuated scanning fiber endoscope tip enclosure that met the ultra thin size requirements, was addressed in this chapter. The sub 500-micron outer housing diameter of the distal tip, required for accessing and imaging most of the lung passages, was set as the primary benchmark for assessing the success of the system design. Other considerations were the resonance frequency of the system and manufacturing time and cost. These dimensions and specifications make it the smallest head on any active endoscope ever.

In order to achieve this feat, a materials selection study was performed based on thermal conductivity, coefficient of linear expansion, electrical resistivity and Young's modulus. This presented a challenge because resistive metals often do not have a good thermal conductivity value. Nevertheless, by the method of elimination based on each criteria, aluminum and copper alloys were chosen as suitable materials for the actuator bridge and copper and silver for the conducting wires doubling as heat sinks.

Based on equations derived in section 3.1.1. it was demonstrated that frequency of the cantilever and by association the sample rate of the endoscope could be modified by changing the physical dimensions of the illumination portion (thin segment) of the optical fiber. It was explained that even though higher frequencies are desired, it should be balanced against the need for higher lateral tip displacement.

The problems with the initial driver circuit design were addressed in a new design. A new PCB was also designed with some thermal shielding and heat dissipation features in mind. It was tested and shown to work with no distortion even at frequencies higher than needed.

An overview of joining methods used to bond aluminum and copper at macro scale was given. Inherent problems with this process were explained. Afterwards, each method was examined to determine its feasibility to be applied to micro scale parts. Welding methods, DC linear spot welding and single-point tab bonding were identified as two methods that would work at this scale for this application for both aluminum and copper alloys. However, neither one was purchased because of their price tag. High temperature brazing was also examined and was thought to have the potential to work. Though, more work and fine tuning is required before it can be put to use.

On the issue of adhesives, it was demonstrated that the old glue used for the initial batch of prototypes was indeed softening at elevated temperature, increasing the damping coefficient and degrading the magnitude of tip displacement. The equations presented in section 3.1.1 are based on Euler-Bernoulli beam theory and rely on a cantilever with a fixed end. So, it was paramount to find a rigid adhesive that had good temperature resistance. After studying all major classes of adhesives and testing many products, EP17 epoxy and UV25 acrylic adhesives, both by Master Bond, were identified as being suitable for this project. Both adhesives are very hard and maintain this rigidity at high temperatures because of their high glass transition temperature. Use of these adhesives on subsequent prototypes resulted in a tangible improvement in performance.

In order to get around the issue of alignment, shaping the actuator wire and joining it to the conducting wires, a novel approach was introduced based on laser cutting a single piece of thin metal foil made of the same material as the bridge. This meant, the actuator was no longer a round wire, easing the alignment and placement

task. In addition, this created a near perfect electrical and thermal interface for the actuator bridge, something that was a big issue in the initial prototypes.

The final section of this chapter, combined all the previous steps together and demonstrated that they can be used to package the system into a sub 500-micron tube with the use of custom made acrylic support structures.

The design presented in this chapter showed that not only it can be used to meet the strict size requirements, it can easily exceed them thus achieving the second objective of this study. A distal tip diameter of 300 to 500 microns and a rigid distal tip length of 3 to 5 mm makes this device far smaller than any other previous art, presented in section 2.2.

No official cost analysis was performed but based on the relative straight forwardness of the design and low number of pieces (compared to devices available currently), it certainly has the potential to be low cost enough to be made disposable eventually.

Chapter 6. Experimental Performance Assessment of the Ultra Thin Endoscope Prototype

6.1. Experimental Testing Overview

This chapter sets to validate the design presented in the previous chapter through experimentation in accordance to objective 3 of this study. The aim is to assess the performance of the proposed design to prove it is capable of achieving the goals set for the project. The size requirements of less than 500-micron distal tip diameter are already addressed. So, this chapter is dedicated to examining the lateral free-end deflection amplitude of the center illumination fiber and frequency at which it happens. These parameters are two of the important factors in determining the resolution and quality of the resulting images. The magnitude of displacement dictates the resolution of the images. It is the lateral amplitude divided by the core diameter of the vibrating fiber. Therefore, 150 microns of tip displacement and a 3-micron optical core would result in a circular image that is about 50 pixels in diameter. A higher resonance frequency would mean a higher sample rate which in turn results in a more data points being collected from the surface being imaged and it also negates some of the inherent problems with the raster scanning pattern, namely the uneven scan density. So, naturally, higher displacement and frequency numbers are desired but as previously discussed, they are somewhat inversely proportional. A longer and narrower illumination fiber would result in a larger tip displacement because of the lowered flexural rigidity but it would also lower the natural frequency. So, it is a balancing act of trying to maximise lateral performance while maintaining an acceptable level of frequency. Most of the prototypes made in the latter stages of this project are just under 2 mm in length and have a natural frequency of about 2.4 to 3.3 kHz.

It is important to note and reemphasize that every single prototype is entirely fabricated and assembled by hand and the tolerances are in the order of a few microns. Therefore, no two samples are the same and while samples with the same configuration may perform similarly, each one is unique. These deviations can arise from many factors. Variations in the angle of the actuating bridge, the height of the fiber relative to the bridge, spread or amount of glue applied, curing procedure of the adhesive, the dimensions of the fiber itself (remember each fiber is also custom made), distance of the

fixed end of fiber to the bridge, size and length of the actuator, bridge materials, joining methods used, how well aligned the fiber is, how rigid the adhesive/platform is, etc. can often have a tangible and significant impact on the performance and behaviour of that particular sample. Over a hundred prototypes in various sizes and numerous configurations have been fabricated during this project. Therefore, the results presented in this section showcase the general behaviour and response of the design and reflect what it can be capable of and do not represent any one uniform singular sample.

6.2. Experiment Setup and Procedure

The goal of testing the prototypes is to evaluate their response to periodic input from the actuator bridge in the form of tip displacement and to characterize these oscillations as a function of power. Given the fact that the actuator bridges can come in different dimensions and thicknesses and can be made of various metals and therefore, can have different resistance values, power, measured in watts, is the unit of measurement for input. Furthermore, since the oscillations are caused by the expansion and contraction of the bridge due to cyclic resistive heating, using power as a unit for input just makes sense. This also makes it possible to have something that can be compared when comparing two different samples together. Prototypes can be simply modelled as time-invariant resistive loads; therefore, power is given as the resistance of the bridge multiplied by the square of current through it (Eq. 30, section 4.2). With the help of pull up resistors and adjusting the input voltage, the power through the bridge can be controlled. The typical test set up is seen below:

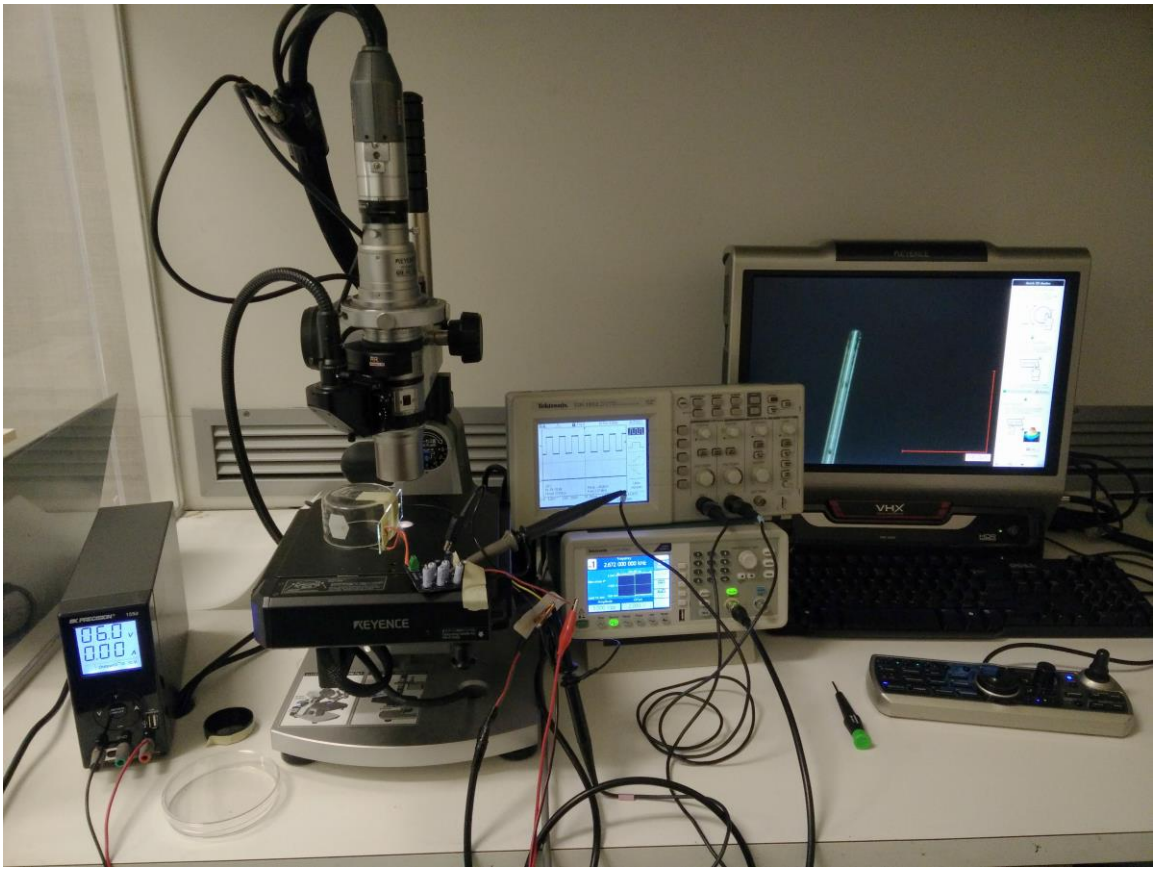

Figure 81. The test set up

In the test set up, an external desk top power supply is used as VCC and the common ground as seen in the circuit schematic (Fig. 55). An oscilloscope is used to monitor the signal input to the driver circuit and the output out of the prototype. This time around, for signal generation, a full-sized desk top function generator has replaced the small microcontroller used in section 4.2. As mentioned previously, the signal generated by the microcontroller was prone to oscillating from the set value or it would drift slightly; both of which can affect the performance (though this could have also been partly due to the shifting resonance frequency of the fiber). Unlike the microcontroller that has a small crystal resonator, the function generator uses an oven to heat up its larger crystal to always maintain a constant temperature. This enables the function generator to have an accuracy level of 1 ppm, meaning for example at 100 kHz, its output frequency is stable within ±0.1 Hz. It is important to maintain a stable frequency because if the system shifts from the intended target, then the system would not be at peak resonance or if it oscillates back and forth, then it would remain in the transient response region. This problem can be addressed with a resonator circuit, however. The output from the

function generator (a square wave) is connected to the signal line on the driver circuit and common ground, shared with the power line. The samples are attached to microscope glass slides for easier handling and are laid on their sides at either a 90 degree or less angle to observe the lateral displacement of the tip. The samples are often placed at an 80 to 82-degree angle with respect to the microscope objective to reduce diffractions caused by the microscope light hitting the edge of the glass slide. This is taken into account when measuring the lateral displacement and compensated for by simple trigonometry (final answer divided by cosine of 8-10 degrees). The microscope used to observe and monitor the tip displacements is an advanced 1000x magnification optical microscope; enough to provide high resolution images that can be used to measure the movement of the 12-micron diameter optical fiber to sub-micron levels, accurately.

Before starting the test procedure, the dimensions of each prototype are recorded using the microscope. These include the length and thickness of the illumination fiber, the distance from the base of the fiber to the actuator, height of the bridge, how well everything is aligned and many more parameters. For each sample, its natural frequency has to be found experimentally. The equations derived for finding the natural frequency of the system in section 3 are fairly accurate and can give a reasonably close estimation for the system being tested. However, due to variations in the fabrication process, those values are not exactly the same as the samples in real life. Nevertheless, the theoretical number does act as a good starting point. In order to find the natural frequency of the sample, the region before and after the theoretical frequency value is swept while the tip of the fiber is being observed. The exact natural frequency of the system is found when the tip of the fiber shows an increase in the amplitude of vibrations.

After the resonance frequency of the prototype is found, the input power is set to a lower voltage and then ramped up in small increments. The response of the system at each step is recorded to form a complete picture of the harmonic response of the prototype. In order to actually find the amount of displacement of fiber tip, the image from each step is inputted into photoshop and the magnitude of displacement is found by counting the pixels and converting that to a value in microns by using the scale in the image. This results in sub-micron level of accuracy when measuring the tip displacement.

6.3. Experimental Results

6.3.1. Harmonic Response

The main premise of this study is resonance vibration of a micro-cantilever under cyclic thermal excitation. In a structural system, any cyclic load will produce a sustained cyclic or harmonic response. Therefore, it is important to actually verify this claim and prove that the oscillations are indeed amplified significantly at the first natural frequency by doing a harmonic analysis. The results are used to determine the steady-state response of a linear structure to loads that vary harmonically with time. Normally this is performed to verify whether the design will overcome resonance, fatigue, and other harmful effects of forced vibrations. However, in this case, resonance is an intended effect and should not cause any damage to the micro-cantilever itself mainly because of its extremely low mass, as seen in section 3.1. For this, the input power is kept the same, but the input frequency is swept slowly from a point before the natural frequency and then past it. The frequency sweep is linear. The harmonic response of the system, i.e. the induced lateral vibrations of the tip, are recorded at small increments. The harmonic response of a laser cut 100-micron aluminum sample can be seen below:

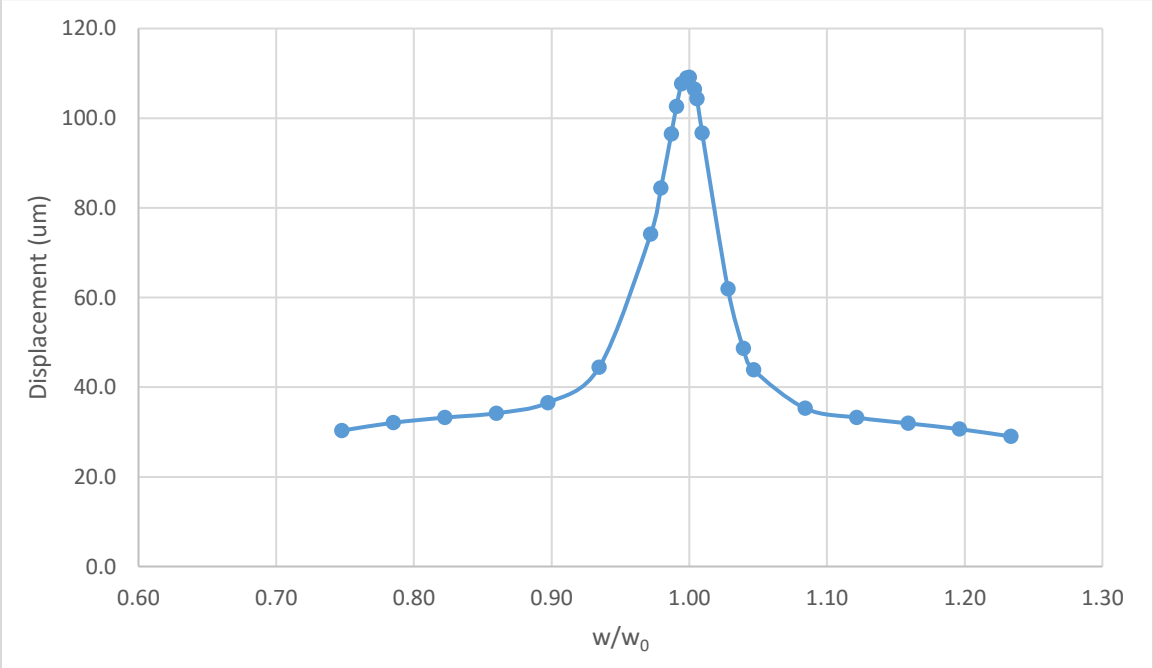

Figure 82. Typical harmonic response of 100-micron tall aluminum bridge sample with a natural frequency of 2381 Hz

Similarly, the typical response of a 150-micron tall brass bridge sample is shown below:

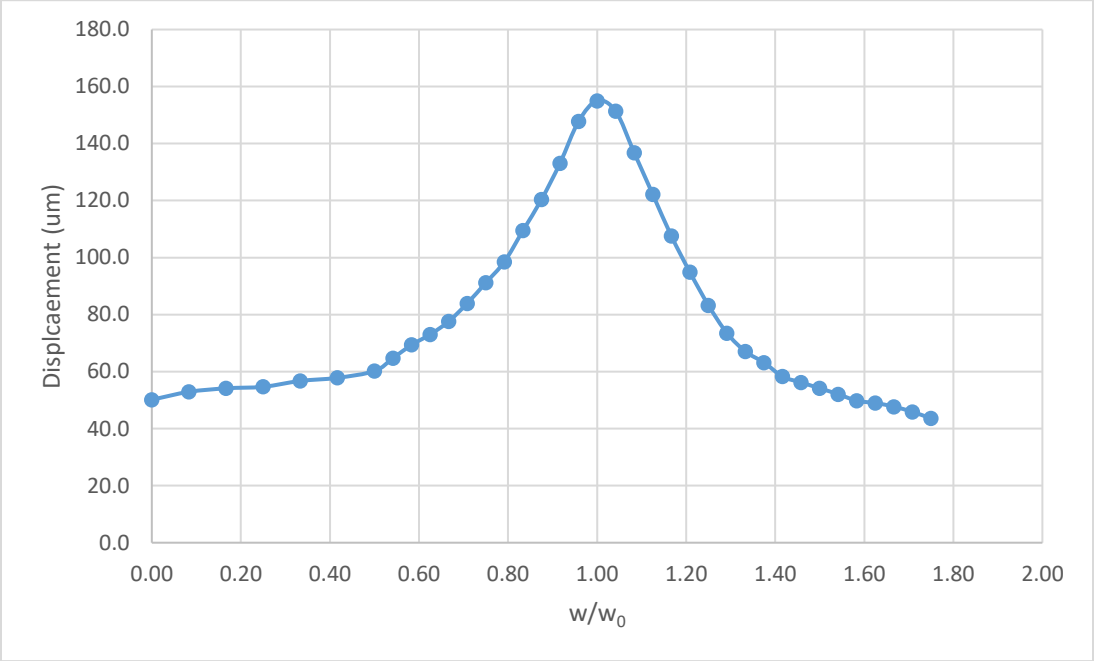

Figure 83. Typical harmonic response of a 150-micron tall brass bridge sample with a natural frequency of 2437 Hz

From the previous two figures, we can observe a noticeably greater amplitude of displacement when the frequency of input oscillations matches the micro-cantilever's natural frequency than it does at other frequencies. This shows that the system does in fact achieve higher magnitude of tip displacement at its natural frequency. The harmonic response of the system is about the same for each configuration. The variations observed in the harmonic response in terms of slope of the curve are due to the damping coefficient (taller bridge flexes more and is less rigid). A lower damping coefficient results in a sharper rise in the harmonic response, as seen in Fig. 88, and results in greater amplitude of displacement. Therefore, a lower damping coefficient is desired in this project. Factors that can contribute to damping in the system are, the hardness of the adhesive holding the 'fixed' end of the fiber (the collection portion), the actuator bridge flexing and absorbing some of the vibrations (remember it is only about 20 microns thick and very soft as a result), how off axis the fiber is relative to the actuator bridge, etc. The improvement in performance after switching from Loctite 495 to Master Bond EP17 (discussed in section 5.5.2.) was a result of lowered damping in the system.

6.3.2. Tip Displacement at Natural Frequency

After establishing that the system indeed has a higher amplitude of displacement at its natural frequency, the performance under different levels of power is evaluated. The input frequency is kept the same as the system's natural frequency and power through the actuator is gradually ramped up. The magnitude of tip displacement at every interval is recorded. As explained in section 6.1., this is a very important factor that determines how high of a resolution the final image will have. Therefore, a series of graphs are presented in this chapter to depict what kind of performance can be expected from this design in various configurations (all of the results presented in this section are from samples that have a micro-cantilever length of just under 2 mm). The input power is kept well below 1 W. The tip displacement response of a 100-micron tall aluminum bridge with a natural frequency of 2381 Hz and fiber-bridge distance of about 100 microns is shown below:

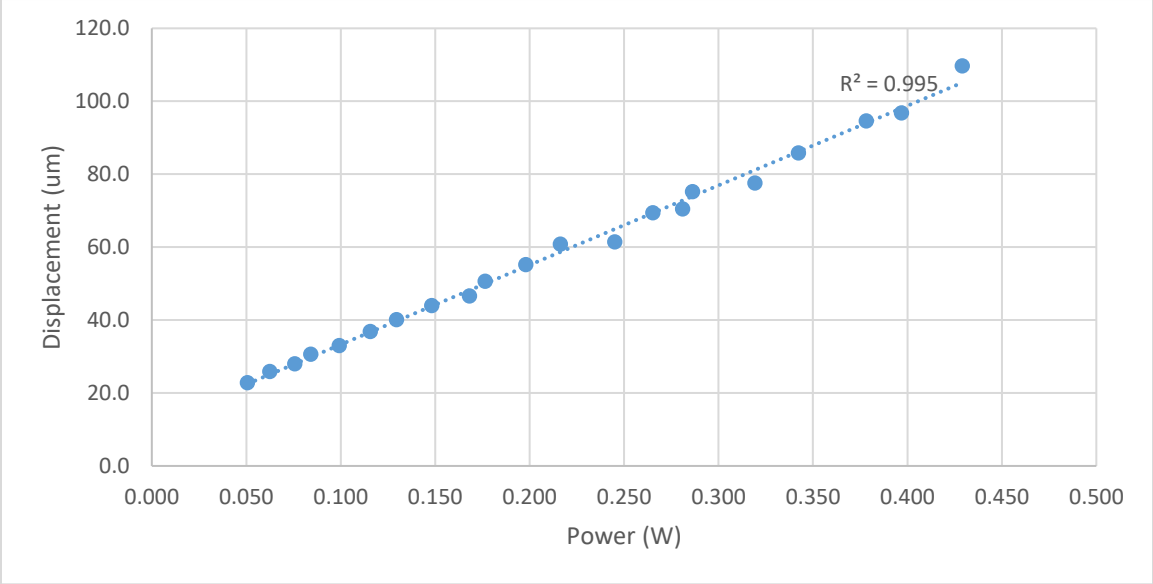

Figure 84. Tip displacement of a 100-micron tall aluminum sample

From section 3.1. and since coefficient of thermal expansion is linear, a taller actuator should result in a higher level of displacement; proportional to its increase in height. Therefore, the results from an aluminum bridge with the same configuration other than a taller aluminum bridge (150 microns, 2410 Hz) is presented below for comparison:

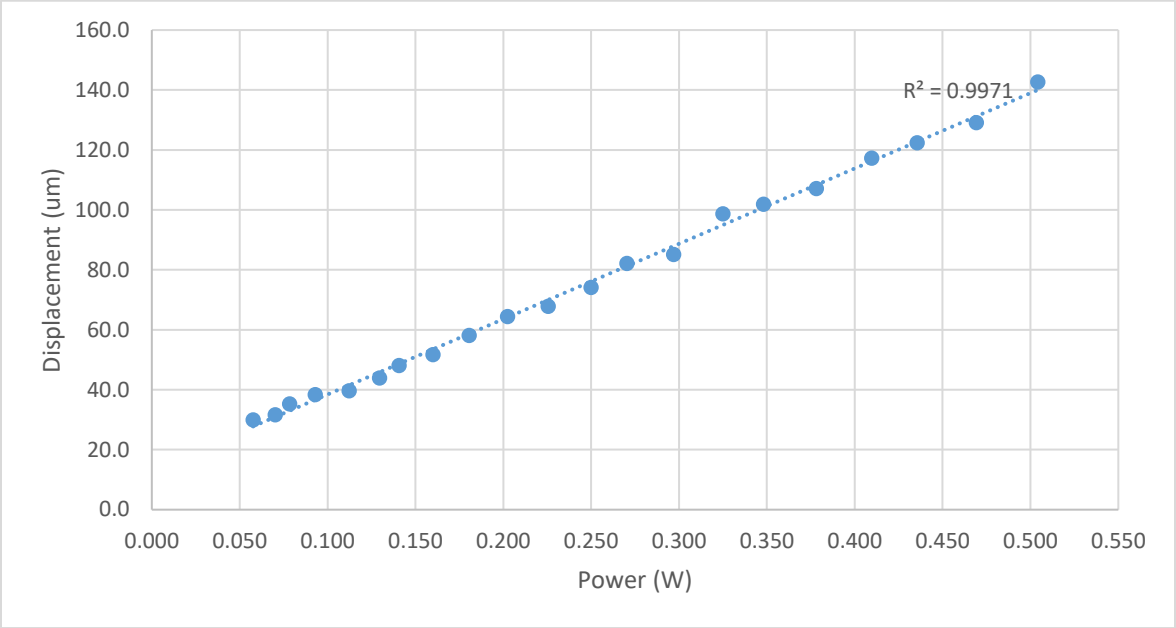

Figure 85. Tip displacement of a 150-micron tall aluminum sample

In theory a 50% increase in tip displacement has to be observed by increasing the height of the bridge from 100 microns to 150. However, this increase in bridge height has resulted in an approximate increase of about 23% in displacement. This can be due to many factors that would cause this deviation from the ideal case. A 150-micron bridge is approximately 40% more resistive than a 100-micron bridge because of its increased length and has more mass, therefore, a larger body of mass from a higher temperature has to be cooled down in the same time cycle. A 150-micron tall bridge would also be less structurally rigid than a shorter one and can flex and bend more reducing the performance.

As explained previously, aluminum is notoriously hard to work with both due to being dissimilar with copper and also being extremely soft in a 20-micron thin foil form factor. Therefore, many of the samples fabricated used brass as the bridge material. Brass has lower thermal conductivity and coefficient of linear expansion values but higher Young's modulus and resistivity. It is also less ductile than aluminum and a similar metal to copper which makes it much easier to work with. The graph below depicts the typical performance displayed by a 150-micron tall brass bridge samples:

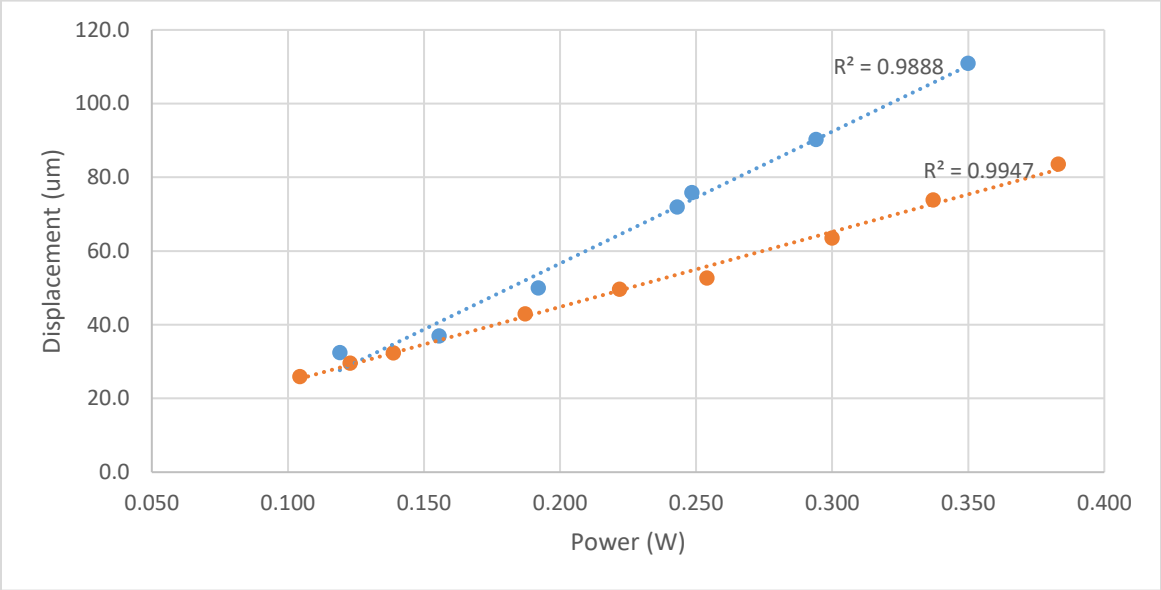

Figure 86. Tip displacement of two 150-micron tall brass bridge samples; blue graph is longer and has a natural frequency of 2466 Hz while the orange graph is shorter and has a natural frequency of 2614 Hz

As expected, the brass samples with their higher resistivity and lower thermal conductivity and linear expansion perform worse than their aluminum counterparts; the 150-mircon tall brass samples are on par with 100-micron tall aluminum samples. The increase in resonance frequency corresponds to only about 100 microns reduction in length. Even though, the shorter micro-cantilever should have a smaller amplitude of lateral vibration than the longer fiber, the effect should not be as pronounced as in Fig. 86. It is evident that a sample with a higher frequency has a significant decrease in performance. This is observed in many samples. This can be attributed to the shorter time cycle in which the actuator bridge has to cool down. This increased resonance frequency can cause a higher average temperature at steady state which would mean a lower cyclic temperature differential and less vertical oscillations by the actuator bridge.

These results mainly point to a heat dissipation issue. This is further reinforced by looking at the data from 200-micron tall brass bridge samples. These samples only provide a marginal improvement in performance compared to their 150-micron counterparts and after a certain point in input power, they not only start to plateau, but they actually regress proving they are not cooling fast enough. This phenomenon can also be seen in 150-micron tall brass samples with slightly higher resonance

frequencies. The graph below shows the response of a 150-micron tall bridge sample with a resonance frequency of 2840 (slightly shorter micro-cantilever) that has been placed closer to the actuator (about 50 microns distance):

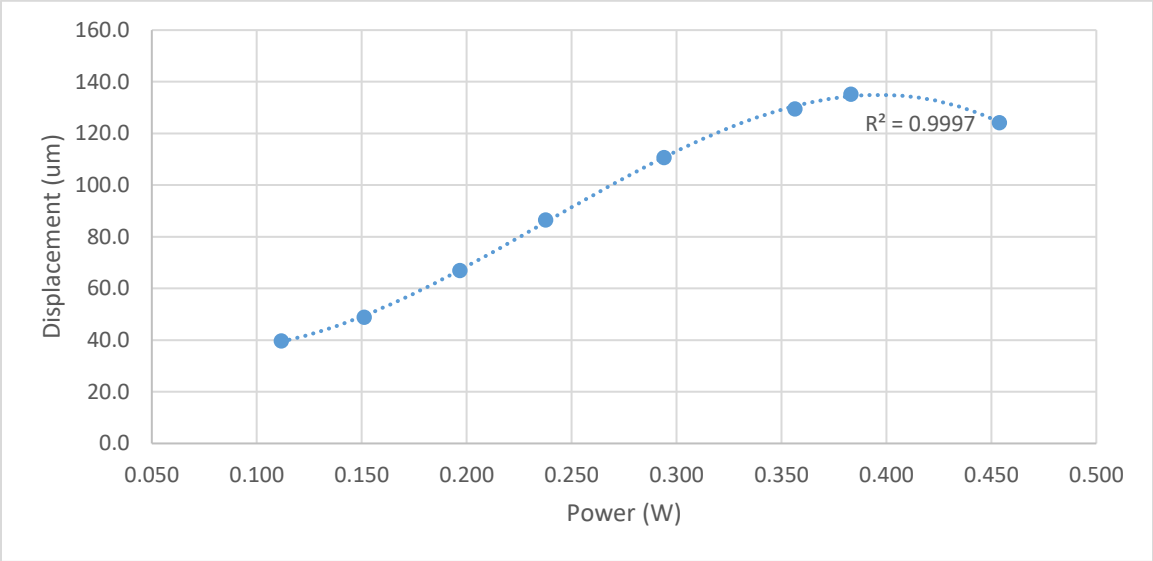

Figure 87. Harmonic response of a 150-micron tall brass bridge sample

As seen in the figure, the harmonic response of the system is fairly linear till about the 0.350 W mark and past that point it starts to plateau and regress. This is a clear evidence of bridge not cooling down sufficiently fast enough and thus having a higher initial temperature before the next cycle and consequently a lower temperature differential.

Nevertheless, there are many possible configurations in this design. In order to achieve a greater degree of tip displacement, a brass sample with 150-micron tall bridge sample was fabricated in which the collection portion of the fiber was tucked right up against the bridge in a perpendicular alignment so that there is essentially no gap between the base of the illumination fiber and the bridge. This particular sample had a resonance frequency of 2410 Hz and its response is shown in the below:

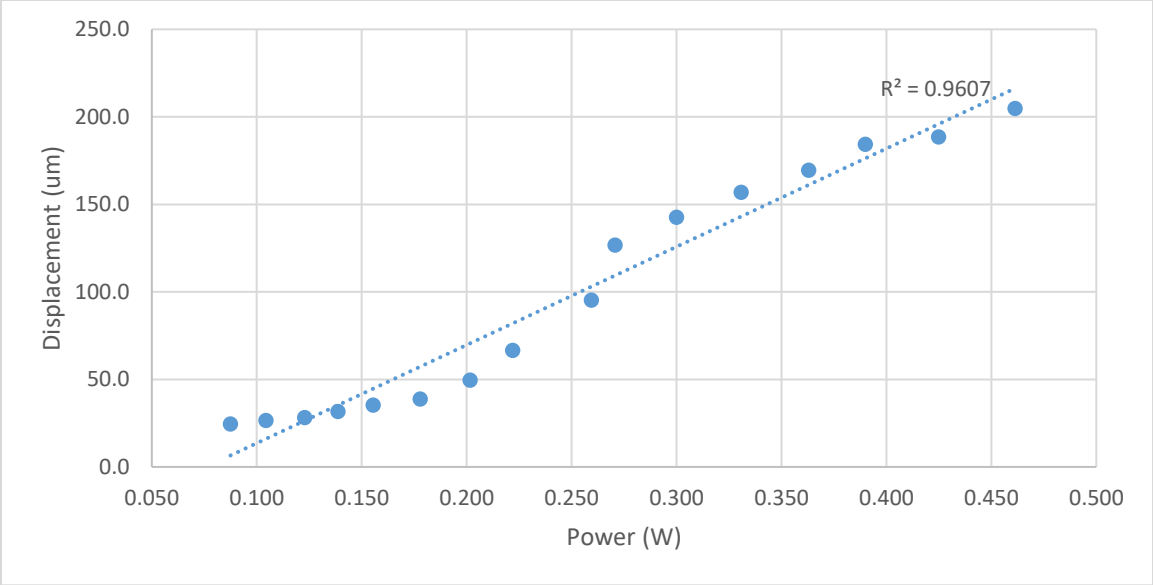

Figure 88. Harmonic response of a 150-micron tall brass bridge with no micro-cantilever gap to it

It can be observed that in this set up the tip displacement is greatly improved to just over 200 microns, achieving the required level of actuation for the project. A microscopic image of tip displacement is seen here:

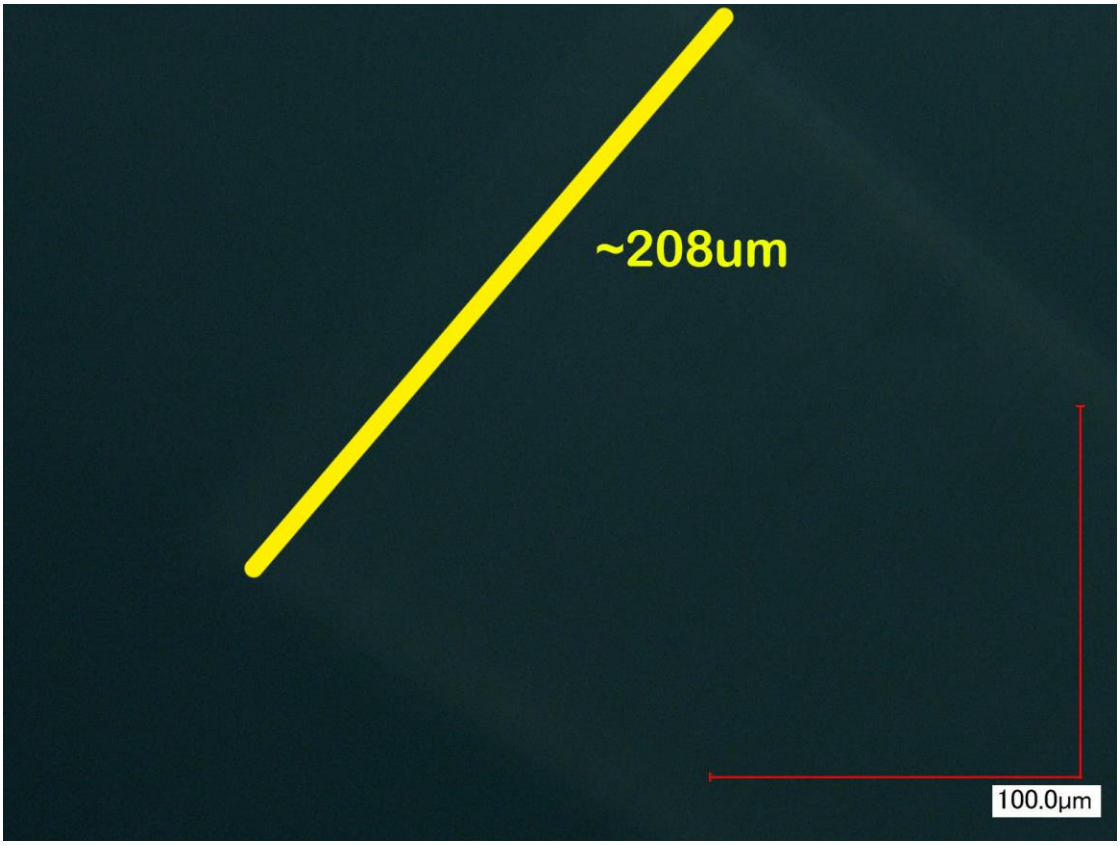

Figure 89. Tip displacement of the 2410 Hz brass sample at 0.461 W with an 8-degree adjustment

The tip displacement results in this section agreed with the findings in section 3 for the most part if the assumptions in the analytical part are taken into consideration; namely the conduction wires acting as perfect heat sinks with no temperature rise. In this iteration of prototypes, the actuation wires are in contact with the laser cut portion before being connected to the copper wires. Due to joining problems discussed in section 4.5.1., the laser cut portion is just soldered to the copper wires and while it is not as critical as when they were between the actuator wire and the copper wires (section 4.3.), it can still give off some residual heat during the 'off' states and hamper the performance somewhat. This multi-stage design, as well as use of solder and the parts well, just not acting like perfect heat sinks in real life, do contribute to lower than expected performance. Furthermore, in the simulations, the collection portion of the fiber (i.e. the backend), was assumed to be completely rigid. However, in real life, most things are not rigid, especially in strips and films only a few microns thick and they do bend and flex under the vibrational forces. This was experienced firsthand when the adhesive holding the micro-cantilever was replaced with EP17; but even then EP17 is not completely rigid

and while it is hard, it is just hard compared to polymers and plastics and other porous structures and does not compare to most metals or crystalline minerals. Nevertheless, even with all of these limitations, the response of the system followed the findings in section 3 in terms of natural frequency and expected behavior and trends. The tip displacement increased linearly with increased cyclic thermal base excitation and longer bridges resulted in larger magnitudes of displacement and the bridge acted like a low-quality resonator, as predicted. In addition, as expected, decreasing the distance of the bridge and the micro-cantilever (denoted by l in section 3.1. and seen in Fig. 23) resulted in larger amplitudes. The coefficients of determination of all the results presented in this section also reaffirm that the level of performance is a linear function of input power, at least till heat dissipation becomes an issue.

Therefore, it can be concluded that this design has the potential to match the requirements set for this project in terms of tip displacement and resonance frequency and it should be possible to increase the amount of displacement by optimizing the design parameters and addressing the issues with heat dissipation and structural rigidity.

6.3.3. Maintaining Average Power but Lower Duty Cycle

In the previous section it was observed that the actuation bridge is not cooling down as fast as it should during the ‘off’ time cycles and the average body temperature is drifting upwards with higher levels of input power resulting in reduced overall performance.

The cyclic input to all the previous samples was a square signal (i.e. 50% duty cycle). In order to try to resolve this issue with minimal modifications to the system, the average power was kept the same, but the duty cycle was reduced. This was achieved by reducing the duty cycle but increasing the amplitude of the signal high enough that the area underneath the now narrower signal is the same as the ‘on’ cycle of the old square signal. Note that while this would result in the same average power, this will still increase the instantaneous power, and this should be balanced and limited to an acceptable level to prevent damaging the thin 20-micron metal wire. Nevertheless, this reduced duty cycle gives the actuation bridge more time per cycle to cool down. This should counteract some of the negative effects of insufficient cooling. A 150-micron tall

brass bridge sample with a resonance frequency of 2407 Hz was first run with a 50% duty cycle as control and then at 20%. The results are shown below:

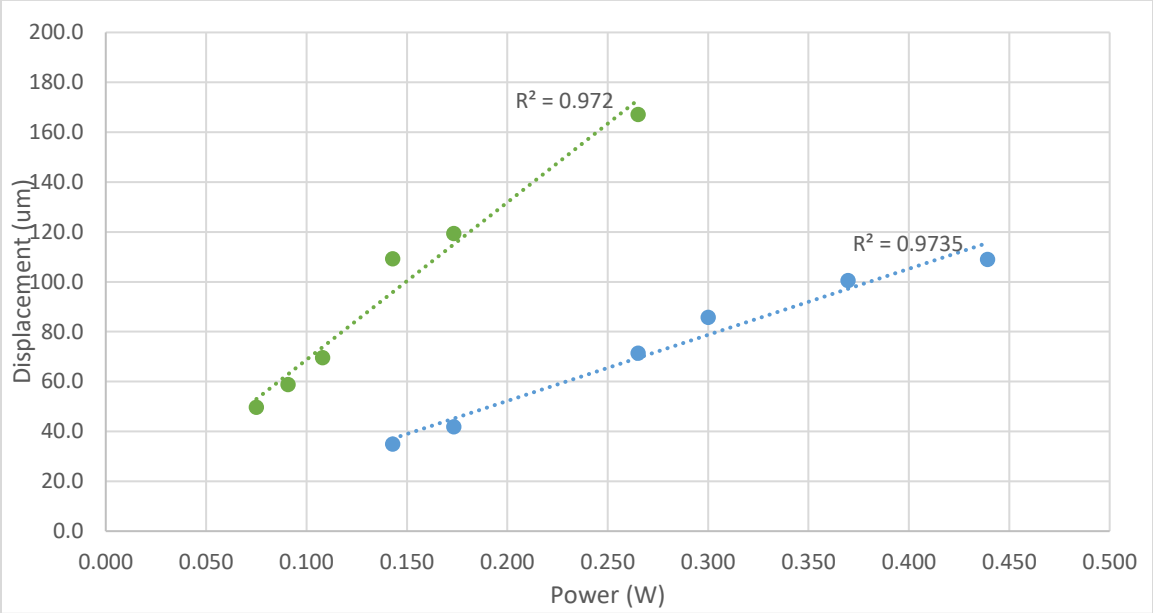

Figure 90. Tip displacement of a 150-micron brass sample under two different duty cycles; green, 20% duty cycle, blue, 50% duty cycle

From the graph, it can be seen that by decreasing the duty cycle to 20% the performance has been more than doubled for the same average power. This further reinforces the idea that heat dissipation is an issue that needs to be addressed. Nevertheless, this method provides a solution to the problem that would help the system reach the set displacement targets. Lowering the duty cycle has improved the performance across the board for every single sample tested with it. However, the amount of improvement has not been uniform across different samples and the improvements have been anywhere from 20% to more than 100% in some cases.

This method can change a sample's performance from insufficient to usable at a certain power level. This is especially evident in samples that have a relatively higher resonance frequency. The sample below is a 150-micron tall brass prototype with a resonance frequency of 2839 Hz under a low power of just 0.075 W:

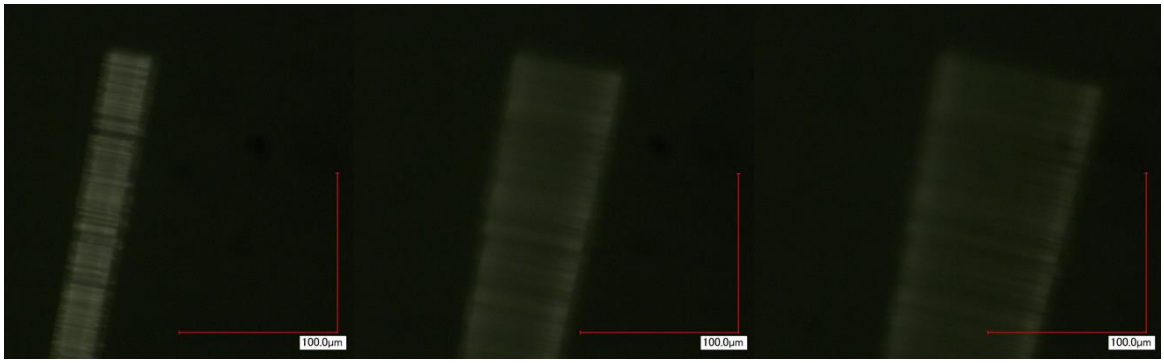

Figure 91. Tip displacement of the same sample with the same power; (a) 50% duty cycle (b) 20% duty cycle (c) 10% duty cycle

The results are plotted in the following bar graph:

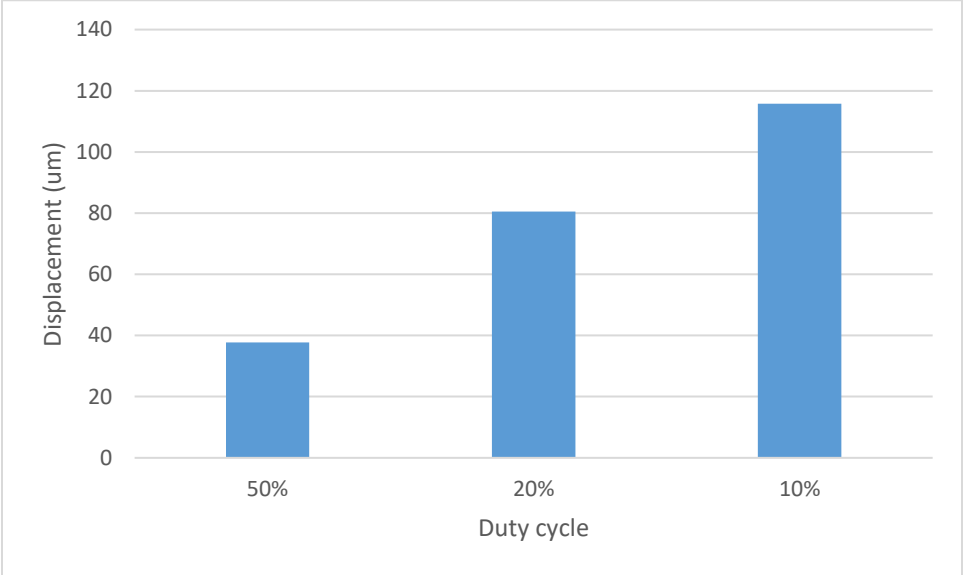

Figure 92. Improvements in performance because of lowered duty cycle

This shows that this is an effective method for increasing the performance of the system. The performance increase is because during the ‘off’ states, the bridge has more time to cool down and so, it drops down to a lower value than it would have otherwise which results in a lower average body temperature and a higher bridge temperature differential. Lowering the duty cycle even further should in theory improve the results but, in practice, because of the massive increase in instantaneous power through the actuator wire, it can damage it. Therefore, in samples with lowered duty cycles, the cost of increased performance has to be balanced against the need for longevity and reliability.

6.3.4. Passing Light Through the Fiber

After achieving satisfactory level of displacement at reasonable frequencies, the next testing phase began. Before this stage, all optical fibers were just tested as essentially mechanical silica beams with no light passing through them. Since, the fibers are custom made, it was not clear how well, they react and hold up to being vibrated; especially when they are pulled to 12 microns in diameter. These tests took place at BCCA. This was important because after many hours of vibrating the optical fibers, some sort of what appeared to be damage to the cladding of the fibers would be seen:

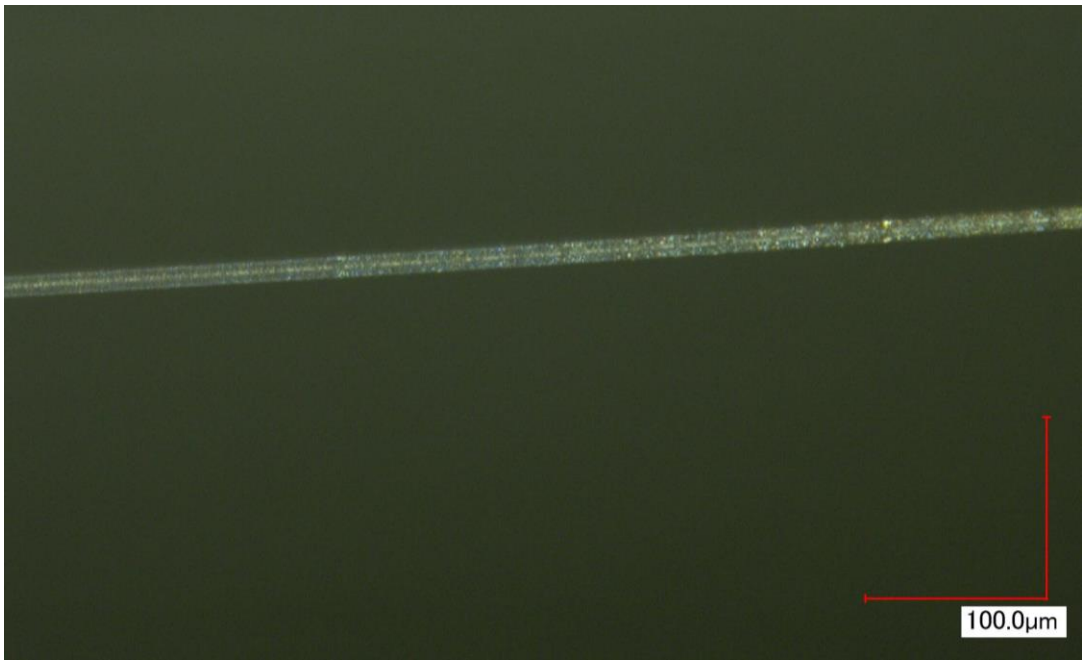

Figure 93. Damage observed on some fibers after hours of vibrations

For the illumination fiber, a 3-micron optical core was used in conjunction with blue laser light (442 nm). For this test a scanning slit beam profiler [54] was used to measure the light power output of the sample, before being vibrated, during vibrations and after some time and see whether the tiny fiber holds up. After testing multiple samples, no significant loss of light power was observed and therefore, it was concluded that the damage is merely cosmetic. The next stage would be to try and collect the reflected lights back.

6.4. Further Observations

6.4.1. Size of Solder

As mentioned in this section, since, none of the joining methods identified in section 5.5.1. were purchased, the laser cut strips were soldered to the copper conduction wires. While not as impactful as when they were in between the resistive heating wire and the copper traces, this still has to have some impact on the performance and give off some heat during the off cycles, reducing the performance. As it was seen from the results in this chapter, heat conduction is an issue and any factor that can contribute to it is obviously undesired.

For this reason, the size of solder spots was tried to be as small as possible (ideally a few microns in diameter) and a review of the test results and comparing them to the physical characteristics of the samples showed that, samples with larger and messier solder spots had a somewhat dampened response. This further reinforces the idea that solder should not be used as a joining method and should just be a temporary stop gap solution for the current batch of samples.

6.4.2. Use of Thermal Pastes

In an attempt to mitigate some of the heat dissipation issues and to add another path of heat conduction to the design, some samples were made with an extra metal layer underneath it and various thermal pastes were used to isolate the two metal layers from each other electrically. However, they did not appear to have a significant effect on the performance of the system:

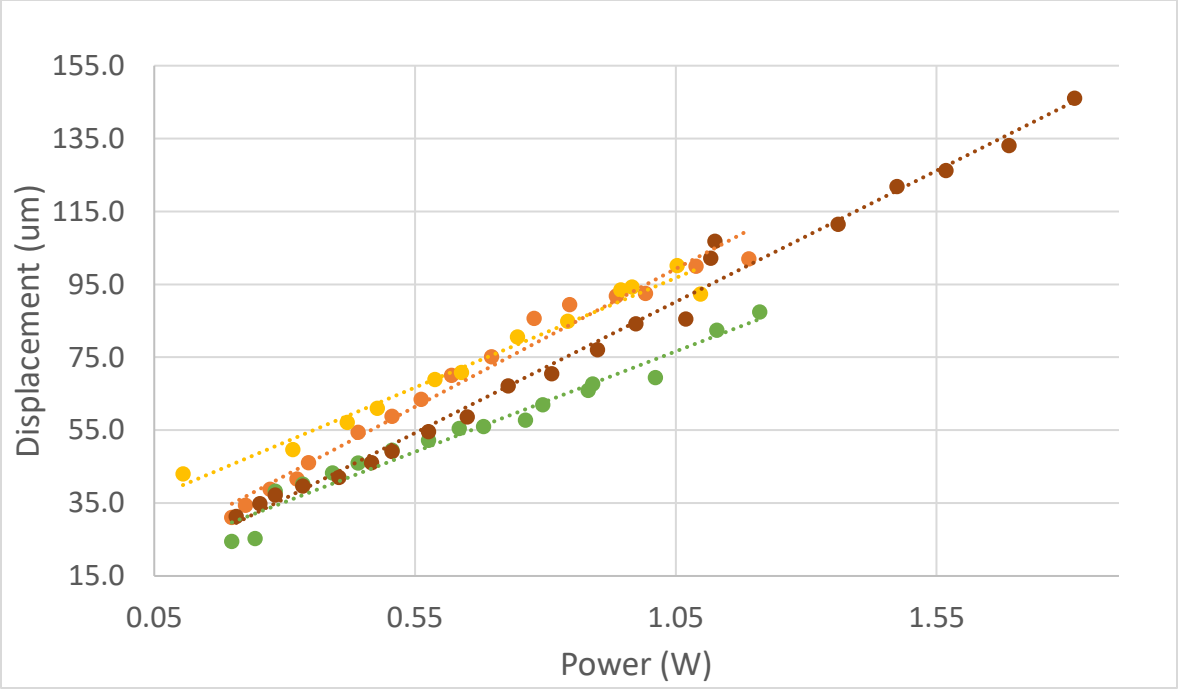

Figure 94. Four similar aluminum samples 4 different thermal paste mixes; yellow is a carbon-based CPU thermal paste, orange is a custom mix of diamond dust and epoxy, brown is a thermal adhesive and green is another brand of thermal adhesive

The results appear to suggest that the choice of materials in immediate contact with the bridge seem to have the largest effect on performance of the fiber and the extra heatsink with the thermal paste contact not only does not improve the performance but might act like a heat capacitor like solder and reduce the vibrations.

6.4.3. Rigidity of the Fixture

The choice of adhesive, used to fix the backend of the system, proved to be a crucial one and using an adhesive that maintained its hardness at elevated temperatures increased the minimal and insufficient vibrations to the target levels. However, after approximately 2-3 hours of continuous operation, there is a noticeable drop in performance. This was narrowed down to micro-cracks forming in the EP17 adhesive due to the induced vibrations:

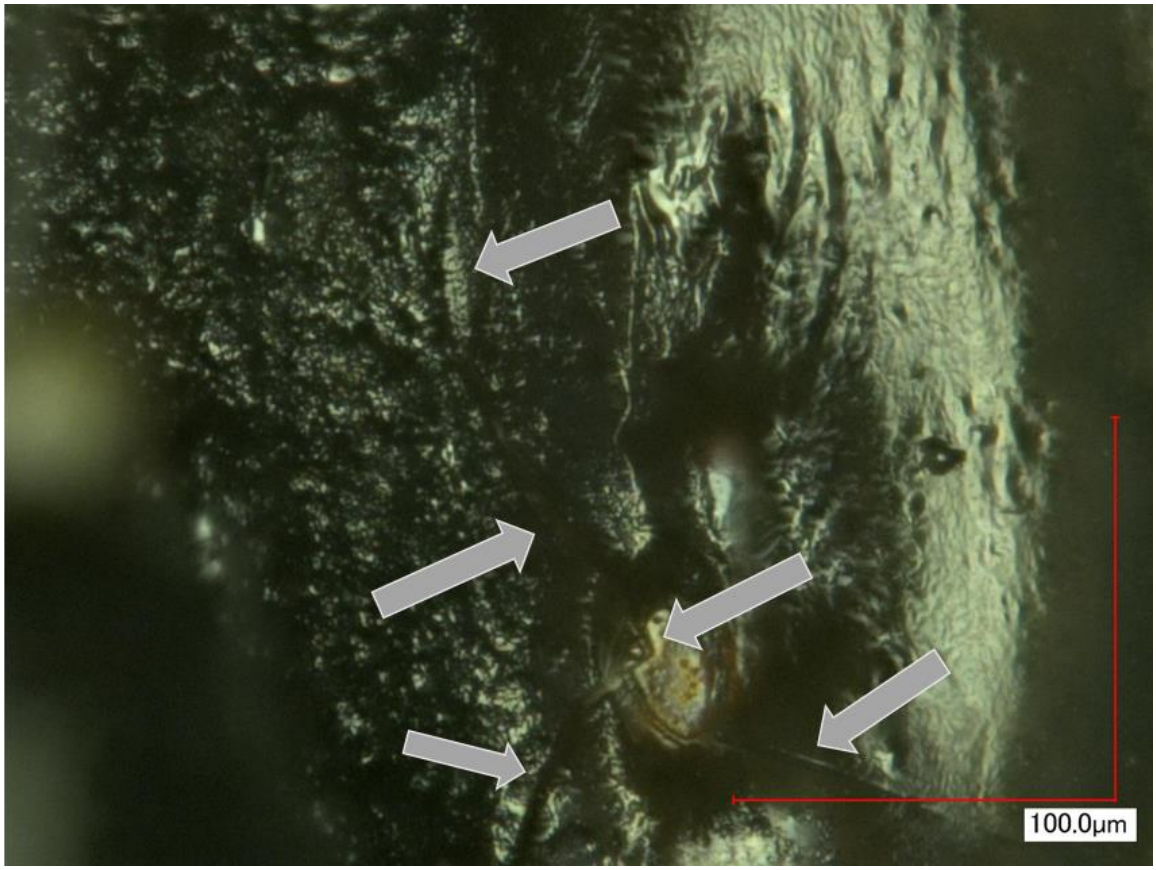

Figure 95. The micro-cracks formed in the EP17 after hours of operation

These micro-cracks, only 1-3 microns wide, compromise the structural integrity of the adhesive and make it so that it can move and play under the induced vibrations. When these cracks form, the back portion of the fiber, i.e. the “fixed” end, is no longer fixed in place which massively increases the damping coefficient of the system and torpedoes the magnitude of tip displacement, effectively destroying that particular prototype. This is something that needs to be addressed if the future prototypes are no longer going to be disposable or need to work for more than a few hours.

6.5. Summary

This chapter covers objective 3 of the study and sets out to assess the performance of the thermally actuated micro-cantilever design and evaluate the magnitude of lateral tip displacement achievable at a sufficiently high enough resonance frequency in order to meet the performance goals set for the project in section 5.1. To validate the proposed designs through experimentation, the harmonic response that can be expected of the prototypes is presented. The harmonic response of the prototypes

shows that even with the materials and layers being only a couple dozen microns, the overall structure is rigid enough to have a low enough damping coefficient to go into resonance. The harmonic response also displays a greater magnitude of tip displacement at resonance as predicted.

The magnitude of tip displacement at various power levels for different design configurations is presented next. The findings show that the design is capable of getting to the target displacement values and the behaviour of the prototypes largely agree with the theoretical findings in section 3. However, it is also evident that there are some heat dissipation issues in the current iteration of samples and this can cause an increased average body temperature and lowered performance. Some of it can be attributed to the use of solder. Using a lower than 50% duty cycle is proposed as a potential fix to the heat dissipation issue and its effectiveness is documented.

These findings show that the proposed design is indeed small enough to match the ultra-thin distal tip size while having a level of performance that is at least sufficient. Furthermore, it identifies a couple of problem areas that can improve performance if addressed. Therefore, these results show that while the general response or at least the trends can be predicted by the analytical models developed, with the real life models these limitations and non-linearities need to be considered and the height and location of the bridge and length of the optical fiber need to be balanced and optimized to maximize the displacement and frequency numbers.

Chapter 7. Conclusion and Future Work

7.1. Summary and Conclusion

Endoscopes lead the way in minimally-invasive diagnosis and treatment of many conditions and help medical professionals carry out these procedures with minimal risk and discomfort to patients. However, they are limited by their distal tip size and many narrow passages inside of the body bar them from getting to certain organs and areas. The lungs, with their many narrow airways, are a notable example of this problem. Even the smallest endoscopes at the moment are incapable of going past the bronchi. A novel approach based on exciting a dual clad single mode micro-cantilever optical fiber at a location close to its base to resonance using a conductive wire is proposed and studied in this paper in order to design a system that is small enough that can be used to image most areas of the lung.

Three objectives are set for this study. The first objective tries to study the feasibility of the suggested method by first analytically modeling it and then comparing the mathematical models to large scale prototypes fabricated in the lab that aim to mimic such system. The second objective is to design a system that implements this proposal in a form factor that is small enough to meet the sub 500-micron housing requirements. The third and final objective of the study is to evaluate the performance of this design in various configurations and verify the design meets the displacement requirements through experimentation.

To create an analytical model of the system, the continuous Euler-Bernoulli beam equation with the effect of surrounding fluid medium is formulated as a boundary value problem. The natural frequencies of the system and its harmonic response are expanded analytically. The obtained analytical solutions are used to draw conclusions on the response of the system and suggestions to optimize its performance are presented. In order to verify the idea in practice, a series of large scale models are fabricated using PCBs and their response to a periodic input with different frequencies are recorded. Comparison between the results of analytical formulation and experimental observations showcase the potential of suggested technique in resonance vibration of optical fibers. Though there is a mismatch between the amplitude of vibrations and the analytical models. This is attributed to the heavy use of solder in the PCB prototypes as well as the

assumptions for the mathematical models, namely the homogenous temperature distribution along the length of the actuator, perfect electrical and thermal interface in between copper conduction wires and aluminum actuation wire, the fixed end of the dual clad fiber being completely rigid, and the body of copper having a steady temperature during the cycles. These topics are covered in chapter 3 and 4.

Chapter 5 covers the design and implementation of this novel proposal. The primary and non-negotiable goal of this study is to have an imaging set-up that fits inside of a sub 500-micron housing. In order to achieve this feat, first a material selection process based on thermal conductivity, coefficient of thermal expansion, Young's modulus and electrical resistivity is performed. This selection process narrows down the list of materials to aluminum and its 6000 series alloys as well as copper alloys like brass for actuation wire and copper or silver as suitable materials for conduction. The factors affecting the resonance frequency of the system, mainly the dimensions of the fiber and the actuation bridge's position relative to it are outlined. A graph relaying this information is also presented. The design decisions that have gone into the driver circuit used to pass a square wave signal through the resistive wire are explained. The study then explains the problems related to joining copper and aluminum and picks out ultrasonic (single-point tab bonding) and capacitive discharge micro spot welding as potential solutions. Two temperature resistant hard adhesives are picked out for the project. A method of making the resistance actuation wire out of a single piece of thin foil is introduced and shown to work. Finally, a method to put all the finding together to fabricate a thermally actuated system that is small enough to theatrically fit inside of a 300-micron tube is presented (though, only 500-micron diameter samples were produced). The observations prove that the design is easily capable of meeting the size requirements. These dimensions make it possibly the smallest active fiber endoscope head.

Chapter 6 sets out to experimentally assess the amplitude of tip displacement of the prototypes fabricated with the method proposed at reasonably high frequencies. The harmonic response of the system is analyzed, and the results show that resonance is indeed responsible for the large vibrations of the fiber. In addition, the findings reaffirm the analytical results from chapter 3. Next, the response of the system in several configurations to various levels of power is presented. The findings are again in line with the theoretical findings in chapter 4 for the most part but heat dissipation seems to be an

issue that is introducing some non-linearities to the response of the systems. Reducing the duty cycle to less than 50% while maintaining the average power is proposed and it is shown to be an effective way of counteracting some of the adverse effects of improper cooling. All in all, the designs seem to be capable of reaching 100-200 microns of tip displacement at frequencies of about 2.5 kHz. This amount of tip displacement is sufficiently high enough to potentially produce an image with an acceptable (though not ideal) resolution.

The outer diameter of the package and the magnitude of tip displacement and resonance frequency were set as benchmarks for determining the success of this project. The results from chapter 5 show that the design can certainly meet the size requirements, producing samples that have a distal tip diameter of 500 microns (theoretically even as small as 300 microns) and a distal rigid length of 3-5 mm; well below what is available at the moment. The findings in chapter 6 show that despite some of the problems outlined, the prototypes are still capable of achieving over 200 microns of tip displacement at about 2.5 kHz, enough to clear the requirements in those categories. Although, these number should be ideally higher for higher quality images, they are still sufficient enough to move the project forward. Nevertheless, a few problem areas are also identified that should significantly improve the performance when they are resolved. Chapter 3, matched the results for the most part. The results presented in chapter 3 can be interpreted as the ideal case and can represent the ceiling and a target to work towards. The results show that there is still a lot of headroom in the design for improvements in terms of achieving greater amplitudes of displacement at lower power levels. The project set out to create an endoscope tip enclosure small enough that can be used inside of the lung and from the observations in chapters 4, 5, and 6 it can be concluded that it has achieved the goals set and the current design can at the very least act as the foundation for future iterations.

7.2. Future Considerations

7.2.1. Shape and Size Optimization

In the analytical models presented in chapter 3, the temperature of the small actuation bridge is assumed to uniform during the thermal cycles. However, that is not the case in the real-world samples and the center of the bridge is going to have a higher

temperature than its legs because it's the farthest point from the 'heat sinks'. Any future simulations and analytical models need to consider this temperature gradient to be able to better predict and optimise the response of the system. Furthermore, more studies on the shape and size of bridge as well as its length and other factors like the shape of the laser cut out thin foil are required in order to be able to design a system that can better manage the heat and reduce the hot spots by increasing their cross-sectional area. For example, the temperature of the bridge can be kept more uniform by increasing its cross-sectional length at the middle portion. Eliminating the hot spots should massively increase the performance.

7.2.2. Welding Contacts

Solder as a way of joining the conduction wires to the actuation bridge or the thin foil was consistently identified as a source of problem because of its high specific heat capacity and relatively low thermal conductivity which cause it to act like a heat capacitor. Any future design iterations need to eliminate the use of solder either by utilizing the methods presented in section 5.5.1. or by finding new bonding solutions.

7.2.3. Hard Brackets

The importance of having a rigid back end is crucial to a design that is based on Euler-Bernoulli fixed-free beam equations. Any vibrations and play on the side of the collection fiber should seriously reduce the performance of the system. This was experienced first hand when the adhesive used in the design changed from Loctite 495 to Master Bond EP17. However, while EP17 is hard, it is only hard for plastics and polymers. Ways of improving the structural rigidity of the design should be explored in future designs in order to improve the performance.

7.2.4. Repeatability and reliability

Chapter 6 highlighted the fact that fabricating these micro-scale prototypes by hand results in a lot of variations and the results from one sample can be noticeably different from another sample with seemingly the same configuration. Therefore, ways to improve repeatability and reliability of the design should take center stage as the project moves forward.

References

[1] "Upper endoscopy," Mayo Clinic, [Online]. Available: https://www.mayoclinic.org/tests-procedures/endoscopy/basics/definition/prc-20020363. [Accessed January 2018].

[2] G. Ginsberg, M. Kochman, I. Norton and C. Gostout, Clinical Gastrointestinal Endoscopy, 2nd edition, Elsevier, 2014.

[3] S. Roberts and R. Thornington, "Paediatric bronchoscopy," *Continuing Education in Anaesthesia, Critical Care & Pain,* vol. 5, no. 2, pp. 41-44, 2005.

[4] B. Bradley, H. Branley, J. Egan, M. Greaves, D. Hansell, N. Harrison, N. Hirani, F. Lake, A. Miller, W. Wallace, A. Wells, M. Whyte and M. Wilsher, "Interstitial lung disease guideline," *the British Thoracic Society in collaboration with Thoracic Society of Australia and New Zealand and the Irish Thoracic Society,* Vols. 1-58, 2008.

[5] Hellerhoff, "Lung biopsy guided by computer tomography: Lung cancer," 8 November 2010. [Online]. Available: https://upload.wikimedia.org/wikipedia/commons/5/50/Biopsie_Lunge_Computertomographie_BC.png. [Accessed January 2018].

[6] "Lung Cancer Statistics," Canadian Cancer Society, 2017. [Online]. Available: http://www.cancer.ca/en/cancer-information/cancer-type/lung/statistics/?region=on. [Accessed January 2018].

[7] E. Seibel, "1-mm catheterscope," in *Optical Fibers and Sensors for Medical Diagnostics and Treatment Applications VIII*, Gannot, Israel, 2008.

[8] M. Komeili and C. Menon, "Modeling the dynamic response of a micro-cantilever excited at its base by an arbitrary thermal input using Laplace transformation," *Applied Mathematical Modeling,* vol. 43, pp. 481-497, 2017.

[9] M. Komeili and C. Menon, "Modelling a micro-cantilever vibrating in vacuum, gas or liquid under thermal base excitation," *Mechanics Research Communications,* vol. 73, pp. 39-46, April 2016.

[10] M. Komeili and C. Menon, "Resonance vibration of a thermally-actuated optical fiber with arbitrary periodic excitation: Analysis and optimization," *International Journal of Mechanical Sciences,* vol. 123, pp. 287-296, April 2017.

[11] M. Komeili and C. Menon, "Analysis and Design of Thermally Actuated Micro-Cantilevers for High Frequency Vibrations Using Finite Element Method," *World Journal of Mechanics,* vol. 06, no. 3, pp. 94-107, 2016.

[12] M. Komeili and C. Menon, "Robust Design of Thermally Actuated Micro-Cantilever Using Numerical Simulations," *International Journal of Simulation Modelling ,* vol. 15, no. 3, pp. 409-422, 2016.

[13] "Endoscopy," Cancer Research UK, 2018. [Online]. Available: http://www.cancerresearchuk.org/about-cancer/cancer-in-general/tests/endoscopy.

[14] "CCD versus CMOS," TELEDYNE DALSA, [Online]. Available: http://www.teledynedalsa.com/imaging/knowledge-center/appnotes/ccd-vs-cmos/. [Accessed January 2018].

[15] E. Seibel, R. Johnston and D. G. Melville, "A full-color scanning fiber endoscope," in *Optical Fiber and Sensors for Medical Diagnostics and Treatment Applications VI*, 2006.

[16] E. Seibel, "Novel approaches in optical imaging and visualization of early cancer screening , diagnosis and treatment," in *Frontiers in Optics/Laser Science XXIII*, 2007.

[17] L. Kinsler, A. Frey, A. Coppens and J. Sanders, Fundamentals of Acoustics, 4th edition, Wiley, 1999.

[18] C. Lee, C. Engelbrecht, T. Soper, F. Helmchen and E. Seibel, "Scanning fiber endoscopy with highly flexible, 1 mm catheterscopes for wide-field, full-color imaging," *Journal of Biophotonics,* vol. 3, pp. 385-407, June 2010.

[19] Q. Smithwick, P. G. Reinhall, J. Vagners and E. Seibel, "A nonlienar state-space model of a resonating single fiber scanner for tracking control: theory and experiment," *Journal of Dynamic Systeems, Measurement, and Control,* vol. 126(1), p. 88, 2004.

[20] J. Maloney, "Large-force electrothermal linear micromotors," *Journal of Micromechanics and Microengineering,* vol. 14, no. 2, pp. 226-234, 2004.

[21] B. Barazani, S. Warnat and T. Hubbard, "Simulation and optical measurement of MEMS thermal actuator sub-micron displacements in air and water," in *IEEE 28th Canadian Conference on Electrical and Computer Engineering*, 2015.

[22] M. J. Sinclair, "A high force low area actuator," in *International Society Conference on Thermal Phenomena* , 2000.

[23] K. Kwack and K. K. Chun, "Very high displacement to voltage ratio MEMS thermal actuator," in *IEEE Sensors*, 2015.

[24] J. M. Maloney, "Large-force electrothermal linear micromotors," *Journal of Micromechanics and Microengineering,* vol. 14, no. 2, pp. 226-234, 2004.

[25] N. Suma, V. S. Nagaraja, S. L. Pinjare, K. N. Neethu and K. M. Sudharshan, "Design and characterization of MEMS thermal actuator," in *International Conference on Devices, Circuits and Systems*, 2012.

[26] B. Bschaden, T. Hubbard and M. Kujath, "Measurement of MEMS thermal actuator time constant using image blur," *Journal of Micromechanics and Microengineering,* vol. 21, no. 4, p. 12, 2011.

[27] D. J. Bell, T. J. Lu, N. A. Fleck and S. M. Spearing, "MEMS actuators and sensors: observations on their performance and selection purpose," *Journal of Micromechanics and Microengineering,* vol. 15, no. 7, pp. 153-164, 2005.

[28] M. Komeili, A. Ahrabi and C. Menon, "Resonance vibration of an optical fiber micro-cantilever using electro-thermal actuation," *Journal of Mathematical Models in Engineering,* vol. 3, no. 1, pp. 1-16, 2017.

[29] F. Beer, R. J. Jr., J. DeWolf and D. Mazurek, Mechanics of Materials 7th edition, McGraw-Hill Education, 2014.

[30] W. Thomson and M. D. Dahleh, Theory of Vibrations with Applications (5th Edition), Pearson, 1997.

[31] N. Asmar, Partial Differential Equations with Fourier Series and Boundary Value Problems (3rd Edition), Dover Publications, 2016.

[32] J. E. Sader, "Frequency response of cantilever beams immersed in viscous fluids with applications to the atomic force microscope," *Journal of Applied Physics,* vol. 84, no. 1, pp. 64-76, 1998.

[33] E. Rosenhead, Laminar Boundary Layers, Oxford University Press, 1963.

[34] K. Ogata, Modern Control Engineering (5th Edition), Pearson, 2009.

[35] A. Rahafrooz and S. Pourkamali, "High-Frequency Thermally Actuated Electromechanical Resonators With Piezoresistive Readout," *IEEE Transactions on Electron Devices,* vol. 58, no. 4, pp. 1205-1214, 2011.

[36] M. P. Norton and D. G. Karczub, Fundamentals of Noise and Vibration Analysis for Engineers, Cambridge University Press, 2003.

[37] N. Lobontiu, Dynamics of Microelectromechanical Systems, Springer, 2007.

[38] W. Thomson, Theory of Vibration with Applications, CRC Press, 1996.

[39] "Arduino Uno Rev3," Arduino, [Online]. Available: https://store.arduino.cc/usa/arduino-uno-rev3.

[40] "LTspice," Linear Technology, 2017. [Online]. Available: http://www.linear.com/solutions/ltspice.

[41] M. F. Ashby, Materials Selection in Mechanical Design, 4th Edition, Butterworth-Heinemann, 2010.

[42] K. G. Budinski and M. K. Budinski, Engineering Materials: Properties and Selection, 9th Edition, Pearson, 2009.

[43] "Granta CES Selector," Granta Material Intelligence, 2016. [Online]. Available: https://www.grantadesign.com/products/ces/.

[44] "Basic Linear Power Supply Circuits Design," CircuitLib Electronic Circuits, [Online]. Available: http://www.circuitlib.com/index.php/lessons/91-basic-linear-power-supply-circuits-design.

[45] "Power Resistor," ResistorGuide, [Online]. Available: http://www.resistorguide.com/power-resistor/.

[46] "Single-point tab bonding tools," SPT, small precision tools, [Online]. Available: http://www.smallprecisiontools.com/products-and-solutions/chip-bonding-tools/wedge-bonding-tools/single-point-tab-bonding-tools/single-point-tab-bonding-tools-introduction/?oid=738&lang=en.

[47] "CD Resistance Welding," Sunstone Welders, [Online]. Available: https://sunstonewelders.com/cd-welding/.

[48] "LOCTITE 495," Henkel, [Online]. Available: http://na.henkel-adhesives.com/product-search-1554.htm?nodeid=8797712875521.

[49] E. M. Petrie, Handbook of Adhesives and Sealants, McGraw-Hill Education, 2006.

[50] "EP17HTND-CCM Product Information," Master Bond, [Online]. Available: https://www.masterbond.com/tds/ep17htnd-ccm.

[51] "UV25 Product Information," Master Bond, [Online]. Available: https://www.masterbond.com/tds/uv25.

[52] "Laser Micromachining," 4D Labs, [Online]. Available: https://users.4dlabs.ca/tools/lasercutter.html.

[53] "IPG Photonics' IX-280-ML," IPG Photonics', [Online]. Available: http://www.ipgphotonics.com/de/289/Widget/IX-280-ML+Datasheet.pdf.

[54] "Scanning Slit Beam Profilers," DataRay Inc., [Online]. Available: https://www.dataray.com/scanning-slit-beam-profilers.html.

Appendix

Packaged Distal Tip

This section is a continuation of subsection 5.7. and aims to showcase the work done by Yasong Li to package and secure the proposed device using a series of PMMA collars while following the guidelines set in chapter 5.

The semi-circle piece is meant to create a flat surface/platform for the metal thin foil cut-out. The collars are meant to keep everything in place. The pieces are then glued together using EP17. Once inside, more EP17 is injected to the tube and cured in order to fill out any gaps between the components and also stick the inserted components to the inside of the tube. Multiple collars are often used next to each other to create a wider support zone. The fixed components before being inserted into the tube are seen below:

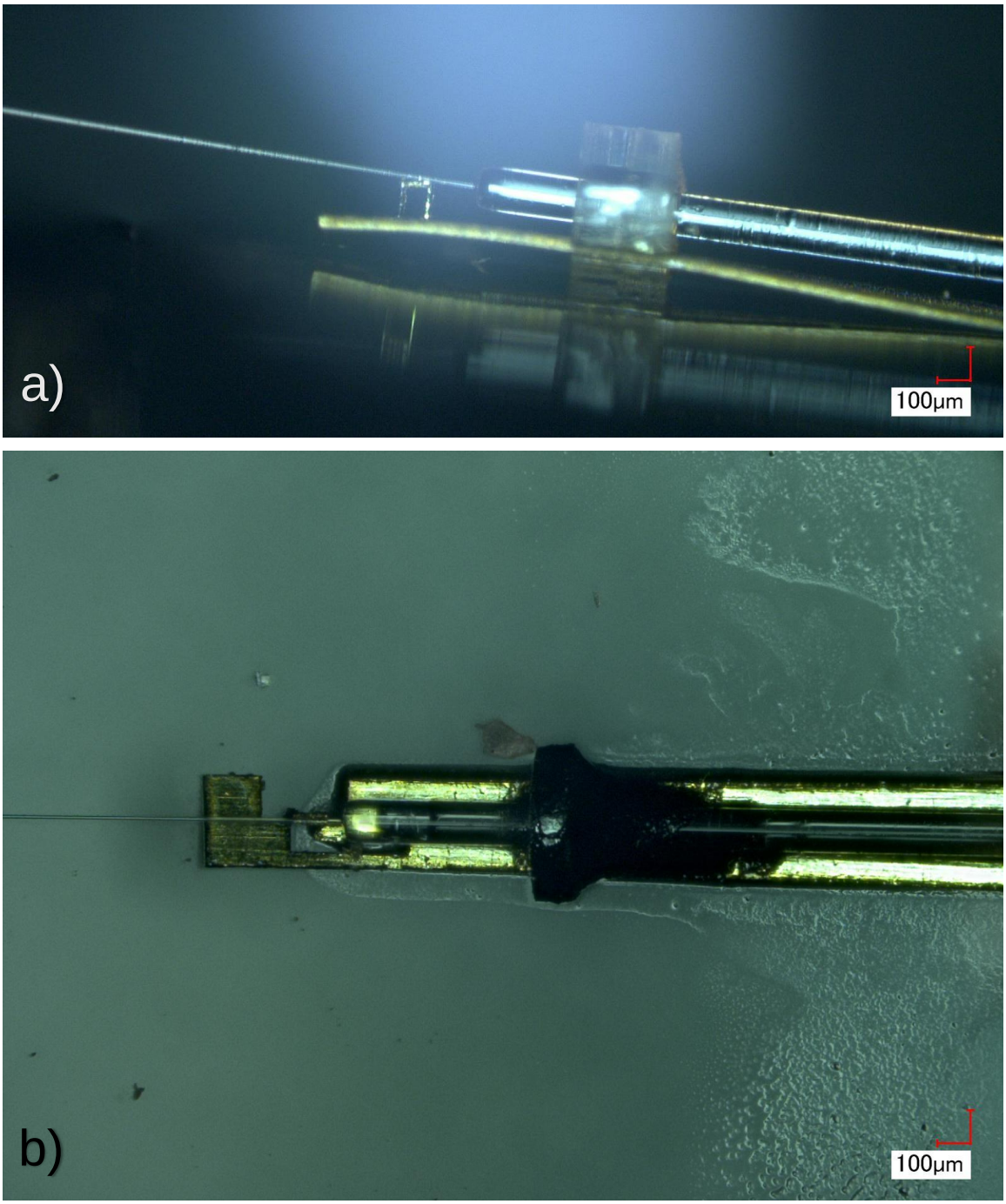

Figure A1. Samples before being inserted into the tube; (a) side view of a brass sample with no EP17 (b) top view of a brass sample after the application and curing of EP17

Just the collar itself inside of the tube is shown below:

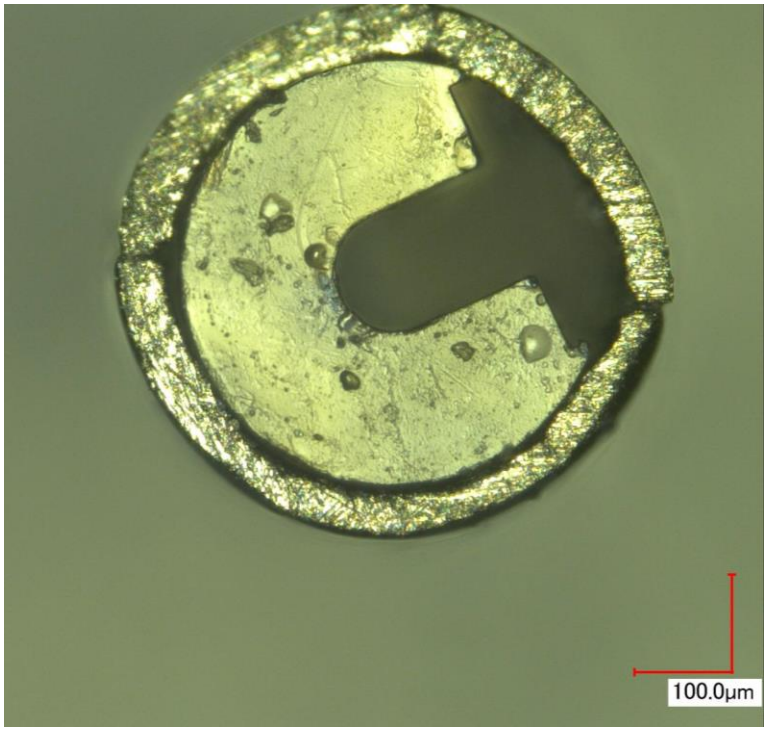

Figure A2. The PMMA collar inside of a 500-micron diameter tube

Similarly, the figure below showcases the bottom semi-circle piece with no collar on top or EP17 applied to the inside of the tube:

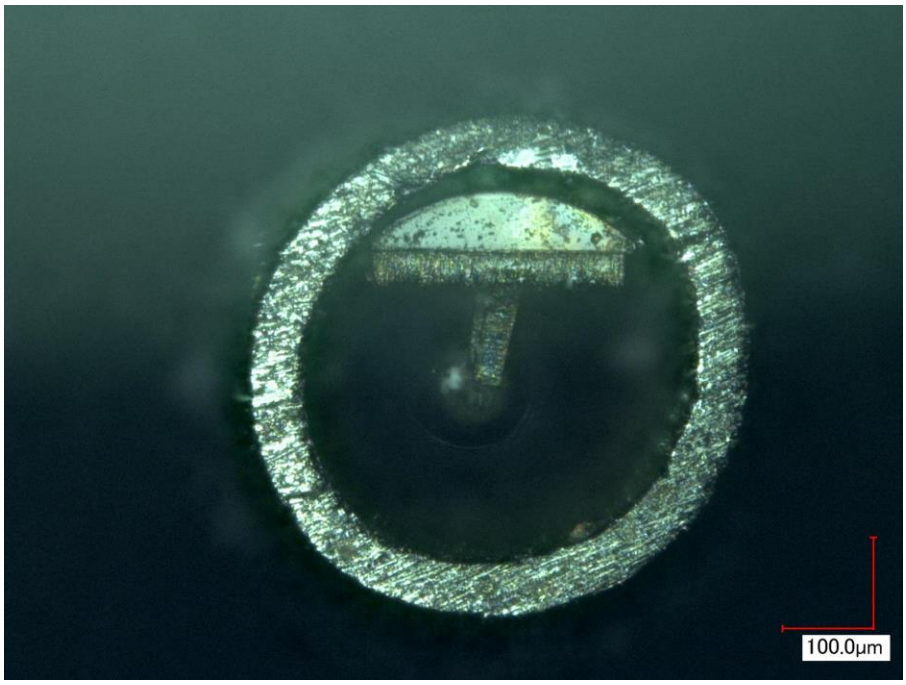

Figure A3. The platform created by the semi-circle bottom piece

By combining all of the aforementioned steps together, the assembly process is completed:

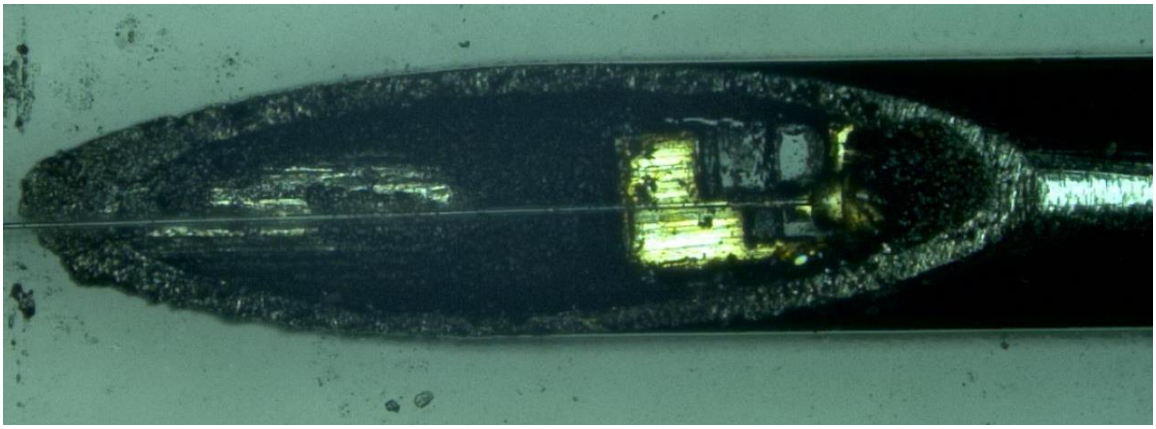

Figure A4. Top view of a completed brass sample assembly

The tube is cut at an angle to make it possible to observe and monitor the device. Similarly, the front and side views of a complete assembly are shown below:

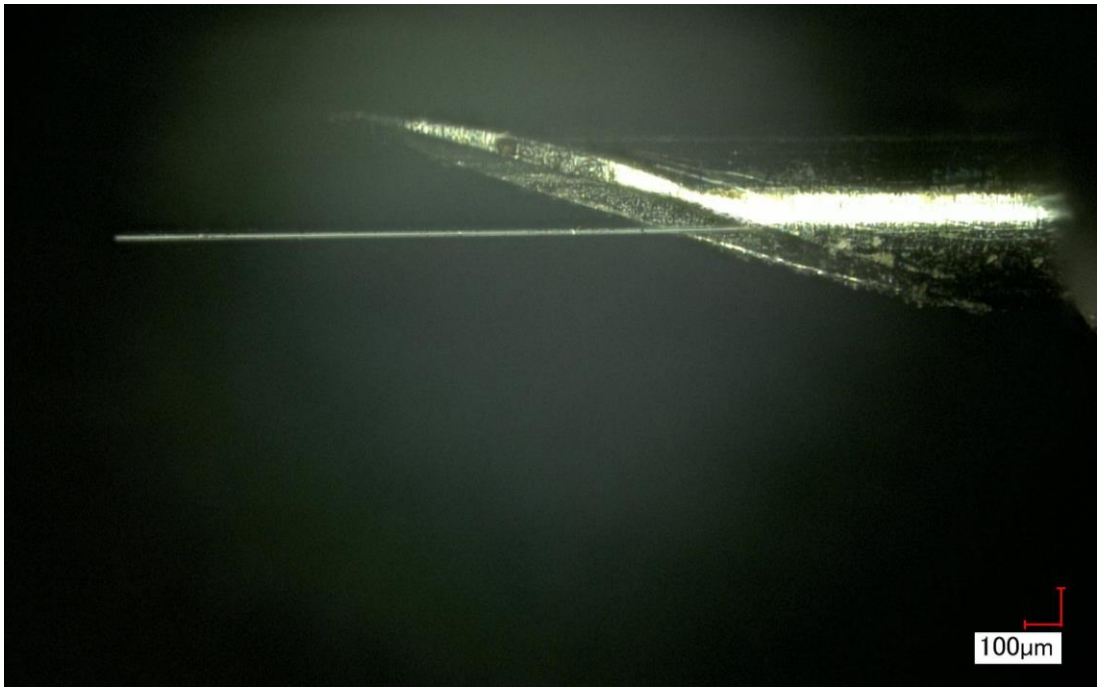

Figure A5. Side view of a completed assembly

Figure A6. **Front view of a completed assembly; the collar, collection portion of fiber, the actuator, and platform below can be seen inside of the tube**